



Simulation and Microwave Measurement of the Conductivity of Carbon Nanotubes

By Daniel Ifesinachi Odili

A thesis submitted to the University of Birmingham for the degree of
DOCTOR OF PHILOSOPHY

The University of Birmingham

School of Electronic, Electrical and Computer Engineering

College of Engineering and Physical Sciences

December 2010

UNIVERSITY OF
BIRMINGHAM

University of Birmingham Research Archive

e-theses repository

This unpublished thesis/dissertation is copyright of the author and/or third parties. The intellectual property rights of the author or third parties in respect of this work are as defined by The Copyright Designs and Patents Act 1988 or as modified by any successor legislation.

Any use made of information contained in this thesis/dissertation must be in accordance with that legislation and must be properly acknowledged. Further distribution or reproduction in any format is prohibited without the permission of the copyright holder.

BIOGRAPHICAL SKETCH

Daniel Odili attended Irwin College in Leicester, United Kingdom, graduating in 2003. He completed his Bachelors of Science with Honours in Electronic and Electrical Engineering at the University of Birmingham, United Kingdom, in July 2006. His undergraduate project was on emerging devices simulation under the supervision of Dr Tony Childs. In this project, he modelled electron transport in carbon nanotubes. Daniel continued his graduate programme at the University of Birmingham in October, 2006. He stayed within the emerging device technology group in the department of Electrical, Electronic and Computer Engineering. His doctorate programme on simulation and microwave measurement of the conductivity of carbon nanotubes was supervised by Dr Tony Childs. Daniel collaborated with the microwave group at Cardiff University to undertake the microwave studies of carbon nanotubes.

ABSTRACT

Recently, excellent properties have been realised from structures formed by carbon nanotubes. This propelled their use as nanoscale electronic devices in the information technology industry. The discovery of carbon nanotubes has stimulated interest in carbon-based electronics. Metal-Oxide-Semiconductor systems (MOS) are used to model charge transport within these carbon structures. Schrodinger's equation is solved self-consistently with Poisson's equation. The Poisson equation, which defines the potential distribution on the surface of the nanotube, is computed using a two-dimensional finite difference algorithm exploiting the azimuthal symmetry. A solution to the Schrodinger's equation is required to obtain the wavefunctions within the nanotube model. This is implemented with the scattering matrix method. The resulting wavefunctions defined on the nanotube surface are normalised to the flux computed by the Landauer equation. A novel implementation of the Schrodinger-Poisson solver for providing a solution to a three dimensional nanoscale system is described. To avoid convergence problems, an adaptive Simpson's method is employed in the model devices. Another main contribution to this field is the highlighting of the differences in the output characteristics of carbon nanotube- and graphene-based devices. In addition, the source and drain contacts that give an optimum device performance are identified. The limitation of this model is that quantised conductance appears on making contact to the nanotube ends. Electron transport in carbon nanotubes can be studied using non-contacting means. A new approach is to induce current in the nanotubes using microwave energy. A resonator-based measurement method is used to examine the electrical properties of the nanotubes. Remarkably, the nanotubes appear to have the smallest sheet resistance of any non-superconducting material. The possibility of a ferromagnetic carbon nanotube is investigated due to the remarkable screening properties observed. Measurements of the magnetisation as a function of the applied magnetic field are conducted using a vector vibrating sample magnetometer. The morphology and microstructure of the nanotubes are observed using scanning electron microscopy (SEM) and transmission electron microscopy (TEM), respectively. Carbon nanotubes can be contaminated with metal particulates during growth. These impurities can modify charge transport in these carbon structures.

ACKNOWLEDGMENT

Firstly, I would like to thank God for giving me knowledge and wisdom. I would like to appreciate my family for praying for me continually and supporting my education financially.

I would like to appreciate the efforts of Dr Tony Childs to see that I complete my PhD. He was my personal tutor for my undergraduate programme and now my project supervisor for my doctorate programme.

I would like to extend my appreciation to Professor Adrian Porch at Cardiff University for his contribution to this project. I would like to acknowledge the contributions of my research colleagues to this work, mostly Yudong Wu and Aslam Sulaimalebbe. I would like to extend my appreciations to Dr P. Weston, one of my advisors throughout my stay in this department.

Finally, I would like to thank the department of electrical, electronic and computer engineering for accommodating me for both my undergraduate and postgraduate programmes.

Table of Contents

Biographical Sketch

Abstract

Acknowledgement

List of Figures

List of Tables

List of Symbols

Chapter 1.....1

Introduction..... 1

1.1 Carbon Structures 1

1.2 Carbon Electronics 3

1.3 Thesis Outline 7

1.4 References 10

Chapter 2.....14

**Modelling Charge Transport in Carbon Nanotubes using a Coupled
Schrodinger-Poisson Solver 14**

2.1 Introduction 14

2.1.1 Graphene..... 15

2.1.2 Carbon Nanotubes 20

2.2 Modelling Techniques..... 27

2.2.1 Finite Difference Method	27
2.2.2 Scattering Matrix Method.....	32
2.3 A Two-Dimensional Simulation of Carbon Nanotube Field-Effect Transistors.....	35
2.4 Simulation Results.....	42
2.4 Role of the Metal-Carbon Nanotube Contact in Computing Electron Transport in Carbon Nanotubes	47
2.5 Conclusions	53
2.6 References	54
Chapter 3.....	57
Comparison of the Current-Voltage Characteristics of MOS Devices Based on Carbon Nanotubes and Graphene	57
3.1 Introduction	57
3.2 Model - Graphene Nanostrip Field Effect Transistors (GFETs).....	58
3.3 Device Simulation	60
3.4 Simulation Results.....	63
3.5 Conclusions	69
3.6 References	70
Chapter 4.....	72
Experiment – Contactless Measurements of Electron Transport in Carbon Nanotubes	72
4.1 Introduction - Metallic Contact Limitations	72
4.2 Experimental Techniques	74
4.2.1 Scanning Electron Microscopy/Transmission Electron Microscopy [5].....	74
4.2.2 Energy Dispersive X-ray Spectroscopy [7]	75

4.3 Microstructure and Morphology of the CNTs.....	76
4.4. Copper Hairpin Resonator.....	80
4.5 Experimental Analysis using Cavity Perturbation Technique	83
4.6 Experimental Results.....	89
4.7 Conclusions	95
4.8 References	96
Chapter 5.....	98
3D Electromagnetic Simulation of Hairpin Resonator for the Microwave Characterisation of Carbon Nanotubes Sample	98
5.1 Introduction	98
5.2 Background	99
5.2.1 Theory of COMSOL Multiphysics [4]	100
5.2.2 Skin Depth	104
5.2.3 Calculation of the Charge Density in a Carbon Nanotube	105
5.3 Modelling of Hairpin Resonator	109
5.3.1 Introduction	109
5.3.2 Hairpin Resonator Model	112
5.3.3 Simulation Results.....	114
5.4 Discussion	119
5.5 Conclusions	122
5.6 References	123
Chapter 6.....	125
Conclusions and Future Work	125
6.1 General Observation.....	125

6.2 Future Outlook	127
6.3 References	129
Appendix 1	130
Appendix 2	134
Appendix 3	137
Appendix 4	139
Appendix 5	144
Appendix 6	147
Appendix 7	148
Appendix 8	151
Appendix 9	162
Appendix 10	163

List of Appendices

A1. Detailed Procedure for Implementing a Finite Difference Algorithm	130
A2. Explanation of the Scattering Matrix Method by Analysing a Single Symmetric Planar Barrier of Defined Width and Height	134
A3. Derivation of the Laplace equation as a Function of Polar and Cylindrical Coordinates	137
A4. A Detailed Procedure for Computing the Electrostatic Potential within the CNFET Structure	139
A5. A Detailed Description of the Grid Implementation for the CNFET Device	144
A6. Debye Length Theory	147
A7. The Images Obtained from the Morphology and Microstructural Studies Conducted on the Nanotube Sample	148

A8. 3D Electromagnetic Simulation of Sapphire Dielectric Resonator for the Microwave Characterisation of Carbon Nanotubes Sample	151
A9. Publication - Modelling Charge Transport in Graphene Nanoribbons and Carbon Nanotubes using a Schrodinger–Poisson Solver.....	162
A10. Publication - Microwave Characterisation of Carbon Nanotube Powders	163

List of Figures

Figure 1.1: Some allotropes of carbon [2].	2
Figure 2.1: Graphene Lattice. The carbon atoms are illustrated using the shaded nodes and the chemical bonds represented by the lines are derived from the sp^2 -orbitals. The primitive lattice vectors are $a_{1,2}$ and the unit-cell is the shaded region. There are two carbon atoms per unit-cell, represented by 1 and 2.....	16
Figure 2.2: The dispersion relation of graphene. The conduction and valence states meet at K-points.....	20
Figure 2.3: (a) Hexagonal lattice structure of a graphene sheet, (b) carbon nanotube formed by rolling up a graphene sheet [6][7].....	21
Figure 2.4: A zig-zag carbon nanotube, where T represents the length of the unit cell.	23
Figure 2.5: Brillouin zone for a zig-zag ($n = 16$) nanotube super-imposed on graphene k -space. The wave vectors along the nanotube axis and perpendicular direction are represented by k_z and k_θ , respectively. The dash lines at the ends are for zone boundaries and they count as a single slice.....	24
Figure 2.6: (a), (b) - Typical nodes in cylindrical coordinates and (c) Finite difference grid for an axisymmetric system.	28
Figure 2.7: Interface between two different media.	30
Figure 2.8: Flux of carriers injected from each contact into the device (a). A fraction of the flux from both sides transmits across the device (b) Equilibrium and (c) Under bias.....	32

Figure 2.9: Fluxes of charge carriers incident upon and reflected from a slab of finite thickness.....	33
Figure 2.10: Two scattering matrices cascaded to produce a single, composite scattering matrix.	34
Figure 2.11: The Coaxial Carbon Nanotube FET Geometry.....	35
Figure 2.12: Cylindrical Coordinates.....	36
Figure 2.13: Iterative procedure for computing electrostatics and charge transport self-consistently.	42
Figure 2.14: Simulation of the potential energy seen by the electrons at different gate bias for the equilibrium condition ($V_{ds} = 0V$). Conduction band edge along the length of the device for $V_{gs} = 0.1V$, $V_{gs} = 0.3V$ and $V_{gs} = 0.5V$	43
Figure 2.15: Conduction band edge along the device length for $V_{gs} = 0.5V$, $V_{ds} = 0V$ and $V_{ds} = 0.4V$. The energies are with respect to the source Fermi level.	44
Figure 2.16: Simulation of the carrier density as a function of position and varying V_{ds} when $V_{gs} = 0.5V$	44
Figure 2.17: Transmission probabilities for electrons (a), and the corresponding conduction band edge (b) at $V_{gs} = 0.5V$ and $V_{ds} = 0.4V$	45
Figure 2.18: The I-V characteristics of the zig-zag nanotube for different gate bias.	46
Figure 2.19: Drain current characteristics for the nanotube based on the FETtoy model [15]	46
Figure 2.20: (a) A carbon nanotube ‘end bonded’ to the metal, (b) a carbon nanotube forming ‘side contacts’ on gold electrodes	48
Figure 2.21: The band bending for the metal/nanotube junction at $V_{gs} = 1V$, $V_{ds} = 0V$, $V_{ds} = 0.4V$ and the transmission probability for electrons at $V_{ds} = 0.4V$, $V_{gs} = 1V$. [Ag with $\phi = 4.5eV$ - (a), (b)], [Fe with $\phi = 4.8eV$ - (c), (d)] and [Au with $\phi = 5.1eV$ - (e), (f)]. The band bending occurs over a length scale Ld	50
Figure 2.22: Plot of CNFETs I-V characteristics as a function of metal contacts at $V_{gs} = 1V$	51
Figure 2.23: The ideal output characteristics of the device without contact effects [15].	52
Figure 3.1: Cubical geometry of Graphene FET.	59
Figure 3.2: Normalised potential updates after each iteration.	63
Figure 3.3: Simulation of the potential energy seen by the electrons at $V_{gs} = 0.5V$ (a) 3D view of the conduction band edge at $V_{ds} = 0.0V$ (b) 3D view of the conduction band edge at	

$V_{ds} = 0.4V$ (c) Conduction band edge along the length of the device for different V_{ds} at the edge of the graphene sheet (d) Conduction band edge along the length of the device for different V_{ds} at the centre of the graphene sheet.	64
Figure 3.4: Simulation of the carrier density at $V_{gs} = 0.5V$. (a) 3D view of the net carrier density as a function of position at $V_{ds} = 0.0V$. (b) 3D view of the net carrier density as a function of position at $V_{ds} = 0.4V$. (c) Cross-section of carrier density for different V_{ds} at the centre of graphene sheet (d) Cross-section of carrier density for different V_{ds} at the edge of the graphene sheet.	65
Figure 3.5: I-V characteristics of Graphene (a) and CNT (b).....	66
Figure 3.6: Transmission Probability and Fermi Dirac Distribution for different V_{ds} . Carbon nanotubes – (a), (c), (e) and graphene – (b), (d), (f)	68
Figure 4.1: (a) A small drain bias applied across the channel causing a splitting of the electrochemical potentials. (b) Energy level broadening due to the process of coupling to the channel.	73
Figure 4.2: SEM image of the CNTs used for this experiment (a) before and (b,c) after manual grinding.	77
Figure 4.3: (a) The TEM image of the nanotube sample, the dark spots representing the impurities and (b) an evidence of the Fe content (inset) in the STEM image of the sample...	78
Figure 4.4: EDX result showing the composition of the CNTs.....	79
Figure 4.5: A schematic of the hairpin resonator used for the microwave measurements [9]. (a) Side view (b) Top view and (c) Inner structure.....	81
Figure 4.6: The spectral response of a resonator in transmission mode observed using the Agilent E5071B Network Analyser.	82
Figure 4.7: (a) 3GHz copper hairpin resonator & (b) Inner structure of the resonator.....	83
Figure 4.8: Screening current in the CNTs sample due to applied magnetic field.	84
Figure 4.9: Possible screening current patterns for various orientations of the CNTs in the bulk sample.	85
Figure 4.10: One of the possible geometries of the nanotubes in the bulk sample.....	86
Figure 4.11: Spectral response of the empty hairpin resonator.	90
Figure 4.12: Calibration experiment: (a) Quartz tube loaded with copper spheres. (b) Spectral response of the hairpin resonator when loaded with small copper spheres.	91

Figure 4.13: (a) Spectral response of the hairpin resonator when loaded with nanotubes sample, (b) Scaled plot of the spectral response shown in (a).	92
Figure 4.14: Resonant traces for graphite powder.	93
Figure 4.15: Magnetisation versus applied magnetic field curve for the sample with a mass of 7mg.	94
Figure 5.1: Cylindrical geometry of (a) carbon nanotube, and (b) copper wire.	105
Figure 5.2: The representation of the Fermi surface in momentum space [7].	106
Figure 5.3: Density of states $D(E)$ for a carbon nanotube calculated using Eq. 5.33.	108
Figure 5.4: Schematics of the hairpin resonator, where l is the plate length, W is the plate width, d is the separation between the plates and t is the plate thickness [9][11].	109
Figure 5.5: 3D geometry of the hairpin resonator modelled using COMSOL Multiphysics.	112
Figure 5.6: 3D geometry of the hairpin resonator cut in half to reduce the size of the RF cavity problem.	113
Figure 5.7: Field concentration and distribution within the hairpin. (a) High magnetic field concentration observed at the short-circuited end of the hairpin. (b) Electric field is maximum at the open end of the hairpin.	115
Figure 5.8: Top view of the magnetic field pattern within the radiation shield of the hairpin resonator.	115
Figure 5.9: The hairpin resonator is loaded with tightly packed nanotubes sample (0.4mm ³ in volume corresponding to a sample mass of 1.3mg).	116
Figure 5.10: Quantization of electronic wave states around a carbon nanotube. (a) The parallel and perpendicular axes of a CNT. (b) The contour plot of graphene valence states for a CNT [13].	120
Figure 5.11: Screening currents for the microwave magnetic field applied parallel to the nanotube axis.	120
Figure A1.1: Common grid patterns: (a) rectangular grid, (b) skew grid, (c) triangular grid, (d) circular grid.	130
Figure A1.2: Estimates for the derivative of $f(x)$ at P using forward, backward, and central differences.	131
Figure A1.3: Finite difference mesh for two independent variables x and t	132

Figure A2.1: A simple rectangular tunnelling barrier.....	134
Figure A3.1: Cylindrical Coordinates.....	137
Figure A5.1: Grid implementation of the azimuthal symmetry in the coaxial CNFET.	144
Figure A7.1: (a), (b) - Series of TEM micrographs showing the microstructure of the CNTs. (c), (d) - Images (a) and (b) are magnified, black spots showing impurities.	148
Figure A7.2: (a), (b) – Series of STEM photographs showing the bulk nanotube sample....	149
Figure A7.3: EDX analysis is performed on the inset shown in (a). (b) – Carbon, (c) – Silicon, and (d) – Iron	150
Figure A8.1: Field configuration for a TE011 resonant mode [3].	152
Figure A8.2: A schematic of the cylindrical sapphire resonator. (a) Resonator with the field lines, dotted lines represent magnetic field patterns while the solid lines represent the electric field patterns (b) Top view of the structure.	153
Figure A8.3: 2D & 3D geometries of the sapphire resonator modelled using COMSOL.....	156
Figure A8.4: The TE011 magnetic field pattern in the sapphire resonator simulated using COMSOL (a) before inserting the conducting sample, (b) after inserting the sample.....	157
Figure A8.5: Field screening observed when the conducting sample is placed in the region of high magnetic field. (a) Assumed conductivity of 104 S/m, and (b) conductivity of 107 S/m.	159
Figure A8.6: The plot of the magnetic field strength against position (z [m]) along the surface of the conducting sample with varying conductivity.	160

List of Tables

Table 2.1: The bandstructure properties of the first three subbands, where $\text{gcd}(i, j)$ is the greatest common divisor of i and j [8].	26
Table 4.1: Elemental analysis of the nanotubes sample using EDX.....	79
Table 5.1: Recorded increase in the resonant frequency as the conductivity of the nanotubes sample increases.....	117
Table A8.1: The skin depth computed from our simulation model is compared to that of the surface resistivity model.	158

List of Symbols

$\phi(\vec{x})$ - Atomic wavefunctions

\hat{H} - Hamiltonian operator

$E(\vec{k})$ - Dispersion relation

C_h - Chiral (wrapping) vector

R_t - Nanotube radius

L_t - Length of nanotube

T - Transmission coefficients

k - Wavevector

V - Electric potential

Q - Charge density

ε - Relative permittivity

R_g - Gate radius

t_{ins} - Insulator thickness

V_{cnt} - Nanotube surface potential

$\Psi(E)$ - Wavefunction of carriers

E - Energy

E_{gap} - Bandgap

m^* - Effective mass

U - Local effective potential

χ_{cnt} - Electron affinity of carbon nanotube

V_s - Source voltage

V_d - Drain voltage

V_g - Gate voltage

φ - Work function

I_p - Probability current

I_L - Landauer current

f - Fermi-Dirac carrier distribution

q - Electron charge

m_0 - Free electron mass

I_D - Drain current

L_d - Debye length

μ_r - Relative permeability

c - Speed of light

f_0 - Resonant frequency

Q_L - Load impedance

f_B - Bandwidth at half-maximum power

H_0 - Applied magnetic field

J - Current density

σ - Electrical conductivity

R_{sq} - Sheet resistance

δ - Skin depth

μ_0 - Permeability of free space

ϵ_0 - Permittivity of free space

$Q_{c,d}$ - Quality factor

$\tan\delta$ - Loss tangent

v - Velocity

D - Electric flux density

M - Magnetisation

P - Polarisation density

V_{loop} - Loop potential

ω - Angular frequency

$\langle P_{cnt} \rangle$ - Power loss in the sample

$\langle P_D \rangle$ - Dielectric power loss

$\langle P_R \rangle$ - Power loss due to fields radiation.

$\vec{\mu}$ - Electron orbital magnetic moment

I - Current

μ_B - Bohr magneton

h - Planck's constant

k_B - Boltzmann's constant

Chapter 1

Introduction

1.1 Carbon Structures

Over the past several decades, the density of devices on a microprocessor has been doubling every three years. Metal-oxide-semiconductor field-effect transistors (MOSFETs) are now approaching their scaling limit. To avoid scaling issues the channel of a MOS device could be replaced with a nanoscale structure. A carbon nanotube (CNT) can serve as the channel of a MOS device because it is a nanoscale structure with excellent electronic properties.

In the early nineties, Sumio Iijima brought CNTs into the awareness of the scientific community [1]. Since then, there has been rapid progress in understanding their electronic properties. CNTs are cylindrical structures of nanometric size, based on a hexagonal lattice of carbon atoms. Before the electronic properties of CNTs can be understood, the properties of the carbon atom must first be studied.

There are six electrons inside a carbon atom, which orbit the nucleus in shells. Two electrons are in the inner shell while the other four are in the outer shell. The state of these outer electron shells determines the stability of the carbon atoms. A stable arrangement is achieved when the outer electron shell is full. Atoms gain, lose, or share electrons with neighbouring atoms so that all the atoms involved end up with complete outer shells. As they share electrons in a reaction, they form bonds between each other, leading to molecules and compounds formation.

Fig. 1.1 shows different crystalline forms of carbon. These crystalline forms of carbon are called allotropes, which include diamond, graphite, buckyball, graphene and carbon nanotube [2].

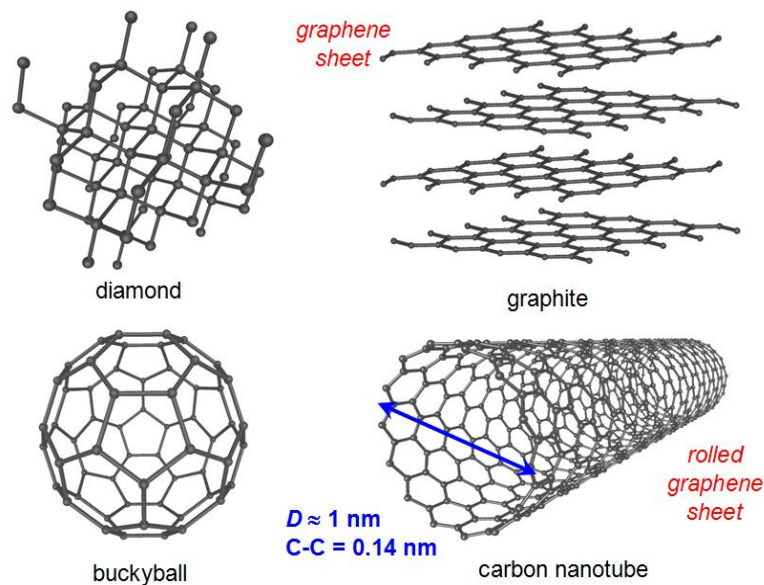


Figure 1.1: Some allotropes of carbon [2].

Diamond is the hardest natural substance on earth due to the strong bonding between the carbon atoms. Each carbon atom in a diamond molecule is joined to four others in a tetrahedron structure. The bonds have similar strength and a regular pattern through the molecule.

Graphite is a layered compound, the carbon atoms on each layer are arranged in a hexagonal lattice with separation of 0.142 nm and the distance between the planes is 0.335 nm .

Fullerene is an allotrope of carbon with a structure similar to that of graphite but the carbon atoms are linked in hexagonal and pentagonal patterns. The surface of a fullerene molecule looks like a soccer ball, which gave it the name buckyball.

Graphene is a flat monolayer of carbon atoms, tightly packed into a two-dimensional honeycomb lattice [3]. It is the basic building block for graphitic materials of all other dimensionalities. Initially, graphene was presumed not to exist in free state but Novoselov et.al [3] managed to extract graphene from bulk graphite in 2004. Graphene has the potential to be the building block for next generation nanoelectronics because of its unique electronic properties.

CNT is the main allotrope of carbon studied in this work. CNTs are categorized as single-walled nanotubes (SWNTs) and multi-walled nanotubes (MWNTs). A SWNT consists of a single graphene sheet rolled up to form a tube while a MWNT consists of multiple graphene sheets.

In the next section, the properties of carbon that make them useful in electronics application are discussed.

1.2 Carbon Electronics

The enormous growth in the information technology industry has been based on developments in charge transport of semiconductor devices. The most important device is the MOSFET and its development has been based on planar technology and the oxidation of silicon. The mobility of the charge carriers in the channel region is one of the most important parameters that determine the performance of a MOSFET. High mobilities are obtained when the effective mass of the charge carriers is small and the mean time between their collisions is long.

Recently, devices based on carbon have attracted considerable interest due to the remarkable properties of structures formed from carbon nanotubes [4][5][6]. Initially, CNTs were extensively studied as they could be either metallic or semiconducting. Experimentally,

electrons were found to travel along the CNTs ballistically [7]. In metallic CNTs, the energy bandgap is zero and electrons travel at the Fermi velocity $v_F = 8 \times 10^5 m/s$ [8].

Stanford University developed a compact model that can be used to investigate the performance of carbon nanotube field-effect transistors (CNFETs) [9][10][11]. This model accounts for practical issues such as scattering in the channel, electron-electron interactions, effects of source/drain extension region, and charge screening. In addition, the model can be used to examine the frequency response and the circuit compatibility of interconnected CNFETs [12][13][14][15].

There is a great interest in CNTs because the prototype structures of carbon nanotube field-effect transistors displayed excellent performance. Although, the performance of CNFETs is comparable to that of silicon-based MOS transistors, it is still difficult to control the energy bandgap of the nanotubes. The bandgap of a CNT is dependent on its diameter and chirality, which is uncontrollable during growth. This limits the use of CNFETs in integrated circuit (IC) applications.

Alternatively, a semiconducting graphene structure such as a graphene nanoribbon can replace the CNT structure in the MOS device. The electron mobility μ for graphene can exceed $15,000 cm^2/Vs$. Graphene has an advantage over CNT because it can be patterned using standard nanoelectronics lithography. It has been reported that graphene could be easily produced using sticky tape [16]. When tailored to less than $100nm$ wide, graphene nanoribbons open a bandgap. This bandgap is due to electron confinement. The bandgap can be varied by simply changing the edge types or width of the nanoribbon, which makes it possible to use graphene as the channel of MOSFETs.

Various techniques have been employed to model charge transport within CNTs and graphene-based devices. These techniques include non-equilibrium green function (NEGF), atomistic NEGF, and Schrodinger-Poisson solver. These techniques are based on the self-consistent simulation scheme, and they adequately treat electron transport within the structures when they are coupled to end contacts. These modelling techniques are now reviewed.

In the NEGF approach [17][18][19], the model device is described by a Hamiltonian matrix (H). The self-consistent potential is incorporated into this Hamiltonian matrix, which is coupled to the end contacts (Source/Drain contacts). The self-energy matrices, Σ_S and Σ_D are used to describe the coupling between the channel and the end contacts. The contacts are characterised by the left and right Fermi energies ε_{f1} and ε_{f2} , respectively. Incoherent charge transport can be described using the self-energy Σ_{scat} [20]. In nanoscale structures such as CNTs, electrons are assumed to move in the active region coherently and unscattered [21]. They operate in the ballistic transport regime where the scattering length is much greater than the device length. In this case, the self-energy Σ_{scat} can be ignored in the Hamiltonian matrix. Using these parameters ($H, \Sigma_S, \Sigma_D, \varepsilon_{f1}, \varepsilon_{f2}$), the transmission coefficient, the device charge density and the terminal currents are computed by performing numerical integrations over the energy space.

The network for computational nanotechnology at Purdue University developed FETtoy, which is a set of MATLAB scripts used to compute the ballistic output characteristics of CNFETs [22][23][24][25]. FETtoy employs the NEGF approach for quantum transport and it assumes a cylindrical geometry for CNT-based devices [26]. Although, this model considers only the lowest subband, it can be simply modified to include multiple subbands.

The atomistic NEGF [27][28] method can be used to examine the impact of bandstructure effects on carrier transport in nanoscale devices such as CNFETs. The first step is to identify a set of atomistic orbitals that describe the fundamentals for carrier transport. This basis set is then used to derive the Hamiltonian matrix for the isolated channel. The size of the Hamiltonian matrix depends on the number of carbon atoms in the channel. The tight-binding approximation [29] is used to describe the interaction between the carbon atoms, and the nearest-nearest neighbour coupling is included in this approximation. The self-energy matrices for the end contacts are obtained from the channel's Hamiltonian matrix.

The NEGF approach is numerically intensive and it is difficult to develop simple intuitive description of the device physics. Therefore, a simpler modelling technique based on ballistic transport assumption is required. Electron transport through nanoscale devices is more

affected by quantum mechanical phenomena [4][30]. In this work, the Schrodinger-Poisson solver is the technique employed to model charge transport within CNTs and graphene-based devices. This solver is a full quantum mechanical transport model that describes the wave-like behaviour of the electrons in the ballistic transport regime. This modelling technique is based on a self-consistent solution of the Schrodinger and Poisson equations.

The solution to the Poisson's equation is obtained using a two-dimensional finite difference method [31]. The finite difference method is based on approximations that allow the differential equations to be replaced by finite difference equations. These finite difference equations are algebraic in form and they relate the value of the dependent variable at a point in the solution region to some neighbouring point's value. A detailed procedure of the finite difference method is described in Appendix 1.

The solution to the Schrodinger's equation is obtained using the scattering matrix method [32]. In this approach, the device regions are characterised by the transmission and the reflection of incoming waves from both ends of the device. The knowledge of the overall transmission coefficient is then used to compute the charge density in the device. In Appendix 2, the scattering matrix method is described in detail.

Successful device modelling requires various parameters to be determined experimentally. Researchers in this field have employed a range of techniques to determine the transport parameters. Connecting electrodes to the nanotube ends is the most common experimental technique used to detect electric signals through a nanotube. However, difficulties arise due to contact effects in low-dimensional systems. The concepts of bulk device physics do not simply apply to low dimensionality structures, leading to unusual device performance when electrodes are attached. For instance, the contact interface realised in a CNFET device could introduce strain in the CNT used as the channel. This can lead to strain-induced bandgaps, which will influence the electronic properties of the CNT.

In this thesis, a contactless measurement technique is investigated, which involves inducing current in the nanotubes using microwave energy. In the course of these measurements, CNTs were found to show remarkable screening properties. Further experimental work

showed that the CNTs also had magnetic properties as observed by other workers but without satisfactory explanation.

1.3 Thesis Outline

The aim in this thesis is to provide a detailed study of electron transport within CNTs. This thesis builds on previous work that has been carried out on CNTs [4]. At the initial stage of this work, electron transport in a CNT-based MOS transistor using a coupled Schrodinger-Poisson solver is simulated. In this case, metallic contacts are used to terminate the nanotube ends.

Simulation results show that the CNT device performance is influenced by these metallic contacts. Therefore, other ways of examining electron transport in a CNT were investigated. One of the possible ways is to induce current in the CNT using microwaves and then examine the microwave loss.

Due to the screening properties observed in the microwave experiment, the possibility of a ferromagnetic CNT is investigated. The experimental analysis suggests that an additional feature of a CNT is its strong magnetic nature. Based on this suggestion, a CNT could serve as the main building block for future magneto-electronic device. The structure of this thesis is as follows:

- **Modelling Charge Transport in Carbon Nanotubes using a Coupled Schrodinger-Poisson Solver (Chapter 2)**

Chapter 2 of this thesis describes the simulation of electron transport in a semiconducting CNT by solving self-consistently a coupled Poisson and Schrodinger equations using a finite difference technique and a scattering matrix method, respectively. The performance of the CNT-based device is analysed from the conduction band profile, the carrier concentration

along the nanotube length, the transmission probabilities for electrons and the current-voltage characteristics of the device.

Since the CNT ends are terminated with metallic contacts, there is a Schottky barrier at the CNT/contact interface, and the on-current of the device depends on the barrier height. Therefore, the role of the CNT/metal interface in the performance of a CNFET device is examined. Finally, the type of metal contact that gives the optimum CNFET performance is identified.

- **Comparison of the Current-Voltage Characteristics of MOS Devices Based on Carbon Nanotubes and Graphene (Chapter 3)**

In Chapter 3, a MOS structure based on a graphene nanostrip is modelled and its performance is compared to that of a CNFET device. The Schrödinger-Poisson solver is employed to examine the electronic properties of a semiconducting graphene nanostrip.

A tight-binding method is used to obtain the energy bandstructure in graphene. A three-dimensional (3D) simulation of the graphene nanostrip field-effect transistor (GFET) is performed using a self-consistent solution of Schrödinger and Poisson equations. Also, the on-state of a GFET is compared to that of a CNFET, and the differences in their output characteristics highlighted.

- **Experiment – Contactless Measurements of Electron Transport in Carbon Nanotubes (Chapter 4)**

In Chapter 4, a non-contact experiment to study electron transport within CNTs is performed. In this experiment, current is induced in the CNTs using microwave energy. A sample of CNTs is inserted into the cavity of a hairpin resonator, and the change in the internal properties of the resonator is analysed.

Ferromagnetism in CNTs is investigated because the CNTs sample screens the applied magnetic field. The ferromagnetic properties of the CNTs are examined using vibrating sample magnetometer. Morphology and microstructural studies are conducted on the CNTs sample to confirm its composition.

- **3D Electromagnetic Simulation of Hairpin Resonator for the Microwave Characterisation of Carbon Nanotubes Sample (Chapter 5)**

In Chapter 5, the experiment described in Chapter 4 is simulated using COMSOL multiphysics. A 3D modelling of tightly packed carbon nanotubes in a hairpin resonator is described. Conductivity of the sample is an input parameter in this simulation. The average conductivity of a CNT is derived starting from the density of states calculation.

The magnitude of field screening is examined from the shift in the resonant frequency of the hairpin resonator by introducing different conductivities. Simulation results show that the sample only screens when its conductivity is very high ($> 10^7 \text{S/m}$). Finally, the broadening of the spectral response bandwidth of the hairpin resonator when the sample is introduced into its cavity is examined.

- **Conclusions and Future Work (Chapter 6)**

This chapter is used to summarise the work carried out in this project. The observations made from the AC and DC studies conducted on CNTs are discussed. The simulation and experimental results are compared to other work that has been done in this field. In the work, it was observed that CNTs have intriguing electronic and magnetic properties. One of the suggestions for future work is to use a CNT as the building block of a magneto-electronic device.

1.4 References

- [1] R. Saito, T. Takeya, T. Kimura, G. Dresselhaus, and M. S. Dresselhaus, Raman intensity of single-wall carbon nanotubes, *Physical Review B*, vol. 57, 1998.
- [2] M. S. Dresselhaus, G. Dresselhaus, Ph Avouris, ed(2001). Carbon nanotubes: synthesis, structures, properties and applications, *Topics in Applied Physics* (Berlin: Springer) 80 ISBN 3540410864.
- [3] K. S. Novoselov, A. K. Geim, S. V. Morozov, D. Jiang, Y. Zhang, S. V. Dubonos, I. V. Grigorieva, and A. A. Firsov, Electric Field Effect in Atomically Thin Carbon Films. *Science*, vol. 306, pp. 666-669, 2004.
- [4] D. L. John, L. C. Castro, P. J. S. Pereira, and D. L. Pulfrey, A Schrodinger-Poisson Solver for Modeling Carbon Nanotube FETs, *Proc. NSTI Nanotech*, vol. 3, pp. 65-68, 2004.
- [5] F. Leonard, *The Physics of Carbon Nanotube Devices*, William Andrew Inc., 2009, ISBN 9780815515739.
- [6] A. Loiseau, *Understanding Carbon Nanotubes: from basics to applications*, Berlin-Springer, 2006, ISBN 9783540269229.
- [7] C. T. White, T. N. Todorov, Carbon nanotubes as long ballistic conductors (*Letters to Nature*, 1998), Department of Materials, University of Oxford, Parks Road, Oxford OX1 3PH, UK.
- [8] M. P. Anantram and F. Leonard, *Physics of Carbon Nanotube Electronic Devices*, Institute of Physics Publishing, *Rep. Prog. Phys.* 69 (2006) 507-561.
- [9] H. S. Philip Wong, J. Deng, A. Hazeghi, T. Krishnamohan, G. C. Wan, *Carbon Nanotube Transistor Circuits – Models and Tools for Design and Performance Optimization*, ICCAD'06, November 5-9, 2006, San Jose, CA 94305.

- [10] T. J. Kazmierski, D. Zhou and B. M. Al-Hashimi, HSPICE implementation of a numerically efficient model of CNT transistor, Forum on Specification and Design Languages (FDL 2009), September 22-24, 2009, Germany.
- [11] N. Patil, J. Deng, S. Mitra, and H. S. Philip Wong, Circuit-Level Performance Benchmarking and Scalability Analysis of Carbon Nanotube Transistor Circuits, IEEE Transactions on Nanotechnology, Vol. 8, No. 1, January 2009.
- [12] D. Akinwande, G. F. Close, and H. S. Philip Wong, Analysis of the Frequency Response of Carbon Nanotube Transistors, IEEE Transactions on Nanotechnology, Vol. 5, No. 5, September 2006.
- [13] A. Lin, N. Patil, K. Ryu, A. Badmaev, L. G. De Arco, C. Zhou, S. Mitra, and H. S. Philip Wong, Threshold Voltage and On–Off Ratio Tuning for Multiple-Tube Carbon Nanotube FETs, IEEE Transactions on Nanotechnology, Vol. 8, No. 1, January 2009.
- [14] N. Patil, J. Deng, A. Lin, H. S. Philip Wong, and S. Mitra, Design Methods for Misaligned and Mispositioned Carbon-Nanotube Immune Circuits, IEEE Transactions on Computer-Aided Design of Integrated Circuits and Systems, Vol. 27, No. 10, October 2008.
- [15] L. Wei, D. J. Frank, L. Chang, H. S. Philip Wong, An Analytical Model for Intrinsic Carbon Nanotube FETs, Solid-State Device Research Conference, ESSDERC 2008, 38th European, 15-19 September 2008.
- [16] A. K. Geim and P. Kim, Carbon Wonderland, Scientific American 298 (4), 68-75 (2008).
- [17] J. Guo, S. Datta, M. Lundstrom, and M. P. Anantram, Toward multi-scale simulations of carbon nanotube transistors, the International Journal on Multiscale Computer Engineering, vol. in press, 2004.
- [18] S. Datta, Nanoscale device modeling: the Green's function method, Superlattices and Microstructures, vol. 28, pp. 253-278, Oct. 2000.
- [19] R. Golizadeh-Mojarad and S. Datta, NEGF-Based Models for Dephasing in Quantum Transport, The Oxford Handbook on Nanoscience and Nanotechnology: Frontiers and Advances, eds. A. V. Narlikar and Y. Y. Fu, vol.1, Oxford University Press (2009)

- [20] R. Venugopal, M. Paulsson, S. Goasguen, S. Datta and M. Lundstrom, A simple quantum mechanical treatment of scattering in nanoscale transistors, *J. Appl. Phys.*, vol. 93, no. 9, pp. 5613-5625, May 2003.
- [21] M. Lundstrom, *Fundamentals of Carrier Transport*, Second Edition, Cambridge University Press, 2000.
- [22] A. Rahman, J. Wang, J. Guo, S. Hasan, Y. Liu, A. Matsudaira, S. S. Ahmed, S. Datta, and M. Lundstrom, *Fettoy 2.0 - on line tool*, 14 February 2006. <https://www.nanohub.org/resources/220/>.
- [23] T. J. Kazmierski, D. Zhou and B. M. Al-Hashimi, A Fast, Numerical Circuit-Level Model of Carbon Nanotube Transistor, *Nanoscale Architectures*, IEEE International Symposium, 2007.
- [24] R. Yousefi, K. Saghafi, Modeling of Ballistic Carbon Nanotube Transistors by Neural Space Mapping, 2008 International Conference on Computer and Electrical Engineering.
- [25] R. Yousefi, K. Saghafi, M. K. Moravvej-Farshi, Neural Network Model for Ballistic Carbon Nanotube Transistors, *Nanoelectronics Conference (INEC)*, 2010 3rd International.
- [26] A. Rahman, J. Guo, S. Datta, and M. Lundstrom, *Theory of Ballistic Nanotransistors*, School of Electrical and Computer Engineering, 1285 EE Building, Purdue University, West Lafayette, IN 47907.
- [27] R. Golizadeh-Mojarad, A.N.M. Zainuddin, G. Klimeck and S. Datta, Atomistic Non-equilibrium Green's Function Simulations of Graphene Nanoribbons in the Quantum Hall Regime, *Journal of Computational Electronics*, 7, 407, 2008
- [28] J. Guo, S. Datta, M. P. Anantram and M. Lundstrom, Atomistic Simulation of Carbon Nanotube Field-Effect Transistors Using Non-Equilibrium Green's Function Formalism, *Journal of Computational Electronics*, Volume 3, Numbers 3-4, 373-377, 2005
- [29] J. Fernandez-Rossier, J. J. Palacios, and L. Brey, Electronic structure of gated graphene and graphene ribbons, *Physical Review B*, vol. 75, p. 205441, 2007.

- [30] M. Pourfath, H. Kosina, and S. Selberherr, A fast and stable Poisson-Schrodinger solver for the analysis of carbon nanotube transistors, *Journal of Computational Electronics*, vol. 5, pp. 155-159, 2006
- [31] M. N.O. Sadiku, *Numerical Techniques in Electromagnetics*, CRC Press, Boca Raton, 1992.
- [32] D. K. Ferry and S. M. Goodnick, *Transport in Nanostructures*, Cambridge University Press, 1997.

Chapter 2

Modelling Charge Transport in Carbon Nanotubes using a Coupled Schrodinger-Poisson Solver

2.1 Introduction

Carbon Nanotubes (CNTs) are one-dimensional nanostructures, which have been extensively explored from technological perspectives. Few semiconductor companies such as IBM, Fujitsu and other research institutes have actually used CNTs to build prototype nanodevices such as carbon nanotube field-effect transistors (CNFETs) [1][2]. They were able to construct CNFET devices and build the logic circuits on a wafer scale [3][4]. Numerical simulations are used to explain the engineering issues of the prototype CNFETs, to understand their operation, explore what controls their performance, and explore ways to improve the transistors' performance.

In this chapter, the electronic properties of a CNFET are investigated. The simulation technique employed is based on a numerical algorithm employed by John *et. al* [5]. It relies on a self-consistent solution of the Schrodinger and Poisson equations to compute the conduction band profile and the charge density in the device. Using the finite difference method, a two-dimensional Poisson equation is solved to obtain the electrostatic potential in the device. Simultaneously, a one-dimensional Schrodinger equation is solved using the scattering matrix method.

Knowledge of the CNT bandstructure is required for this simulation method. The CNT bandstructure is obtained by folding the two-dimensional graphene bandstructure onto a one-dimensional Brillouin zone of the CNT. In the following section the bandstructure calculation starting from the analysis of a single layer of graphene strip is performed.

2.1.1 Graphene

Graphene is made up of carbon atoms that are arranged in a planar hexagonal lattice structure [6]. Each carbon atom has four electrons in the outer shell three of which hybridize to form the directed orbitals that result in the hexagonal lattice structure. The single electron remaining occupies the pi-orbital that sticks out of the plane. All the single electrons from the individual carbon atoms are free to move around in the plane, and they are responsible for the electronic properties of graphene.

The bandstructure of graphene was obtained using a tight-binding Hamiltonian, which describes the movement of electrons along the hexagonal lattice structure of graphene [6].

Bandstructure of Graphene [3]

The lattice structure of graphene is shown in Fig. 2.1.

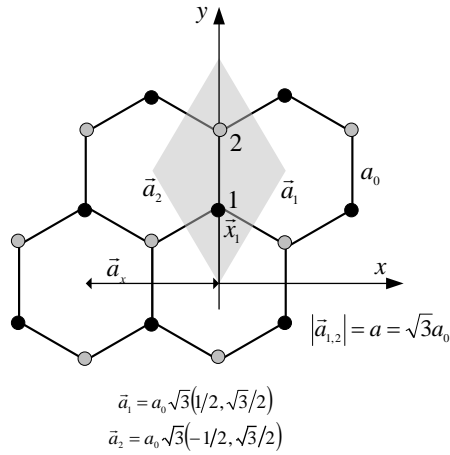


Figure 2.1: Graphene Lattice. The carbon atoms are illustrated using the shaded nodes and the chemical bonds represented by the lines are derived from the sp^2 -orbitals. The primitive lattice vectors are $\vec{a}_{1,2}$ and the unit-cell is the shaded region. There are two carbon atoms per unit-cell, represented by 1 and 2.

The electronic properties of graphene are derived from the fourth valence electron not used for the sp^2 bonds. In terms of atomic orbitals, the fourth electron occupies the p_z orbital, and there are two such electrons per unit cell, leading to two π -bands. Based on the lattice structure shown in Fig. 2.1, the lattice vectors $\vec{a}_{1,2}$ are written in the (x, y) basis as:

$$\vec{a}_1 = a_0\sqrt{3}(1/2, \sqrt{3}/2) \quad (2.1)$$

$$\vec{a}_2 = a_0\sqrt{3}(-1/2, \sqrt{3}/2) \quad (2.2)$$

where a_0 is the nearest-neighbour distance ($a_0 = 1.42\text{\AA}$). The p_z atomic-orbitals are oriented perpendicular to the plane and they have rotational symmetry around the z -axis.

The Ansatz wavefunction is given by:

$$\psi_{\vec{k}} = \sum_{\vec{R} \in G} e^{i\vec{k} \cdot \vec{R}} \phi(\vec{x} - \vec{R}) \quad (2.3)$$

where G is a set of lattice vectors and $\phi(\vec{x})$ is the atomic wavefunction. There are two p_z orbitals per unit cell, and their corresponding wavefunctions are defined as ϕ_1 and ϕ_2 , where

the index refers to their respective carbon atom. The total wavefunction, ϕ is a linear combination of ϕ_1 and ϕ_2 .

$$\phi(\vec{x}) = b_1\phi_1(\vec{x}) + b_2\phi_2(\vec{x}) \quad (2.4)$$

where b_1 and b_2 are integers. The tight-binding Hamiltonian for a single electron in the atomic potential, V_{at} is given by:

$$H = \frac{\vec{p}^2}{2m} + \sum_{\vec{R} \in G} \left(V_{at}(\vec{x} - \vec{x}_1 - \vec{R}) + V_{at}(\vec{x} - \vec{x}_2 - \vec{R}) \right) \quad (2.5)$$

where \vec{x}_1 and \vec{x}_2 represent the positions of the two carbon atoms within the unit cell. Multiplying Eq. 2.5 by ϕ_1 , gives:

$$H\phi_1 = \epsilon_1\phi_1 + \left(\sum_{\vec{R} \neq 0} \left(V_{at}(\vec{x} - \vec{x}_1 - \vec{R}) + V_{at}(\vec{x} - \vec{x}_2 - \vec{R}) \right) + V_{at}(\vec{x} - \vec{x}_2) \right) \phi_1 \quad (2.6)$$

where ϵ_1 is the eigenvalue of the atomic p_z state. The second section of Eq. 2.6 is abbreviated by $\Delta U_1\phi_1$ yielding:

$$H\phi_{1,2} = \epsilon_{1,2}\phi_{1,2} + \Delta U_{1,2}\phi_{1,2} \quad (2.7)$$

Eq. 2.7 can be simplified further by noting that $\epsilon_1 = \epsilon_2$ and that the energy can be set to zero. Choosing $\epsilon_{1,2} = 0$, Eq. 2.7 becomes:

$$H\phi_1 = \Delta U_1\phi_1 \quad (2.8)$$

$$H\phi_2 = \Delta U_2\phi_2 \quad (2.9)$$

Now, solve the Schrodinger equation:

$$H\psi_{\vec{k}} = E(\vec{k})\psi_{\vec{k}} \quad (2.10)$$

Since there are two parameters, b_1 and b_2 , two equations are required for this eigenvalue problem. These equations are obtained by projecting ψ on the two states ϕ_1 and ϕ_2 yielding [6]:

$$E(\vec{k})\langle\phi_{1,2}|\psi\rangle = \langle\phi_{1,2}|\Delta U_{1,2}|\psi\rangle \quad (2.11)$$

To calculate $\langle\phi_1|\psi\rangle$ and $\langle\phi_2|\psi\rangle$, only the nearest-neighbour overlap integrals are taken into account to obtain the two equations:

$$\langle\phi_1|\psi\rangle = b_1 + b_2(\int\phi_1^*\phi_2)(1 + e^{-i\vec{k}\cdot\vec{a}_1} + e^{-i\vec{k}\cdot\vec{a}_2}) \quad (2.12)$$

$$\langle\phi_2|\psi\rangle = b_2 + b_1(\int\phi_2^*\phi_1)(1 + e^{i\vec{k}\cdot\vec{a}_1} + e^{i\vec{k}\cdot\vec{a}_2}) \quad (2.13)$$

Assume that the overlap integral is real:

$$\gamma_0 = \int\phi_1^*\phi_2 \in R \quad (2.14)$$

To calculate $\langle\phi_{1,2}|\Delta U_{1,2}|\psi\rangle$, only the nearest-neighbour overlap integrals are taken into account. Use the abbreviation:

$$\gamma_1 = \int\phi_1^*\Delta U_1\phi_2 = \int\phi_2^*\Delta U_2\phi_1 \quad (2.15)$$

The following two equations are obtained:

$$\langle\phi_1|\Delta U_1|\psi\rangle = b_2\gamma_1(1 + e^{-i\vec{k}\cdot\vec{a}_1} + e^{-i\vec{k}\cdot\vec{a}_2}) \quad (2.16)$$

$$\langle\phi_2|\Delta U_1|\psi\rangle = b_1\gamma_1(1 + e^{i\vec{k}\cdot\vec{a}_1} + e^{i\vec{k}\cdot\vec{a}_2}) \quad (2.17)$$

Putting all these equations together (i.e. Eq. 2.11, 2.12, 2.13, 2.16 and 2.17), and using the abbreviation $\beta(\vec{k})$, the eigenvalue problem is reduced to:

$$\begin{pmatrix} E(\vec{k}) & \beta(\gamma_0 E(\vec{k}) - \gamma_1) \\ \beta^*(\gamma_0 E(\vec{k}) - \gamma_1) & E(\vec{k}) \end{pmatrix} \begin{pmatrix} b_1 \\ b_2 \end{pmatrix} = \begin{pmatrix} 0 \\ 0 \end{pmatrix} \quad (2.18)$$

$$\beta(\vec{k}) = \left(1 + e^{-i\vec{k} \cdot \vec{a}_1} + e^{-i\vec{k} \cdot \vec{a}_2} \right) \quad (2.19)$$

The dispersion relation $E(\vec{k})$ is obtained from Eq. 2.18 by setting the determinant to zero. Making use of the fact that γ_0 is small, obtain as an approximation, the dispersion relation:

$$E(\vec{k}) = \pm \gamma_1 |\beta(\vec{k})| \quad (2.20)$$

The magnitude of β is calculated from Eq. 2.19 and used to solve Eq. 2.20. The dispersion relation becomes:

$$E(\vec{k}) = \pm \gamma_1 \sqrt{3 + 2\cos(\vec{k} \cdot \vec{a}_1) + 2\cos(\vec{k} \cdot \vec{a}_2) + 2\cos(\vec{k} \cdot (\vec{a}_2 - \vec{a}_1))} \quad (2.21)$$

Based on the lattice structure shown in Fig. 2.1, the dispersion relation is expressed in a different form using the (x, y) components for \vec{k} :

$$E(k_x, k_y) = \pm \gamma_1 \sqrt{1 + 4\cos\left(\frac{\sqrt{3}ak_y}{2}\right)\cos\left(\frac{ak_x}{2}\right) + 4\cos^2\left(\frac{ak_x}{2}\right)} \quad (2.22)$$

where a is the lattice constant ($a = \sqrt{3}a_0$).

Fig. 2.2 shows a three-dimensional (3D) plot of the bandstructure of graphene. The conduction and valence states in graphene only meet at singular points in k-space called K points. The dispersion around these points is conical.

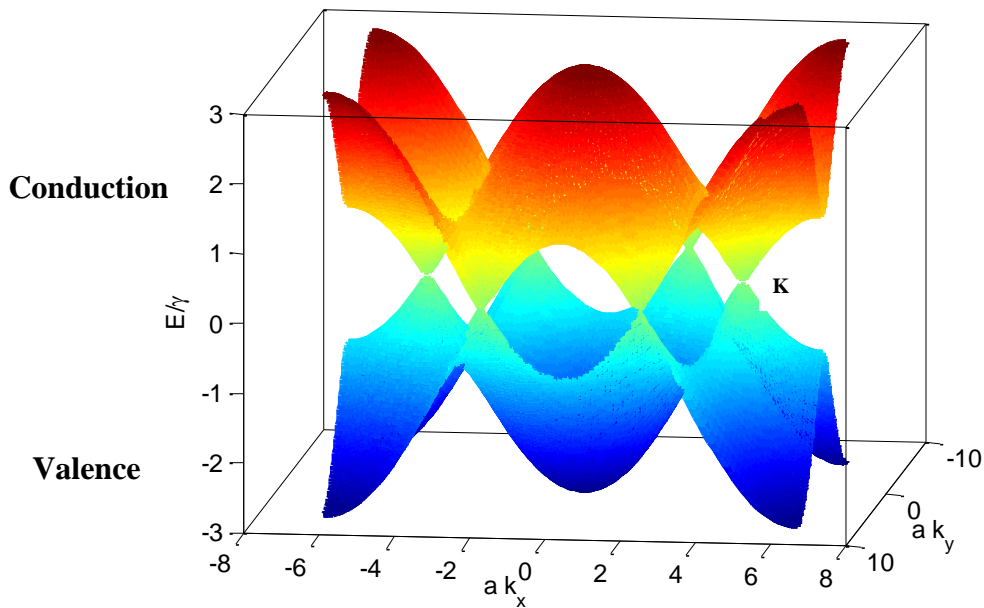


Figure 2.2: The dispersion relation of graphene. The conduction and valence states meet at K-points.

In the next section, we describe the electronic states of a CNT are described by combining the electronic properties of graphene with cylindrical boundary conditions.

2.1.2 Carbon Nanotubes

Having described graphene in section 2.1.1, carbon nanotubes, which are cylindrical structures based on graphene are now discussed. Their dimensions are typically a few nanometers in diameter and up to $100\mu\text{m}$ long. Fig. 2.3b shows a CNT formed by rolling up a graphene sheet.

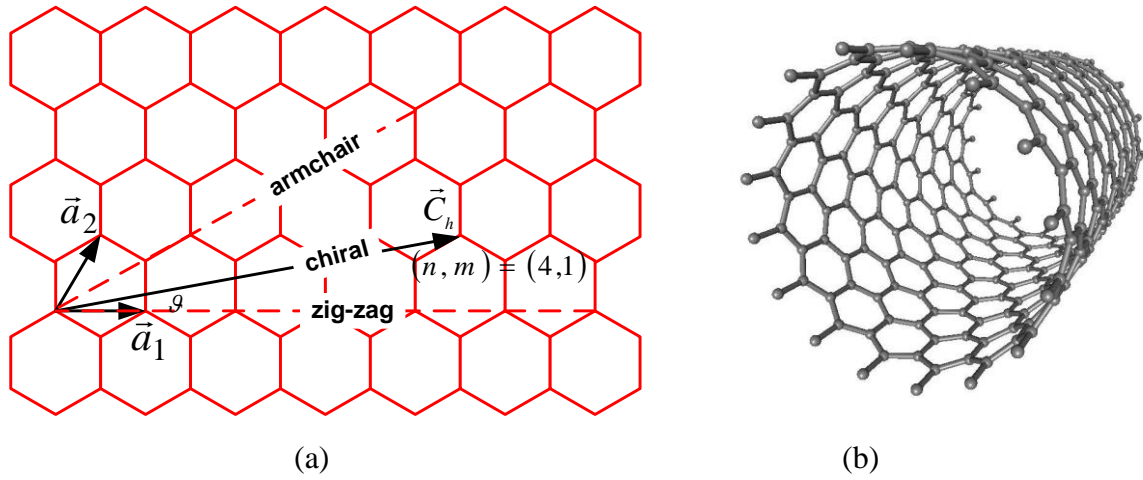


Figure 2.3: (a) Hexagonal lattice structure of a graphene sheet, (b) carbon nanotube formed by rolling up a graphene sheet [6][7].

The rolling up of a graphene sheet can be described in terms of the chiral (wrapping) vector C_h , which connects two sites of the two-dimensional (2D) graphene sheet that are crystallographically equivalent:

$$C_h = n\vec{a}_1 + m\vec{a}_2 \quad (2.23)$$

where \vec{a}_1 and \vec{a}_2 are the unit vectors of hexagonal graphene lattice separated by 60 degrees and the indices (n, m) are positive integers ($0 \leq m \leq n$) that specify the chirality of the tube.

As shown in Fig. 2.3, the chiral vector starts and ends at equivalent lattice points. The tube is formed by rolling up the chiral vector so that its head and tail join, forming a ring around the tube. The length of the chiral vector is the circumference of the tube, and the radius of the tube, R_t is given by:

$$R_t = \frac{|C_h|}{2\pi} = \frac{a_{cc}\sqrt{3(n^2+m^2+nm)}}{2\pi} \quad (2.24)$$

The number of atoms per nanometer-length on a single-walled nanotube is given by [4]:

$$N_{atoms} \approx 2 \frac{A_{cyl}}{A_{hex}} \frac{1}{L_t} = \frac{8\pi R_t L_t}{3\sqrt{3}a_{cc}^2} \frac{1}{L_t} \approx 240R_t \quad (2.25)$$

where A denotes area, and L_t is the length of the nanotube.

CNTs can be further divided into different groups depending on their (n, m) indices. These groups are named based on the shape of the cross-section established by the chiral vector slicing across the hexagonal pattern. The groups are armchair nanotube ($n = m$ and $\vartheta = 30^\circ$), zig-zag nanotube ($m = 0$ and $\vartheta = 0$) and chiral (other cases), where ϑ is the angle between C_h and \vec{a}_1 .

The microstructures of CNTs have mostly been observed using Transmission Electron Microscopy (TEM). Detailed analysis of the microstructures of CNTs shows that their electrical properties (Semiconductor or Metal) depend on the structure of the graphitic sheet [7]. A CNT can be either metallic or semiconducting depending on the indices that specify the chirality of the tube. A CNT is metallic if $2m + n = 3p$, where p is a positive integer. Otherwise, it is semiconducting. The electrical properties of a CNT also depend on the separation between the energy of valence and conduction states. The energy gap of a metallic CNT is zero while that of a semiconducting CNT is nonzero.

Bandstructure of Carbon Nanotubes

The bandstructure of a CNT can be approximated using the zone-folding method ZFM [8]. In this approach, the rolled up graphene restricts the available wave vector space. A diagram of a zig-zag nanotube is shown in Fig. 2.4.

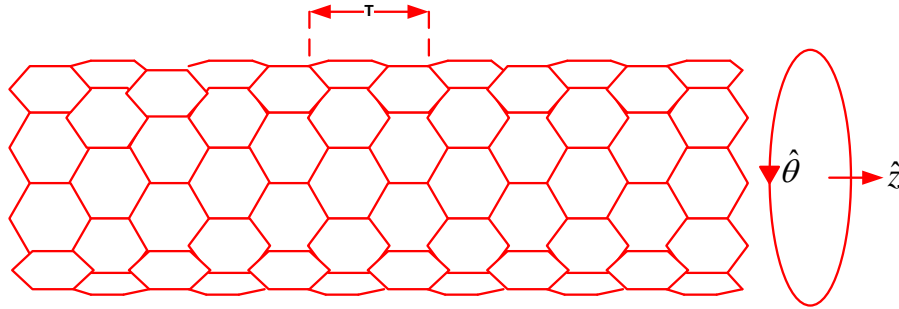


Figure 2.4: A zig-zag carbon nanotube, where T represents the length of the unit cell.

The wave vectors along the tube axis are continuous and restricted differently to that of graphene because the length of the CNT unit cell is larger in this direction. Significant confinement of the electron eigenvectors allows only discrete wave vector values in the direction perpendicular to the tube axis. The electron is therefore treated as a wave packet of Bloch states along the axis of the tube [7].

Fig. 2.5 shows the Brillouin zone for a $n = 16$ zig-zag nanotube. The CNT Brillouin zone is a collection of N 1D slices through the k -space of graphene. The length of each 1D slice is $2\pi/T$, where T represents the length of the CNT unit cell, and N represents the number of graphene unit cells within a single CNT unit cell.

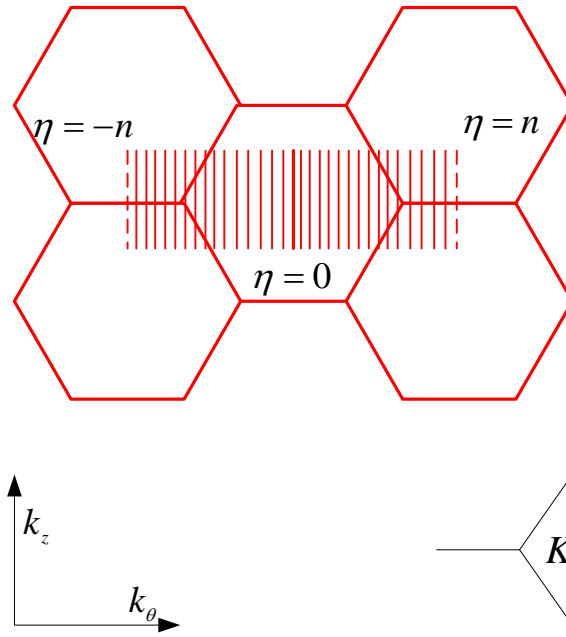


Figure 2.5: Brillouin zone for a zig-zag ($n = 16$) nanotube super-imposed on graphene k -space. The wave vectors along the nanotube axis and perpendicular direction are represented by k_z and k_θ , respectively. The dash lines at the ends are for zone boundaries and they count as a single slice.

For each of the $2n$ graphene unit cells within the zig-zag CNT unit cell, there is only one discrete value for the wave vector perpendicular to the axis of the nanotube. Each band of graphene is then broken into $2n$ subbands in the CNT. The electron wave vector for a zig-zag nanotube with a diameter d is:

$$\hat{k} = (k_z, \eta) = k_z \hat{z} + \frac{2\eta}{d} \hat{\theta} \quad (\eta = -n, \dots, n) \quad (2.26)$$

where the electronic quantum number η represents the confinement along $\hat{\theta}$. At $\eta = \pm n$, the wave vectors are treated as one shared zone boundary wave vector. If it is assumed that the length of the nanotube is very long, the z component along the nanotube axis k_z can be treated as continuous. The electronic subbands are degenerate for $\pm\eta$. As shown in Fig. 2.5, this degeneracy in η corresponds to two equivalent valleys in the subband structure each centred near a graphene K-point.

Electron conduction is within the delocalized π orbitals along the nanotube axis. For this calculation, the subbands produced from the π -antibonding band of graphene is required. The bandstructure of CNT is calculated from the π -orbital nearest-neighbour tight-binding bandstructure of graphene (described in section 2.1.1). The energy dispersion for a zig-zag nanotube is:

$$E(\hat{k}) = E(k_z, \eta) = \pm \gamma_1 \sqrt{1 \pm 4 \cos\left(\frac{T k_z}{2}\right) \cos\left(\frac{\pi \eta}{n}\right) + 4 \cos^2\left(\frac{\pi \eta}{n}\right)} \quad (2.27)$$

$$-\frac{\pi}{T} < k_z < \frac{\pi}{T}$$

For the zone-folding method, the conduction electron wavefunction is [7]:

$$\psi_{\hat{k}} = \sum_{\hat{k}} \langle \hat{r} | \hat{k} \rangle = \frac{1}{\sqrt{2\pi L_t}} \sum_{k_z \eta} e^{i(k_z z + \eta \theta)} \phi_{k_z \eta}(z, \theta) \quad (2.28)$$

where L_t is the length of the CNT and ϕ represents the graphene π -antibonding orbitals normalized over the graphene unit cell.

In the later stage of this chapter, the simulation of electron transport in a CNT at low applied fields is described. Therefore, the electronic bandstructure of the first few subbands are required. The E - k relation of the first three subbands is described using Eq. 2.29 [8].

$$\frac{\hbar^2 k_z^2}{2m_b^*(n)} = [E_b - E_b^m(n)] \{1 + \alpha_b(n)[E_b - E_b^m(n)]\} \quad (2.29)$$

where b is the subband index ($b = 1, 2, 3$), $E_b^m(n)$ is the energy minimum, $m_b^*(n)$ is the effective mass and $\alpha_b(n)$ is the nonparabolicity factor of subband b . Table 2.1 shows the details of Eq. 2.29 parameters. These parameters are a function of the nanotube index because they are related to the diameter of the nanotube.

Subbands	Energy Minimum	Effective Mass	Nonparabolicity Factor
Subband 1	$E_1^m(n) = \frac{\pi\gamma}{\sqrt{3}n}$	$m_1^*(n) = \frac{3m_e}{n\gamma} \left(1 - 0.0044n + \frac{\gcd(n+1,3) - \gcd(n-1,3)}{n} \right)$	$\alpha_1(n) = \frac{3}{2\gamma} (0.3n - 1)$
Subband 2	$E_2^m(n) = 2E_1^m(n) \left(1 + \frac{\gcd(n-1,3) - \gcd(n+1,3)}{3n} \right)$	$m_2^*(n) = m_1^*(n) \left(\frac{E_2^m(n)}{E_1^m(n)} + \frac{5}{n} \left[\frac{E_2^m(n)}{E_1^m(n)} [\gcd(n-1,3) - 1] - [\gcd(n+1,3) - 1] \right] \right)$	$\alpha_2(n) = \frac{3}{2\gamma} (0.2n - 1)$
Subband 3	$E_3^m(n) = 4E_1^m(n) \left(1 + \frac{1 + 2\gcd(n+1,3) - 3\gcd(n-1,3)}{4n} \right)$	$m_3^*(n) = m_1^*(n) \left(\frac{E_3^m(n)}{E_1^m(n)} + \frac{5}{n} \left[\frac{E_3^m(n)}{E_1^m(n)} [\gcd(n+1,3) - 1] - [\gcd(n-1,3) - 1] \right] \right)$	$\alpha_3(n) = \frac{3n^2}{300\gamma}$

Table 2.1: The bandstructure properties of the first three subbands, where $\gcd(i, j)$ is the greatest common divisor of i and j [8].

Having provided a detailed atomic description of CNTs, the modelling techniques used to simulate electron transport in CNTs at low applied fields are now discussed.

2.2 Modelling Techniques

In this section, the simulation techniques used in our work are introduced. The CNFET model described in section 2.3 is based on a self-consistent solution of Poisson and Schrodinger equations. The Poisson equation is solved using a two-dimensional finite difference method (described in section 2.2.1), and the Schrodinger equation is solved using the scattering matrix method (described in section 2.2.2).

2.2.1 Finite Difference Method

The finite difference method can be used to solve a Laplace equation in cylindrical coordinates (ρ, ϕ, z) [9]. In cylindrical coordinates, the Laplace equation is written as:

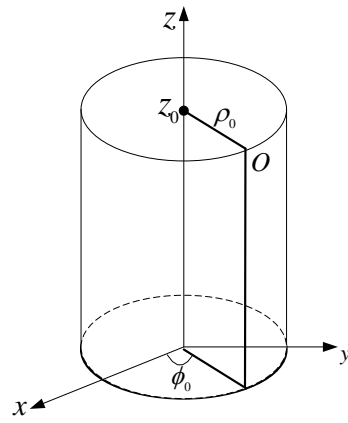
$$\nabla^2 V = \frac{\partial^2 V}{\partial \rho^2} + \frac{1}{\rho} \frac{\partial V}{\partial \rho} + \frac{1}{\rho^2} \frac{\partial^2 V}{\partial \phi^2} + \frac{\partial^2 V}{\partial z^2} = 0 \quad (2.30)$$

The equivalent finite difference approximation at point $O(\rho_0, r_0, z_0)$ is:

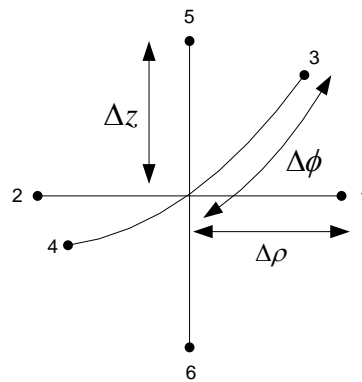
$$\frac{V_1 - 2V_0 + V_2}{(\Delta\rho)^2} + \frac{1}{\rho_0} \frac{V_1 - V_2}{2\Delta\rho} + \frac{V_3 - 2V_0 + V_4}{(\rho_0\Delta\phi)^2} + \frac{V_5 - 2V_0 + V_6}{(\Delta z)^2} = 0 \quad (2.31)$$

where $\Delta\rho$, $\Delta\phi$ and Δz are the step sizes along ρ , ϕ and z , respectively. Eq. 2.31 is derived from the cylindrical coordinates shown in Fig. 2.6.

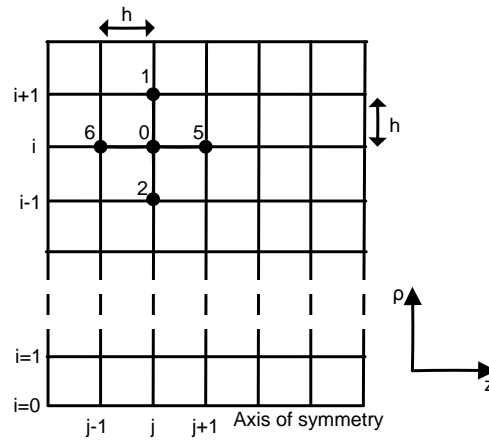
$$\begin{aligned} V_0 &= V(\rho_0, \phi_0, z_0), & V_1 &= V(\rho_0 + \Delta\rho, \phi_0, z_0), & V_2 &= V(\rho_0 - \Delta\rho, \phi_0, z_0), \\ V_3 &= V(\rho_0, \phi_0 + \rho_0\Delta\phi, z_0), & V_4 &= V(\rho_0, \phi_0 - \rho_0\Delta\phi, z_0), \\ V_5 &= V(\rho_0, \phi_0, z_0 + \Delta z), & V_6 &= V(\rho_0, \phi_0, z_0 - \Delta z) \end{aligned} \quad (2.32)$$



(a)



(b)



(c)

Figure 2.6: (a), (b) - Typical nodes in cylindrical coordinates and (c) Finite difference grid for an axisymmetric system.

For an axisymmetric system such as the one described in Fig. 2.6, there is no dependence of ϕ , so $V = V(\rho, z)$. Assuming square nets i.e. $\Delta p = \Delta z = h$, the solution region becomes discretized. Eq. 2.31 becomes:

$$\left(1 + \frac{h}{2\rho_0}\right) V_1 + \left(1 - \frac{h}{2\rho_0}\right) V_2 + V_5 + V_6 - 4V_0 = 0 \quad (2.33)$$

Set a point at $(\rho_0, z_0) = (ih, jh)$ to give:

$$1 + \frac{h}{2\rho_0} = \frac{2i+1}{2i}, \quad 1 - \frac{h}{2\rho_0} = \frac{2i-1}{2i} \quad (2.34)$$

$$V(i, j) = \frac{1}{4} \left[V(i, j-1) + V(i, j+1) + \left(\frac{2i-1}{2i}\right) V(i-1, j) + \left(\frac{2i+1}{2i}\right) V(i+1, j) \right] \quad (2.35)$$

There is singularity at $\rho_0 = 0$ and by symmetry, all odd order derivatives must be zero:

$$\left. \frac{\partial V}{\partial \rho} \right|_{\rho=0} = 0 \quad (2.36)$$

$$V(\Delta\rho, z_0) = V(-\Delta\rho, z_0) \quad (2.37)$$

By L'Hopital's rule,

$$\lim_{\rho_0 \rightarrow 0} \left. \frac{1}{\rho_0} \frac{\partial V}{\partial \rho} \right|_{\rho=0} = \left. \frac{\partial^2 V}{\partial \rho^2} \right|_{\rho_0} \quad (2.38)$$

The Laplace's equation becomes:

$$2 \frac{\partial^2 V}{\partial \rho^2} + \frac{\partial^2 V}{\partial z^2} = 0 \quad (2.39)$$

Applying finite difference to Eq. 2.39 gives:

$$V_0 = \frac{1}{6} (4V_1 + V_5 + V_6) \quad (2.40)$$

$$V(0, j) = \frac{1}{6} [V(0, j - 1) + V(0, j + 1) + 4V(1, j)] \quad (2.41)$$

To solve the Poisson equation in cylindrical coordinates, replace the zero on the right hand side of the Laplace equation with the term $g = Q_v/\epsilon$.

$$V(i, j) = \frac{1}{4} \left[V(i, j + 1) + V(i, j - 1) + \frac{2i-1}{2i} V(i - 1, j) + \frac{2i+1}{2i} V(i + 1, j) - gh^2 \right] \quad (2.42)$$

where ϵ is the permittivity, h is the step size and Q_v is the charge density.

To treat an interface between two media, the boundary condition $D_{1n} = D_{2n}$ must be imposed at the interface, where D is the electric displacement field.

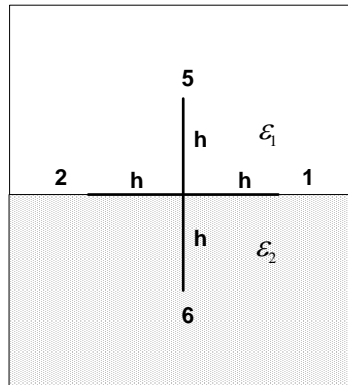


Figure 2.7: Interface between two different media.

Applying Taylor series expansion to points 1, 2 and 5 in medium 1 of Fig. 2.7, gives:

$$\begin{aligned} V_1 &= V_0 + \frac{\partial V_0^{(1)}}{\partial \rho} h + \frac{\partial^2 V_0^{(1)}}{\partial \rho^2} \frac{h^2}{2} + \dots \\ V_2 &= V_0 - \frac{\partial V_0^{(1)}}{\partial \rho} h + \frac{\partial^2 V_0^{(1)}}{\partial \rho^2} \frac{h^2}{2} - \dots \end{aligned} \quad (2.43)$$

$$V_5 = V_0 + \frac{\partial V_0^{(1)}}{\partial z} h + \frac{\partial^2 V_0^{(1)}}{\partial z^2} \frac{h^2}{2} + \dots$$

where superscript (1) denotes medium 1. Summing Eq. 2.30 and Eq. 2.43, gives:

$$h^2 \nabla^2 V = V_1 + V_2 + 2V_5 - 4V_0 - 2h \frac{\partial V_0^{(1)}}{\partial z} + \frac{h(V_1 - V_2)}{2\rho_0} = 0 \quad (2.44)$$

$$\frac{\partial V_0^{(1)}}{\partial z} = \frac{V_1 + V_2 + 2V_5 - 4V_0 + \frac{h(V_1 - V_2)}{2\rho_0}}{2h} \quad (2.45)$$

Also, applying the Taylor series to points 1, 2, and 6 in medium 2, gives:

$$V_1 = V_0 + \frac{\partial V_0^{(2)}}{\partial \rho} h + \frac{\partial^2 V_0^{(2)}}{\partial \rho^2} \frac{h^2}{2} + \dots$$

$$V_2 = V_0 - \frac{\partial V_0^{(2)}}{\partial \rho} h + \frac{\partial^2 V_0^{(2)}}{\partial \rho^2} \frac{h^2}{2} - \dots \quad (2.46)$$

$$V_6 = V_0 - \frac{\partial V_0^{(2)}}{\partial z} h + \frac{\partial^2 V_0^{(2)}}{\partial z^2} \frac{h^2}{2} + \dots$$

Summing Eq. 2.30 and Eq. 2.46 yields:

$$h^2 \nabla^2 V = V_1 + V_2 + 2V_6 - 4V_0 - 2h \frac{\partial V_0^{(2)}}{\partial z} + \frac{h(V_1 - V_2)}{2\rho_0} = 0 \quad (2.47)$$

$$-\frac{\partial V_0^{(2)}}{\partial z} = \frac{V_1 + V_2 + 2V_6 - 4V_0 + \frac{h(V_1 - V_2)}{2\rho_0}}{2h} \quad (2.48)$$

Applying the boundary condition $D_{1n} = D_{2n}$ or $\varepsilon_1 \frac{\partial V_0^{(1)}}{\partial z} = \varepsilon_2 \frac{\partial V_0^{(2)}}{\partial z}$ and solving for V_0 gives:

$$V_0 = \frac{1}{4} \left(1 + \frac{h}{2\rho_0} \right) V_1 + \frac{1}{4} \left(1 - \frac{h}{2\rho_0} \right) V_2 + \frac{\varepsilon_1}{2(\varepsilon_1 + \varepsilon_2)} V_5 + \frac{\varepsilon_2}{2(\varepsilon_1 + \varepsilon_2)} V_6 \quad (2.49)$$

Having covered the finite difference method used for solving the Poisson equation, the scattering matrix method used for solving the Schrodinger equation is now described.

2.2.2 Scattering Matrix Method

Classical physics describes the macroscopic world but quantum mechanics describes the microscopic world of atoms and molecules. Phase randomizing scattering dominates macroscopic devices so quantum interference effects can be ignored [10]. However, for very small devices there is a need to use a wave approach to electron transport.

In this work, electron transport in the mesoscopic regime, which is a size scale between microscopic and macroscopic, is studied. Consider a structure connected to metallic contacts as shown in Fig. 2.8.

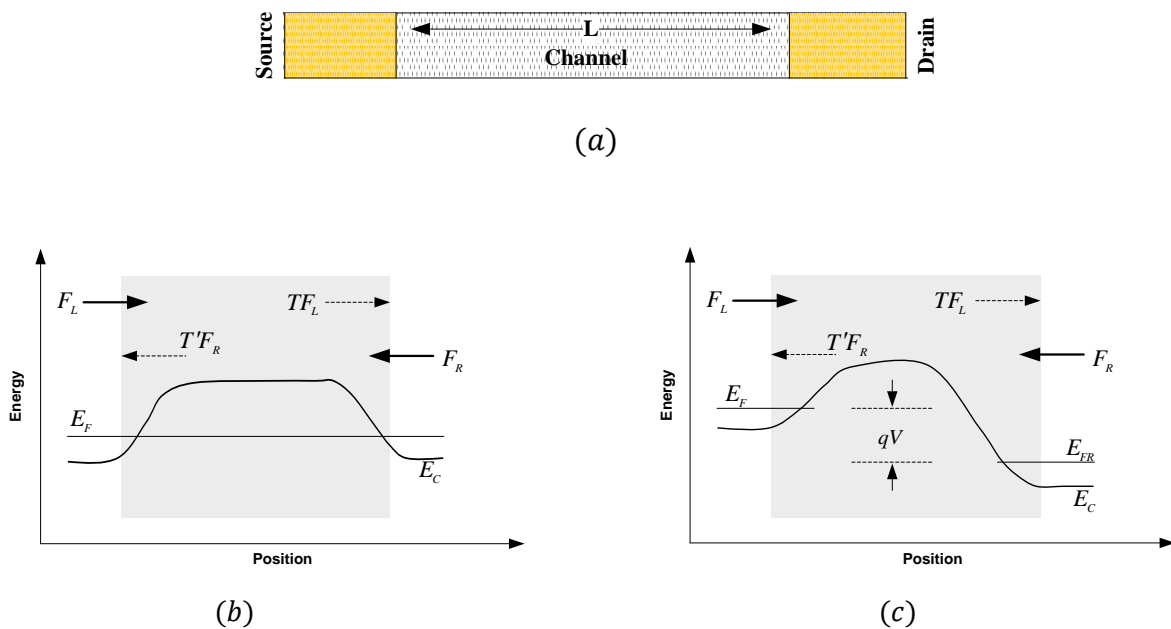


Figure 2.8: Flux of carriers injected from each contact into the device (a). A fraction of the flux from both sides transmits across the device (b) Equilibrium and (c) Under bias.

The end contacts inject a flux of electrons into the structure. The entire device is then described by its transmission coefficients, T and T' , and the net flux through the device is:

$$F_{net} = TF_L - T'F_{R'} \quad (2.50)$$

where F_L and F_R are the fluxes injected from the left and right contacts, respectively. The transmission coefficients for the device are determined using a semi-classical calculation.

The scattering matrix theory is derived in terms of carrier fluxes and their backscattering probabilities [10]. Consider a semiconductor slab with a finite thickness Δz , as shown in Fig. 2.9. Assuming steady state conditions, $a(z)$ and $b(z)$ are the position-dependent, steady state, right- and left-directed fluxes. There is a right-directed flux incident on the left face of the slab and a left-directed flux incident on the right face.

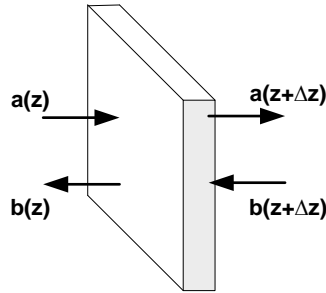


Figure 2.9: Fluxes of charge carriers incident upon and reflected from a slab of finite thickness.

In this example, fluxes $b(z)$ and $a(z + \Delta z)$ that emerge from the slab are to be determined. These fluxes can be expressed in scattering matrix form, which relates both fluxes emerging from the slab to the two incident fluxes on the slab:

$$\begin{pmatrix} a(z + \Delta z) \\ b(z) \end{pmatrix} = \begin{bmatrix} T & 1 - T' \\ 1 - T & T' \end{bmatrix} \begin{pmatrix} a(z) \\ b(z + \Delta z) \end{pmatrix} \quad (2.51)$$

where T and T' denote the fraction of the steady-state right- and left-directed fluxes transmitted across the slab.

The scattering theory can be applied to the device shown in Fig. 2.8. In this case, the device is divided into a set of thin slabs connected so that the output fluxes from one slab provide the input fluxes to its neighbouring slabs. The two fluxes injected from the left and right contacts are used as the boundary conditions. Fig. 2.10 shows two interconnected scattering matrices.

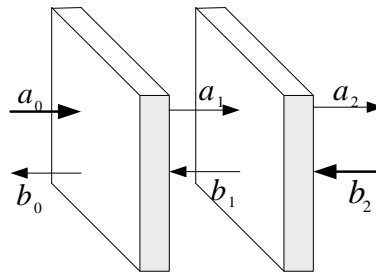


Figure 2.10: Two scattering matrices cascaded to produce a single, composite scattering matrix.

Taking only the fluxes emerging from the set of two scattering matrices, a_2 and b_0 into account, the two scattering matrices can be replaced by a single scattering matrix. Assume that the two scattering matrices have transmission elements t_1, t'_1, t_2 and t'_2 . The elements of the composite scattering matrix are:

$$\begin{aligned}
 t_{21} &= t_1[1 - r'_2 r_2]^{-1} t_2 \\
 r_{21} &= r_1 + t'_1 r_2 [1 - r'_1 r_2]^{-1} t_1 \\
 r'_{21} &= r'_2 + t_2 [1 - r'_1 r_2]^{-1} r'_1 t'_2 \\
 t'_{21} &= t'_1 [1 - r'_1 r_2]^{-1} t'_2
 \end{aligned} \tag{2.52}$$

where $r_1 = 1 - t_1$, etc. Eq. 2.52 describes the multiple reflection processes that occur when a flux coming from the left or right, transmits across the first slab then backscatters and reflects from the interiors of the two slabs.

In real applications, the device is divided into a finite number of scattering matrices. These matrices are then cascaded two at a time until the entire device is described by a single scattering matrix. Once this matrix is computed, the current through the device is determined by subtracting the right- and left-directed fluxes.

In the next section, this modelling technique is applied to a MOS device based on a semiconducting CNT. The electronic properties of the device are determined from the fluxes evaluated throughout the device.

2.3 A Two-Dimensional Simulation of Carbon Nanotube Field-Effect Transistors

In this section, the simulation of electron transport in a semiconducting nanotube using the CNFET structure is described. Accurate modelling of CNFETs requires a self-consistent solution of the Poisson and Schrodinger equations. The quantum mechanical treatment of electron transport is included by solving a one-dimensional Schrödinger equation.

CNFETs are devices with a gate wrapped around the gate dielectric and the nanotube [11]. Here, the coaxial geometry of the CNFET is considered due to the cylindrical nature of CNTs. Fig. 2.11 shows the structure of the CNFET device described in this work.

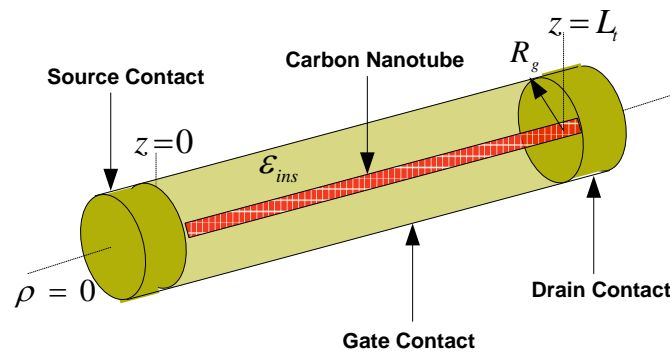


Figure 2.11: The Coaxial Carbon Nanotube FET Geometry.

Since the source and drain contacts have the same radius as the gate contact, the metallic cylinder is closed and the simulation technique that is based on a numerical method employed by John *et. al* [5] is used to solve for the parameters of the closed system. The device shown in Fig. 2.11 consists of a semiconducting nanotube surrounded by an insulator with relative permittivity ϵ_{ins} and a cylindrical, wrap-around gate contact. The ends of the device are terminated by the source and drain contacts. The device dimensions include the gate radius R_g , the nanotube radius R_t , the insulator thickness $t_{ins} = R_g - R_t$, and the device length L_t .

In this closed metallic cylinder system, Poisson's equation is restricted to just two dimensions by azimuthal symmetry. To fully specify the geometry of this device, the Poisson's equation as a function of polar and cylindrical coordinates shown in Fig. 2.12, is derived (refer to Appendix 3).

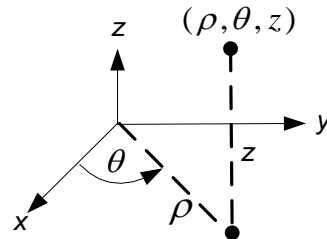


Figure 2.12: Cylindrical Coordinates.

In cylindrical coordinates, the Poisson's equation restricted to two dimensions by azimuthal symmetry is:

$$\frac{\partial^2 V}{\partial \rho^2} + \frac{1}{\rho} \frac{\partial V}{\partial \rho} + \frac{\partial^2 V}{\partial z^2} = -\frac{Q}{\epsilon} \quad (2.53)$$

where $V(\rho, z)$ is the potential within the outer cylinder, ϵ is the permittivity and Q is the charge density. Although the solution to Eq. 2.53 encompasses the entire volume of the

device, the longitudinal potential profile $V_{cnt}(z) \equiv V(R, z)$ along the surface of the nanotube is mainly required. Knowledge of this potential is required for the carrier transport calculations.

The solution to Eq. 2.53 is obtained via the finite difference method, which is implemented by discretizing the spatial domain and using central differencing to generate a linear system of equations for some known charges, and subject to the boundary conditions. The boundary conditions for the CNFET device are:

$$V_s = -\frac{\varphi}{q} \quad (2.54)$$

$$V_g = V_s + V_{gs} \quad (2.55)$$

$$V_d = V_s + V_{ds} \quad (2.56)$$

where φ is the work function, q is the electron charge, V_{gs} is the gate-source voltage and V_{ds} is the drain-source voltage. In our system, we replace the values of the potential at the device boundaries with the boundary conditions shown in Eq. 2.54 - Eq. 2.56. A detailed procedure for computing the electrostatic potential within the CNFET structure is described in Appendix 4.

The charge distribution on the surface of the nanotube is obtained by solving the Poisson equation coupled with the time-independent Schrödinger equation:

$$\frac{\partial^2 \Psi}{\partial z^2} = -\frac{2m^*}{\hbar^2} (E - U)\Psi = -k^2 \Psi \quad (2.57)$$

where $\Psi(E, x)$ is the wavefunction of the carrier with an Energy E , m^* is the effective mass obtained from the bandstructure of the zig-zag nanotube and U is the local effective potential seen by the carriers.

$$U = qV_{cnt} - X_{cnt} \quad (2.58)$$

where X_{cnt} is the electron affinity of CNT.

The charge density in the CNFET device is given by:

$$Q = \frac{q(p-n)}{2\pi} \frac{\delta(\rho-R_t)}{\rho} \quad (2.59)$$

where $\delta(\cdot)/\rho$ is the Dirac delta function in cylindrical coordinates, n and p are computed from the Schrodinger equation. A numerical solution of Eq. 2.57 is found at any given energy E . Schrodinger's equation is solved using the scattering matrix method in which a numerical solution is propagated by cascading 2×2 matrices as described in section 2.2.2.

A detailed description of the grid implementation for the model device is provided in Appendix 5. The entire system is divided into N grids and for each grid the electron wavefunction Ψ is expressed as:

$$\Psi_n = A_n e^{ik_n z} + B_n e^{-ik_n z} \quad (2.60)$$

where k is the wavevector, A and B are the amplitudes of the wavefunctions. The wavefunction and its derivative are matched on the boundary between intervals n and $n + 1$ using the relations:

$$\Psi_n = \Psi_{n+1} \quad (2.61)$$

$$\frac{\partial \Psi_n}{\partial z} = \frac{\partial \Psi_{n+1}}{\partial z} \quad (2.62)$$

As described in section 2.2.2, the relationship between $[A_n B_n]^T$ and $[A_{n+1} B_{n+1}]^T$ is obtained using:

$$\begin{bmatrix} A_{n+1} \\ B_n \end{bmatrix} = S_n \begin{bmatrix} A_n \\ B_{n+1} \end{bmatrix} \quad (2.63)$$

where $[A_n B_n]^T$ is the transpose of the matrix $[A_n B_n]$, S_n is the scattering coefficient, Ψ_1 and Ψ_N are the wavefunctions in the source and drain contacts, respectively. When computing the wavefunctions for the source injection, the amplitude of the wavefunction at the drain end is set to zero. An analogous calculation is performed when considering the drain injection.

The Landauer equation is expected to hold for the flux and the probability current I_P equated to the Landauer current I_L [12]:

$$I_P(E) = \frac{q\hbar}{2m} i \left[\left(\frac{\partial \Psi}{\partial z} \right)^* \Psi - \Psi^* \left(\frac{\partial \Psi}{\partial z} \right) \right] \quad (2.64)$$

$$I_L(E) = \frac{q}{\pi\hbar} f_s(E) T(E) \quad (2.65)$$

$$\frac{2q}{\pi\hbar} f_s T = \frac{q\hbar}{m^*} k_N |A_N|^2 \quad (2.66)$$

where f_s is the Fermi-Dirac carrier distribution in the source and T is the transmission probability described by:

$$T = \frac{k_N |A_N|^2}{k_1 |A_1|^2} \quad (2.67)$$

The normalization condition is:

$$|A_1| = \frac{2m f_s}{\pi\hbar^2 k_1} \quad (2.68)$$

The total carrier density in the system is computed from the normalized wavefunctions. In order to obtain the carrier distribution along the surface of the nanotube, Ψ is integrated over all possible energy levels.

$$n(z) = \int_{E_{min}}^{E_{max}} (|\Psi_{e,S}|^2 + |\Psi_{e,D}|^2) dE \quad (2.69)$$

$$p(z) = \int_{E_{min}}^{E_{max}} (|\Psi_{h,S}|^2 + |\Psi_{h,D}|^2) dE \quad (2.70)$$

where E_{min} is the bottom of the energy band, E_{max} is the vacuum energy level, $\Psi_{e,S}$ is the electrons source injection, $\Psi_{e,D}$ is the electrons drain injection, $\Psi_{h,S}$ is the holes source injection, and $\Psi_{h,D}$ is the holes drain injection. Eq. 2.69 and Eq. 2.70 can be solved using the right-point rectangle rule [13] or the adaptive Simpson's method [14].

The right-point rectangle rule is expressed as:

$$\int_a^b f(x) dx \approx \sum_{i=1}^{\infty} f(a + i\Delta x) \Delta x \quad (2.71)$$

In this approach, the interval $[E_{min}, E_{max}]$ is simply divided into equidistant points and the Schrodinger equation is solved at these points. This method can only give an accurate result if a large number of points are allocated within the intervals. This will require an extremely large computing time to achieve a converged carrier density. Narrow resonances of the wavefunction may occur at certain energy levels when the potential profile on the CNT channel changes. These narrow resonances will lead to a sudden change of the carrier concentration and result in longer simulation time or even worse an oscillated and non-converged charge density. This problem can be avoided by using a numerical integration method that refines the grid in the region of resonances.

The integrations were performed using the adaptive Simpson's method with different subdivided intervals defined [14]. The adaptive Simpson's method is expressed as:

$$I_1 = \int_a^b f(x)dx = \frac{h}{6}(f(a) + 4f(c) + f(b)) \quad (2.72)$$

$$I_2 = \int_a^c f(x)dx + \int_c^b f(x)dx = \frac{h}{12}(f(a) + 4f(d) + 2f(c) + 4f(e) + f(b)) \quad (2.73)$$

$$\text{where } c = \frac{a+b}{2} \quad d = \frac{a+c}{2} \quad e = \frac{c+b}{2}$$

If $|I_2 - I_1|/15 < \varepsilon$, where ε is a predefined tolerance, the algorithm calls for further division of the integration interval into two, and the adaptive Simpson's method is applied to each subinterval in a recursive manner. In this approach, the points in the integration intervals are non-equidistant, so there are many points around the resonances while there are only few points in other regions.

Simulation Procedure

To start the simulation, the initial charge density inside the device is guessed, usually zero. The next step is to compute the electron potential inside the device by solving Poisson's equation. The new charge density in the device is computed by using the scattering matrix method to solve the Schrodinger equation. This new charge density is then used to solve the Poisson equation again and these steps are repeated a number of times until the new value of the charge density match the older one. At this point, the criterion for convergence of the system is achieved and other properties of the device are observed via numerical integrations. Fig. 2.13 shows the flow chart of the simulation procedure.

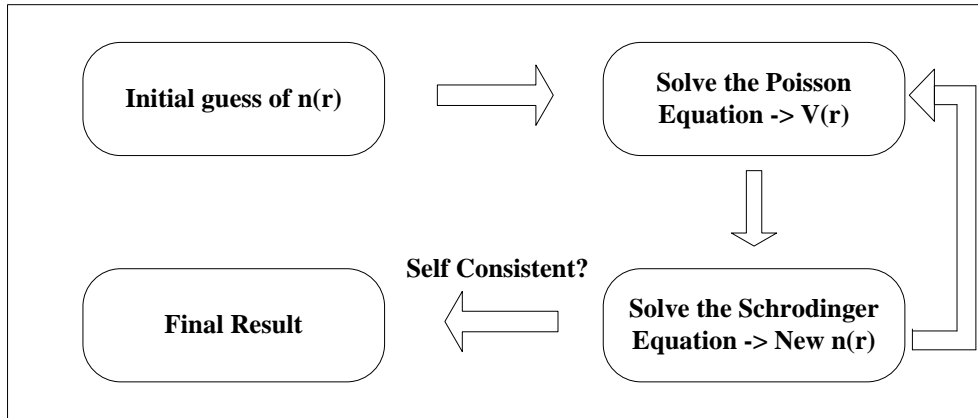


Figure 2.13: Iterative procedure for computing electrostatics and charge transport self-consistently.

2.4 Simulation Results

The carbon nanotube used for this simulation is a zig-zag nanotube with indices ($n = 16, m = 0$). The nanotube diameter R_t is $0.63nm$ and the corresponding bandgap is $0.62eV$. Other parameters of the device include the nanotube length $L_t = 20nm$, dielectric thickness $t_{ins} = 2.5nm$ and $\epsilon_{ins} = 25$. The nanotube ends are terminated with silver (Ag) contacts having a work function ϕ of $4.5eV$. The electron affinity χ_{cnt} is $4.2eV$, and the nanotube is presumed to have a free-space relative permittivity ($\epsilon_t = 1$). The electron effective mass m_* is calculated from the bandstructure properties of the nanotube (as described in table 2.1) and it is $0.0311m_0$ for both electrons and holes [6][7], where m_0 is the free electron mass.

Now, the result of a simulation based on the theory described in section 2.3 is analysed. Fig. 2.14 shows the conduction band profile when the applied gate voltage is varied. A positive gate bias pulls the conduction band down, allowing more propagating modes in the channel.

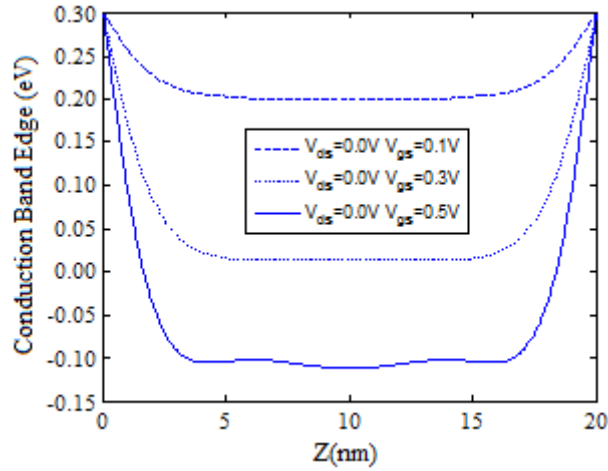


Figure 2.14: Simulation of the potential energy seen by the electrons at different gate bias for the equilibrium condition ($V_{ds} = 0V$). Conduction band edge along the length of the device for $V_{gs} = 0.1V$, $V_{gs} = 0.3V$ and $V_{gs} = 0.5V$.

The potential profile for applied $V_{ds} = 0V$ and $0.4V$ is shown in Fig. 2.15. Fig. 2.16 shows the electron density when the drain-source voltage V_{ds} is varied and a constant gate-source voltage V_{gs} of $0.5V$ is applied. The electrons in the channel are from the source and drain contacts and they are drawn into the nanotube by tunneling through the barriers at the contacts. When the system is in equilibrium ($V_{ds} = 0$), the charge carrier concentration is evenly distributed throughout the device, following the shape of the conduction band profile. Interference effects on the charge distributions are observed when the system is out of equilibrium. The electron concentration in the channel reduces as V_{ds} increases because evanescent states dominate the electron concentrations near the device contacts and the effect is seen on the local potential.

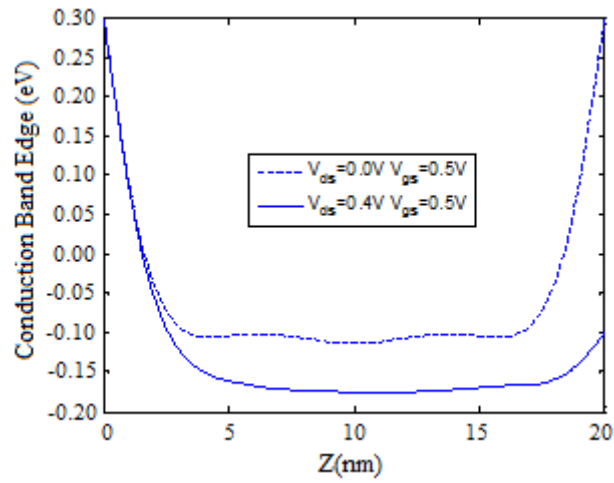


Figure 2.15: Conduction band edge along the device length for $V_{gs} = 0.5V$, $V_{ds} = 0V$ and $V_{ds} = 0.4V$. The energies are with respect to the source Fermi level.

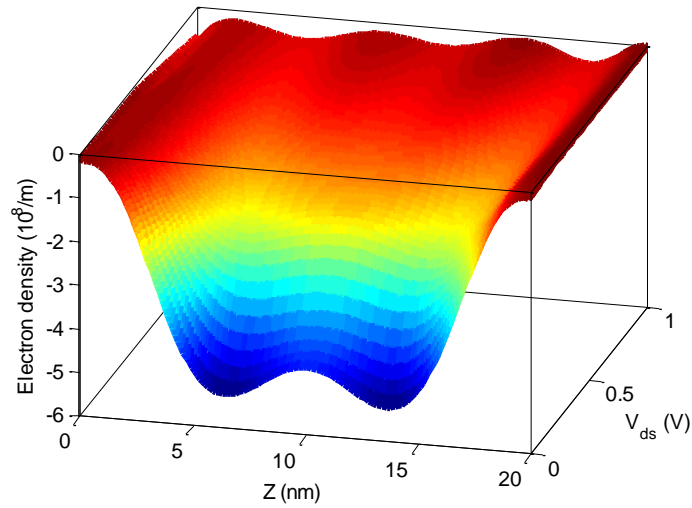


Figure 2.16: Simulation of the carrier density as a function of position and varying V_{ds} when $V_{gs} = 0.5V$.

The simulation method allows the inclusion of quantum mechanical reflection for the thermionic component of the flux. The total carrier distribution within the nanotube is determined by the action of reflections at the barriers near the contacts on the injected carriers. Carriers above the potential barrier are often assumed to have a transmission probability closed to unity. This approximation does not hold in general since there is a significant reflection when the minimum integration energy (taken to be $5.5eV$ below the metal Fermi level [5]) is much lower than the conduction band edge. As shown in Fig. 2.17, for energies that are well above the barrier height, the transmission coefficient is oscillatory approaching unity as E becomes large.

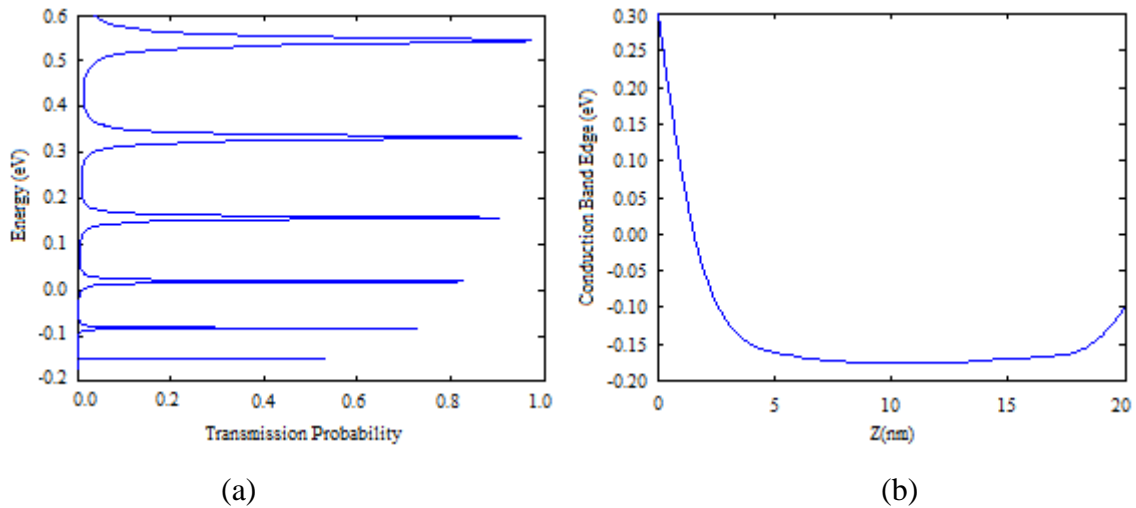


Figure 2.17: Transmission probabilities for electrons (a), and the corresponding conduction band edge (b) at $V_{gs} = 0.5V$ and $V_{ds} = 0.4V$.

Fig. 2.18 shows the drain I-V characteristics for the model device. For an applied gate bias of $0.5V$, the nanotube saturation current is achieved at a drain bias of $0.2V$. The reflecting action at the nanotube-drain interface limits the expected full saturation current of $3.3\mu A$. There is a significant reflection when the minimum integration energy is much lower than the conduction band edge.

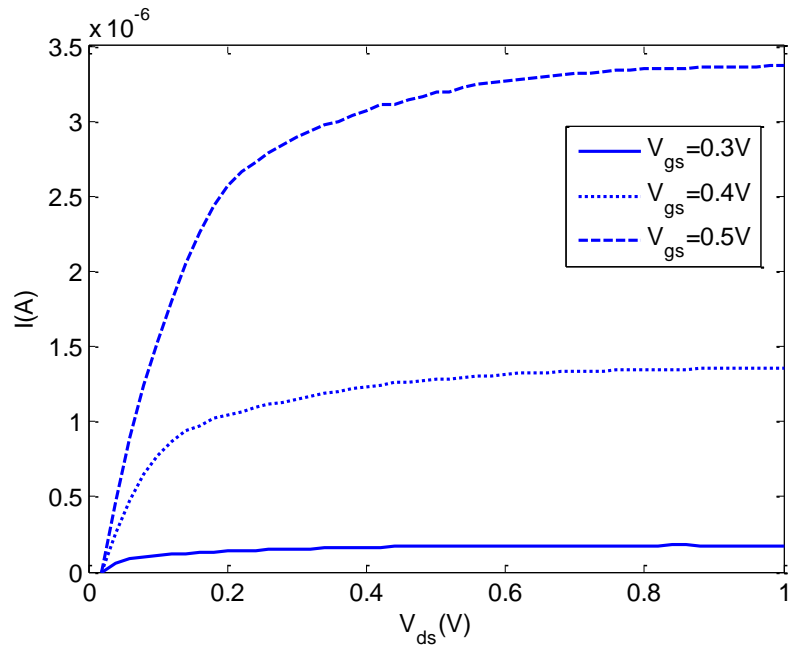


Figure 2.18: The I-V characteristics of the zig-zag nanotube for different gate bias.

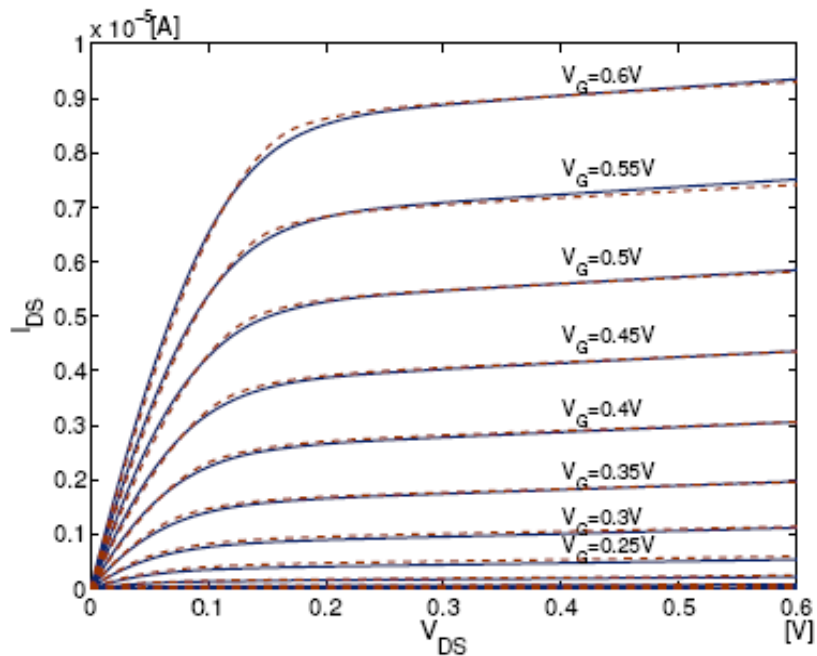


Figure 2.19: Drain current characteristics for the nanotube based on the FETtoy model [15]

Fig. 2.19 shows the output characteristics for the nanotube based on the FETtoy model. The I-V characteristics obtained in this work is comparable to those calculated using other simulation methods [15][16][17]. As shown in Fig. 2.18, the device current also saturates at a drain bias of around 0.2V when the gate bias is 0.5V. The slight difference in both output characteristics is that the maximum current drive achieved for the gate bias of 0.5V is higher for the FETtoy model. This difference may be due to numerical evaluation of integrals in both models using different approach. In this work, the adaptive Simpson's method was employed while the Newton-Raphson was used in the FETtoy model.

The saturation current depends on how the barriers at the source and drain contacts are treated. In the next section, the role of the metallic contacts on the transport properties of the zig-zag nanotube is investigated.

2.4 Role of the Metal-Carbon Nanotube Contact in Computing Electron Transport in Carbon Nanotubes

The current in the device on-state is one of the most important characteristics of the CNT device. The I-V characteristics of CNFETs with different metal contacts and the metallic contact that gives the highest on-current is identified.

In MOS devices, contacts play an important role in their performance and a lot of work has been done to control their effects on electron transport [18][19][20][21]. CNFETs have produced on-currents ranging from $10^{-5}A$ to $10^{-8}A$ because the electrodes used to terminate the CNTs are different [22].

In addition, experimental results show a variation in on-currents of approximately 3-4 orders of magnitude for different metal contacted CNTs [22]. The magnitude of the on-currents was

observed to be dependent on the work functions of the metal used to terminate the nanotube [22]. The variation in on-currents was linked to the electron injection into the nanotube, which is dependent on the line-up of the metal Fermi level and the conduction band in the nanotube.

Another experimental issue is that a nanotube could be end-bonded to the metal as shown in Fig. 2.20a or it could lay on the metal surface and be side-contacted as shown in Fig. 2.20b. The contact geometry realised defines the coupling strength, which influences electron transport at the metal/nanotube interface [19][23].

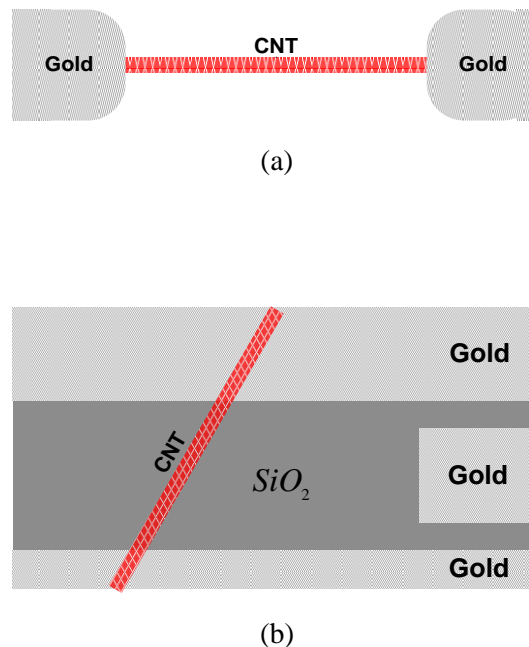


Figure 2.20: (a) A carbon nanotube ‘end bonded’ to the metal, (b) a carbon nanotube forming ‘side contacts’ on gold electrodes

Here the performance of CNFETs modelled with different metallic contacts is analysed. Silver (*Ag*), Iron (*Fe*) and Gold (*Au*) are the metals used for this simulation. The work functions for *Ag*, *Fe* and *Au* are $4.5eV$, $4.8eV$ and $5.2eV$, respectively. As before, the Poisson and Schrodinger equations are self-consistently solved using finite difference

technique and scattering matrix method, respectively. The transmission probability for the electrons is then computed from the solution of the Schrodinger equation. Since the metal/nanotube interface introduces boundary conditions in the solution of the Schrodinger equation, the transmission probability is dependent on the metal work function.

Simulation Results

The transport properties of the zig-zag nanotube are examined when different metal contacts terminate its ends. Electron transport from the metal contact into the nanotube is dominated by quantum mechanical tunnelling, thereby increasing the resistance of the contact. The conduction band profile is analysed and we look closely at the barriers near the end contacts. At the metal/nanotube interface, the barrier height depends on the metal work function.

Fig. 2.21 shows the conduction band edge for the CNFETs with different metal contacts. The band bending occurs over a length scale known as the Debye length L_d . At this length scale, the electrons screen out the applied fields (refer to Appendix 7 for details). In the devices, when $V_{gs} = 1V$ and $V_{ds} = 0.4V$, L_d is approximately $5nm$, $6nm$ and $7nm$ for *Ag*, *Fe* and *Au* contacts, respectively.

The device current depends on L_d and the barrier height at the metal/nanotube interface. If L_d is small, electrons tunnel through the barriers at the contact more readily and this will lead to an increased current.

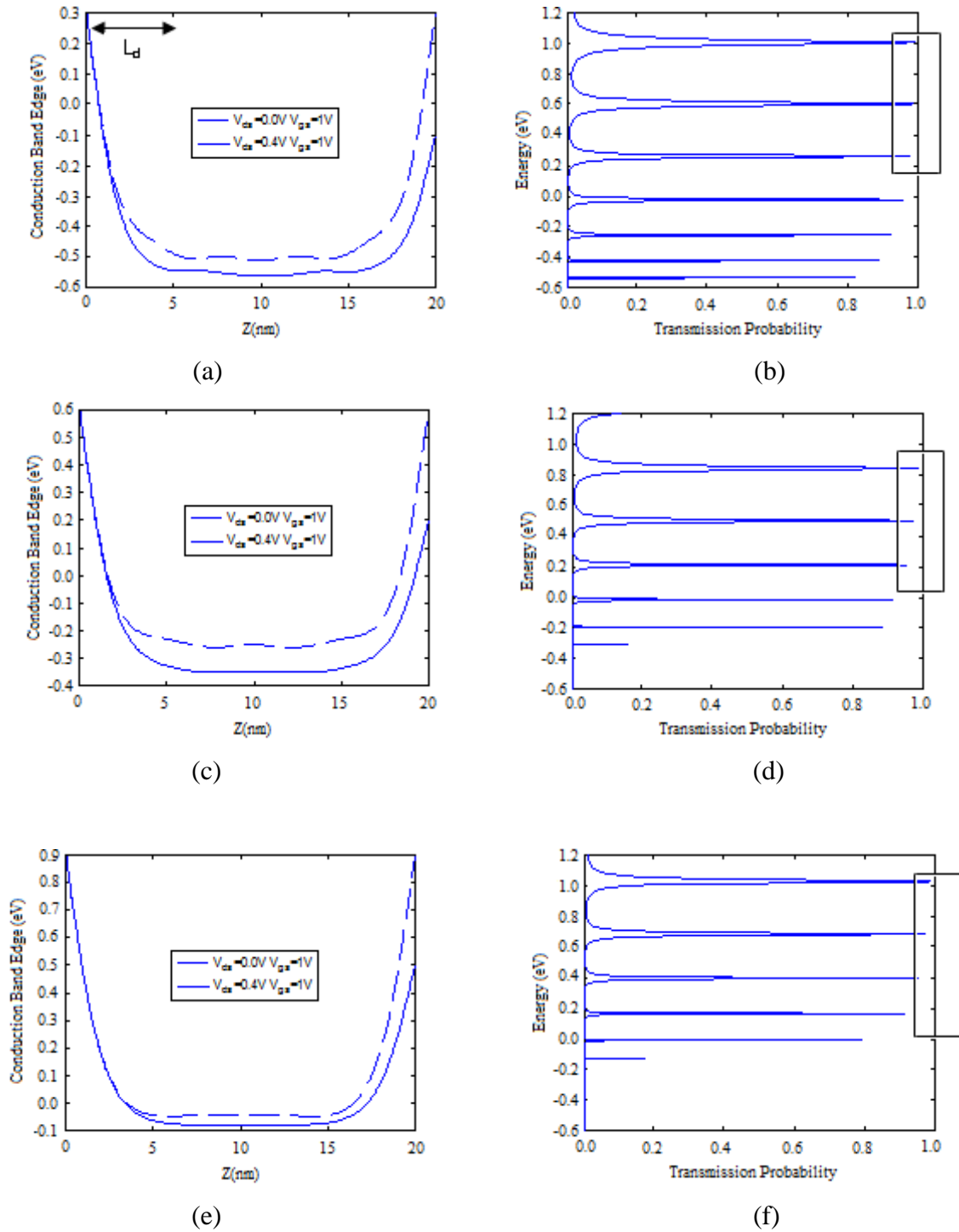


Figure 2.21: The band bending for the metal/nanotube junction at $V_{gs} = 1V$, $V_{ds} = 0V$, $V_{ds} = 0.4V$ and the transmission probability for electrons at $V_{ds} = 0.4V$, $V_{gs} = 1V$. [Ag with $\phi = 4.5eV$ - (a), (b)], [Fe with $\phi = 4.8eV$ - (c), (d)] and [Au with $\phi = 5.1eV$ - (e), (f)]. The band bending occurs over a length scale L_d .

As shown in Fig. 2.22, the on-currents of the zig-zag nanotube vary for different metal contacts. On comparing the I-V characteristics of the devices, it was observed that on-current is higher when *Ag* is used as the device contacts. This is expected as L_d and the barrier height for *Ag* are smaller when compared to those of *Fe* and *Au*. When *Au* is used as the metal contacts, the maximum current drive is achieved at a lower drain voltage compared to *Ag* and *Fe*. As shown in Fig. 2.22, a full current saturation is only achieved for *Ag* contacts but the current saturates at a larger drain voltage (0.5V). Based on the observed on-current and current saturation, an optimum CNFET performance is achieved when *Ag* is used as the nanotube end contacts.

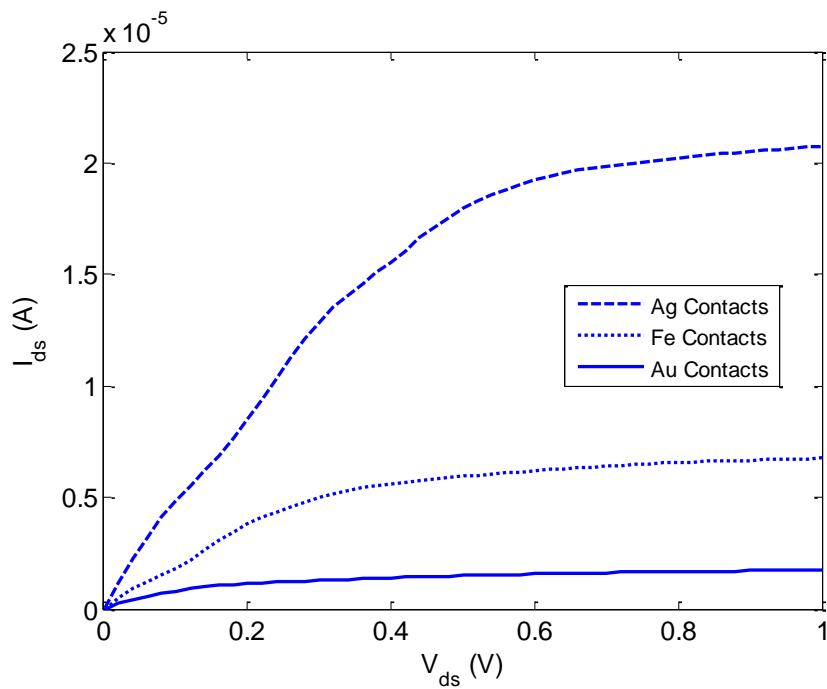


Figure 2.22: Plot of CNFETs I-V characteristics as a function of metal contacts at $V_{gs} = 1V$.

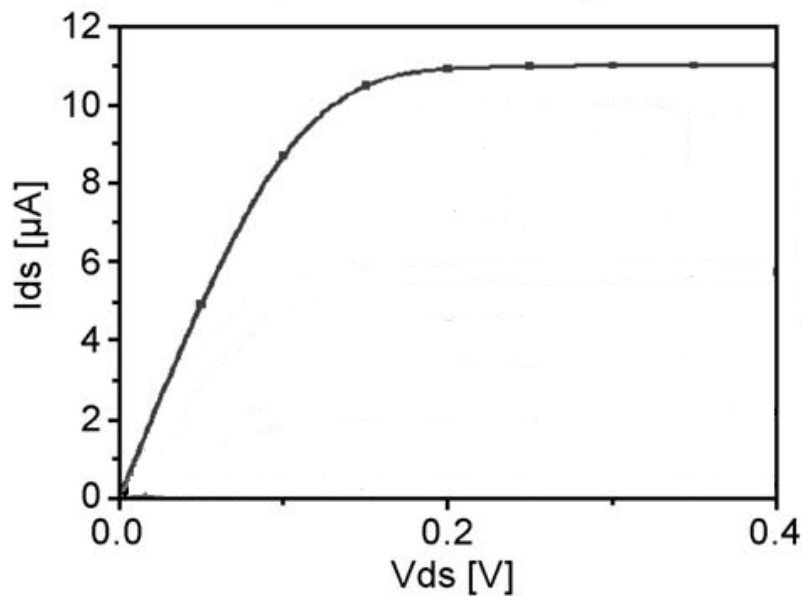


Figure 2.23: The ideal output characteristics of the device without contact effects [15].

The differences in the output characteristics of the devices can be understood from the relationship between the drain current I_{ds} and the transmission probability for electrons. As shown in Fig. 2.21, the transmission probability when the energy is greater than $0.2eV$ is higher for *Ag* and stays constant afterwards (as described by the spikes). However, the transmission probability for *Fe* and *Au* is still increasing for these energies, and this prevents full current saturation. The trends for the I-V characteristics follow that of the metal work functions. Therefore, the operation of CNFETs can be controlled by modulating the tunnelling barriers at the contacts. Fig. 2.23 shows the output characteristics of the device without the contact effects. In the ideal case, a full current saturation is achieved for a drain bias of around $0.2V$.

2.5 Conclusions

The bandstructure of graphene is calculated through a tight-binding Hamiltonian. Using the zone-folding method ZFM [8], the bandstructure of CNTs is obtained from the π -orbital nearest-neighbour tight-binding bandstructure of graphene [6].

Methods for modelling charge transport in a CNT have been discussed and illustrated using the Schrodinger-Poisson solver. Poisson's equation is solved self-consistently with Schrodinger's equation using the finite difference and scattering matrix techniques, respectively. The scattering matrix method enables resonance effects to be taken into account.

A fully wrapped around gate is assumed to improve immunity to short channel effects [24]. The drain I-V characteristics of the CNFET device suggest there is a reflecting action at the nanotube-drain contact interface influencing the current saturation of the device.

The role of metal-nanotube contacts in computing electron transport in CNTs has been investigated. Simulation results show that contacts play a dominant role in the performance of CNFETs. In the later stage of this thesis, electron transport in CNTs is investigated using a method that avoids the influence of metal contacts.

In the next Chapter, a simulation of electron transport in a graphene nanoribbon is described and its output characteristics compared to that of a CNFET.

2.6 References

- [1] Z. Chen, D. Farmer, S. Xu, R. Gordon, P. Avouris, and J. Appenzeller, Externally Assembled Gate-All-Around Carbon Nanotube Field-Effect Transistor, *IEEE Electron Device Letters*, Vol. 29, No. 2, February 2008.
- [2] T. Iwai, Y. Awano, Carbon Nanotube Bumps for Thermal and Electric Conduction in Transistor, *FUJITSU Sci. Tech. J.*, 43, 4, pp.508-515, October 2007.
- [3] H. Wei, N. Patil, A. Lin, H. S. Philip Wong, S. Mitra, Monolithic Three-Dimensional Integrated Circuits using Carbon Nanotube FETs and Interconnects, *Electron Devices Meeting (IEDM)*, December 2009 IEEE International, DOI: 10.1109/IEDM.2009.5424292.
- [4] G. F. Close, S. Yasuda, B. Paul, S. Fujita, and H. S. Philip Wong, A 1 GHz Integrated Circuit with Carbon Nanotube Interconnects and Silicon Transistors, *Nano Lett.*, 2008, 8 (2), pp 706–709.
- [5] D. L. John, L. C. Castro, P. J. S. Pereira, and D. L. Pulfrey, A Schrodinger-Poisson Solver for Modeling Carbon Nanotube FETs, *Proc. NSTI Nanotech*, vol. 3, pp. 65-68, 2004.
- [6] D. Gunlycke and C. T. White, Tight-binding energy dispersions of armchair-edge graphene nanostrips, *Physical Review B*, vol. 77, pp. 115-116, 2008.
- [7] M. S. Dresselhaus, G. Dresselhaus and Ph. Avouris (eds.), *Carbon Nanotubes Synthesis, Structure, Properties, and Applications (Topics in Applied Physics; v. 80)*, 2001, ISBN 3540410864.
- [8] G. Pennington and N. Goldsman, Semiclassical Transport and Phonon Scattering of Electrons in Semiconducting Carbon Nanotubes, *Phys. Rev. B* 68, 045426 (2003).
- [9] M. N.O. Sadiku, *Numerical Techniques in Electromagnetics*, CRC Press, Boca Raton, 1992.
- [10] M. Lundstrom, *Fundamentals of Carrier Transport*, Second Edition, Cambridge University Press, 2000.

- [11] L. C. Castro, D. L. John, and D. L. Pulfrey, An improved evaluation of the DC performance of carbon nanotube field-effect transistors, *Smart Mater. Struct.* 15 (2006) S9–S13.
- [12] D. L. Pulfrey, *Carbon Nanotube Field-Effect Transistors and their Possible Applications*, Nano Electronics Group, May 30, 2008, Pisa.
- [13] C. J. Zarowski, *An Introduction to Numerical Analysis for Electrical and Computer Engineers*, A John Wiley & Sons, Inc. Publication, ISBN - 0471467375, 2004.
- [14] M. Pourfath, H. Kosina, and S. Selberherr, A fast and stable Poisson-Schrodinger solver for the analysis of carbon nanotube transistors, *Journal of Computational Electronics*, vol. 5, pp. 155-159, 2006.
- [15] T. J Kazmierski, D. Zhou and B. M Al-Hashimi, A Fast, Numerical Circuit-Level Model of Carbon Nanotube Transistor, *Sch. of Electron. & Comput. Sci., Southampton Univ., Southampton, Nanoscale Architectures 2007, NANOSARCH 2007 IEEE International Symposium*, pp. 33-37.
- [16] A. Hazeghi, T. Krishnamohan, and H. S. Philip Wong, Schottky-Barrier Carbon Nanotube Field-Effect Transistor Modeling, *IEEE Transactions On Electron Devices*, Vol. 54, No. 3, March 2007.
- [17] T. J. Kazmierski, D. Zhou and B. M. Al-Hashimi, HSPICE implementation of a numerically efficient model of CNT transistor, *Forum on Specification and Design Languages (FDL 2009)*, September 22-24, 2009, Germany.
- [18] Z. Zhang, X. Liang, S. Wang, K. Yao, Y. Hu, Y. Zhu, Q. Chen, W. Zhou, Y. Li, Y. Yao, J. Zhang, and L.-Mao Peng, Doping-Free Fabrication of Carbon Nanotube Based Ballistic CMOS Devices and Circuits, *Nano Letters*, Vol. 7, No. 12, pp. 3603-3607, 2007.
- [19] P. Tarakeshwar, J. J. Palacios, and Dae M. Kim, Interface Study of Metal Electrode and Semiconducting Carbon Nanotubes: Effects of Electrode Atomic Species, *IEEE Transactions on Nanotechnology*, Vol. 7, No. 2, March 2008.
- [20] Y. He, J. Zhang, S. Hou, Y. Wang, and Z. Yu, Schottky barrier formation at metal electrodes and semiconducting carbon nanotubes, *Applied Physics Letters* 94, 093107, 2009.
- [21] K. Nagashio, T. Nishimura, K. Kita, and A. Toriumi, Contact resistivity and current flow path at metal/graphene contact, *Applied Physics Letters* 97, 143514, 2010.

- [22] S. Chu Lim, J. Ho Jang, D. Jae Bae, G. Hee Han, S. Lee, I. Yeo, and Y. Hee Lee, Contact resistance between metal and carbon nanotube interconnects: Effect of work function and wettability, *Applied Physics Letters* 95, 264103, 2009.
- [23] N. Peng, H. Li and Q. Zhang, Nanoscale Contacts between Carbon Nanotubes and Metallic Pads, *ACS Nano*, 3 (12), pp. 4117–4121, 2009.
- [24] Y. Ouyang, Y. Yoon, and J. Guo, Scaling Behaviors of Graphene Nanoribbon FETs: A Three-Dimensional Quantum Simulation Study, *Electron Devices, IEEE Transactions on*, vol. 54, pp. 2223-2231, 2007.

Chapter 3

Comparison of the Current-Voltage Characteristics of MOS Devices Based on Carbon Nanotubes and Graphene

3.1 Introduction

Simulations of the electronic properties of CNFETs suggest that they have great potential in future high speed electronic systems [2][3]. However, in practice, it is difficult to control the chirality of carbon nanotubes and the structures cannot readily be integrated into an electronic system. The chirality is important because the energy bandgap of a semiconducting CNT is a function of it [4].

Recently, graphene [5], which is a single sheet of graphite, has been created in the laboratory for the first time. Although graphene has been studied theoretically for many years it was thought to be too unstable to exist in its basic form. The discovery of stable graphene at the University of Manchester in 2004 has led to the realistic prospect of its utilization within electronic devices. The advantage of graphene is that it is compatible with the planar technology employed within the semiconductor industry. Like CNTs, graphene exhibits high electron mobilities [5], μ , in excess of $15,000\text{cm}^2/\text{Vs}$ and it can be metallic or semiconducting.

When tailored to less than 100nm wide graphene nanoribbons may open a band gap due to the electron confinement. Electronic states of the graphene nanoribbon largely depend on the edge structures and the width [6]. There are two main types of nanoribbon, known as

armchair-edge and zigzag-edge, depending on the arrangements of carbon atoms along the nanoribbon edges.

One of the most important potential applications of graphene is as the channel for electron transport in a MOS structure. Structures of this kind have been demonstrated experimentally [7] using epitaxially synthesized graphene on silicon carbide substrates. This work describes the simulation of an armchair-edge graphene based MOS transistor using a coupled Schrödinger-Poisson solver and compares the result with the characteristics of CNT based MOSFETs described in Chapter 2.

3.2 Model - Graphene Nanostrip Field Effect Transistors (GFETs)

A semiconducting armchair-edge graphene nanoribbon is used as the channel of the device to be modelled. The band structure is obtained through a tight-binding Hamiltonian of the armchair-edge nanoribbon that includes the summation of the first-nearest-neighbour (1NN) Hamiltonian, third-nearest-neighbour (3NN) Hamiltonian, 3NN truncation Hamiltonian and the 1NN edge distortion Hamiltonian [8].

Charge transport in graphene is investigated through the self-consistent solution of the charge and local electrostatic potential. The quantum mechanical treatment of electron transport is included by solving a one-dimensional (1D) Schrödinger's equation. A graphene field-effect transistor (GFET) based on the structure shown in the Fig. 3.1 is modelled. This device consists of a semiconducting nanoribbon with a wrap around gate at four faces of the rectangular geometry. A dielectric with relative permittivity ϵ_{ox} separates the semiconductor region of the device from the surrounding gate contact. The ends of the device are terminated by the source and drain contacts. Device parameters include the length (along x-direction) of the nanoribbon, its width (along z-direction) and the thickness of the insulator t_{ox} separating the graphene from the gate contact.

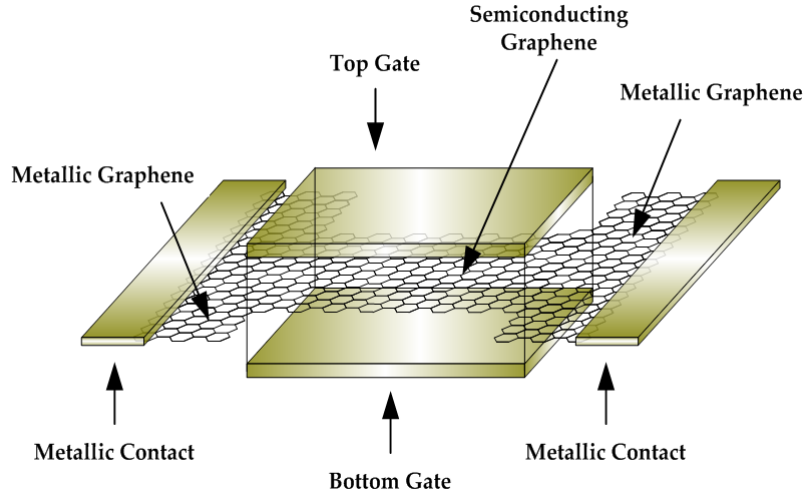


Figure 3.1: Cubical geometry of Graphene FET.

The potential profile in the entire model is obtained from the solution of the three-dimensional Poisson's equation in a rectangular system given by:

$$\left(\frac{\partial}{\partial x^2} + \frac{\partial}{\partial y^2} + \frac{\partial}{\partial z^2} \right) V(x, y, z) = -\frac{Q(x, y, z)}{\epsilon} \quad (3.1)$$

where $V(x, y, z)$ and $\rho(x, y, z)$ are the potential and charge density, respectively. The width of the nanoribbon is divided into unit cells allowing the graphene sheet to be treated as a quasi-one-dimensional conductor. The charge distribution on the surface of the material is obtained by solving the time-independent Schrödinger equation given by:

$$\frac{\partial^2 \Psi}{\partial x^2} = -\frac{2m^*}{\hbar^2} (E - U)\Psi = -k_G^2 \Psi \quad (3.2)$$

where $\Psi(x, E)$ is the wavefunction of the carrier having an energy E and m^* is the effective mass obtained from the bandstructure of the nanoribbon and is the same for both electrons and holes due to symmetry [9]. U is the local potential.

3.3 Device Simulation

The simulation is based on a numerical procedure employed by John et. al. [2]. Poisson's equation is solved using a finite difference method applying central differencing, forward differencing and backward differencing where applicable in the grid system. In matrix form Poisson's equation is written as

$$AV = -\frac{\Delta^2}{\epsilon}Q \quad (3.3)$$

where V and Q are the potential and charge density vectors, respectively, Δ is the length of the grid and A is a matrix generated from the finite difference method. Boundary conditions for the potential are defined by the terminal voltages and work functions.

The computed potential on the surface of the graphene sheet is defined by the vacuum level, $qV_{GRAPHENE}$. The potential energy seen by the electrons and holes is given by:

$$U_e(x) = -qV_{GRAPHENE} - E_{ea} \quad (3.4)$$

$$U_h(x) = U_e(x) + E_{gap} \quad (3.5)$$

where E_{ea} and E_{gap} are electron affinity and graphene band gap, respectively.

The charge distribution on the graphene surface is obtained by solving the Schrödinger equation using the scattering matrix. The charge density in the model device is given by

$$Q(x) = \frac{-q(n(x)-p(x))}{\Delta^3} \Delta \quad (3.6)$$

where q is the electron charge, $n(x)$ and $p(x)$ computed from Eq. 3.15 and Eq. 3.16 are the number of electrons and holes, respectively, in the graphene as a function of position. The

grid system used in the simulation is based on a series of $[2 \times 2]$ matrices; the wavefunction and its derivative are matched at the boundaries between the intervals n and $n + 1$ yielding a stable system [10]. The boundary conditions give:

$$\Psi_n = \Psi_{n+1} \quad (3.7)$$

$$\frac{\Psi_n}{\partial x} = \frac{\Psi_{n+1}}{\partial x} \quad (3.8)$$

Boundary conditions for the wavefunctions at the contacts are given by:

$$\Psi_1 = A_1 e^{ik_1 x_1} + B_1 e^{-ik_1 x_1} \quad (3.9)$$

$$\Psi_n = A_n e^{ik_n x_n} + B_n e^{-ik_n x_n} \quad (3.10)$$

where Ψ_1 and Ψ_n are the wavefunction at source and drain, respectively, A_1, B_1, A_n and B_n are the amplitudes of the wavefunctions and k_1, k_n are the wavevectors in the source and drain, respectively. The relationship between the amplitude of the wavefunctions $[A_n \ B_n]^T$ and $[A_{n+1} \ B_{n+1}]^T$ is given by the transfer matrix:

$$\begin{bmatrix} A_n \\ B_n \end{bmatrix} = M_n \begin{bmatrix} A_{n+1} \\ B_{n+1} \end{bmatrix} \quad (3.11)$$

The Landauer expression [10] holds for the flux and equals the probability current yielding:

$$\frac{q}{\pi \hbar} f_1 T_E = \frac{q \hbar}{m^*} k_n |A_n|^2 \quad (3.12)$$

where f_1 is the Fermi-Dirac carrier distribution in the source, and T_E is the transmission probability specified by:

$$T_E = \frac{k_n |A_n|^2}{k_1 |A_1|^2} \quad (3.13)$$

Substituting the expression for the transmission probability into the Landauer equation results in the normalization

$$|A_1| = \frac{m^* f_s}{\pi \hbar^2 k_s} \quad (3.14)$$

By including the source and drain injection components, the normalized wavefunction gives the total carrier density in the device. The carrier density on the graphene sheet is calculated by integrating Ψ over all possible energies levels.

$$n(x) = \int_{E_{min}}^{E_{max}} (|\Psi_{e,S}|^2 + |\Psi_{e,D}|^2) dE \quad (3.15)$$

$$p(x) = \int_{E_{min}}^{E_{max}} (|\Psi_{h,S}|^2 + |\Psi_{h,D}|^2) dE \quad (3.16)$$

Here E_{min} is the conduction band edge, E_{max} is the vacuum energy level, $\Psi_{e,S}$ and $\Psi_{e,D}$ are the electron wavefunctions within the source and drain, respectively while $\Psi_{h,S}$ and $\Psi_{h,D}$ are the equivalent wavefunctions for holes. The integration is performed using the procedure described in ref. 3.

Using a numerical damping factor, the coupled Schrödinger-Poisson equation model was solved iteratively. An initial assumption of zero charge Q^l on the graphene surface was made and the electrostatic potential V^l computed from Poisson's equation. A new charge density is computed Q_{int}^l using the calculated electrostatic potential V^l . The new charge density Q_{int}^{l+1} is used for the calculation of the new potential V_{int}^{l+1} and finally the new potential V^{l+1} is calculated as:

$$V^{l+1} = \alpha V_{int}^{l+1} + (1 - \alpha) V^l \quad (3.17)$$

where $0 < \alpha < 1$. The convergence of the system is achieved when the defined criterion is met (i.e. error less than 10^{-5}).

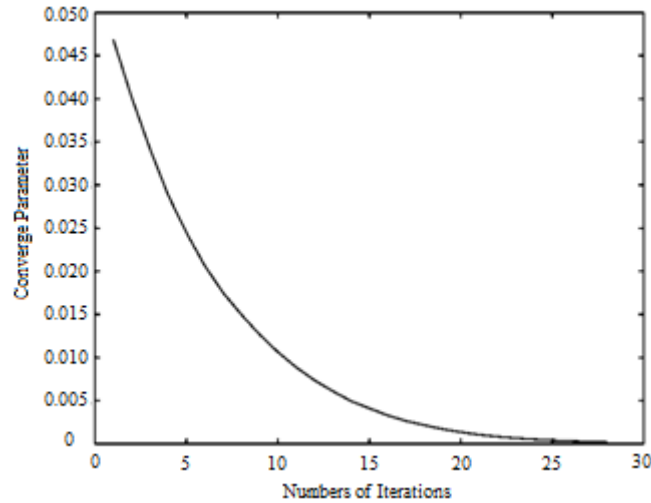


Figure 3.2: Normalised potential updates after each iteration.

3.4 Simulation Results

The graphene nanoribbon used in the study has dimensions $20\text{nm} \times 4\text{nm}$. Carbon nanotubes are formed by rolling the nanoribbon resulting in tubes of radius 0.64nm . For both structures the work-functions of the source and drain regions were taken to be 4.5eV and the conduction band edge in the channel in equilibrium is 0.15eV above the Fermi energy level. The work function is chosen to be consistent with the value for silver (Ag) used in the experimental work reported in ref [11]. Only the first subband was considered as the energies of the upper subbands exceed the drain voltage in the structures used in this simulation. A single effective mass was used in the model devices to allow comparison of their output characteristics. The effective mass was $0.0311m_0$ for both electrons and holes, where, m_0 is the free electron mass [12].

Fig. 3.3a shows a three-dimensional (3D) plot of the electron potential energy within the graphene sheet with $V_{ds} = 0\text{V}$ and $V_{gs} = 0.5\text{V}$. The electron potential energy, represented by the conduction band edge, is lower at the edges of the sheet due to the wrap around gate.

Increasing V_{ds} lowers the conduction band edge in the central region as shown in Fig. 3.3b. Cross-sections of the electron energy profiles along the edge of the sheet and in the centre of the channel, giving a clearer picture of the effect of drain voltage on electron energy, are shown in Figs. 3.3c and 3.3d respectively.

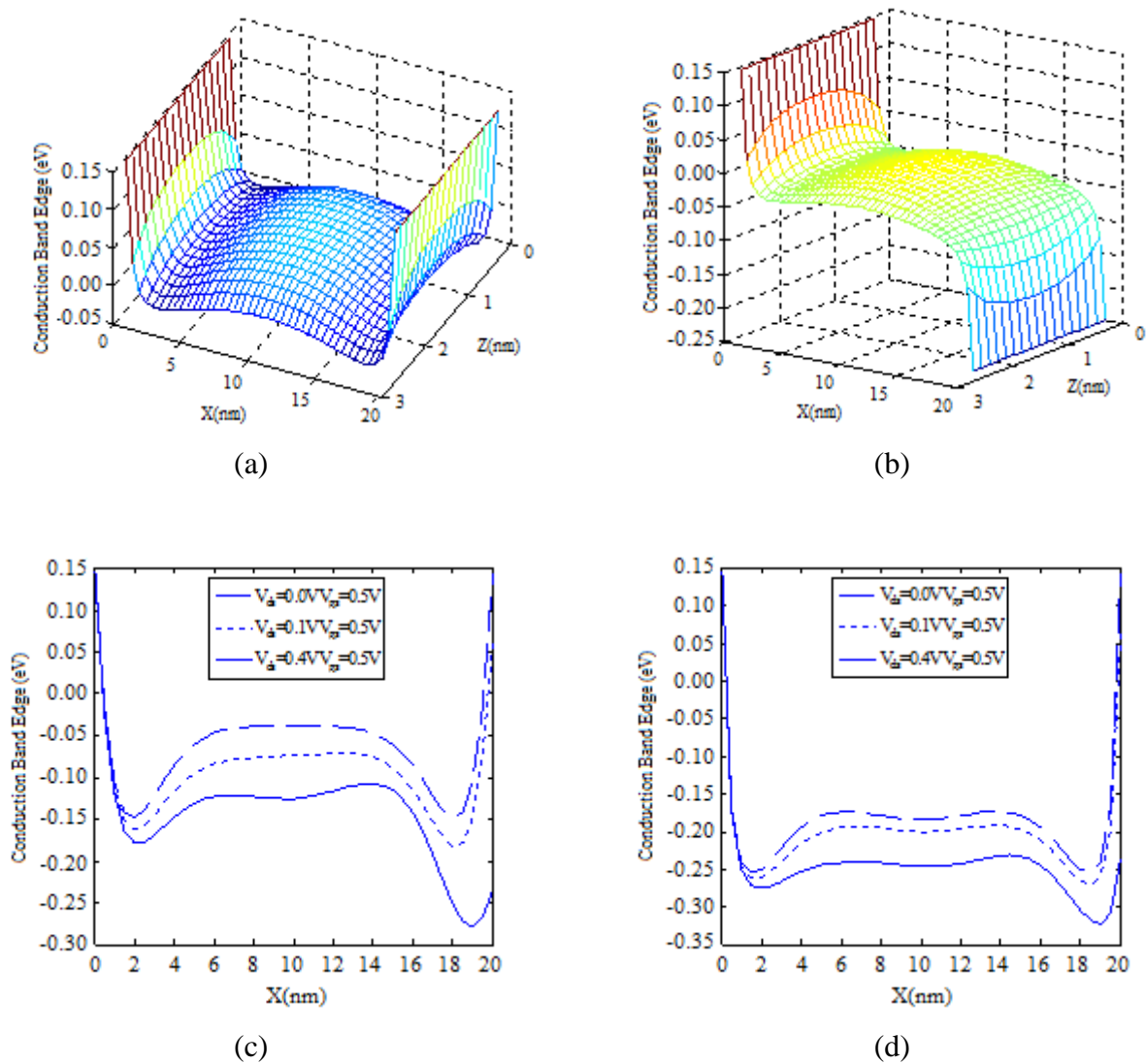


Figure 3.3: Simulation of the potential energy seen by the electrons at $V_{gs} = 0.5V$ (a) 3D view of the conduction band edge at $V_{ds} = 0.0V$ (b) 3D view of the conduction band edge at $V_{ds} = 0.4V$ (c) Conduction band edge along the length of the device for different V_{ds} at the edge of the graphene sheet (d) Conduction band edge along the length of the device for different V_{ds} at the centre of the graphene sheet.

Figures 3.4a and 3.4b show the electron density throughout the graphene sheet resulting from tunneling through the potential barrier at the contact. When the $V_{ds} = 0V$, the electron density is higher at the edges than in the centre, a result consistent with the variation of the conduction band edge. As the drain voltage is increased to $0.4V$, the electron density falls within the centre and at the edges. Again, this can be seen more clearly from the cross-sections of the energy density profile through the centre of the device and at the edges. This result can be compared with that obtained in chapter 2 for a carbon nanotube structure.

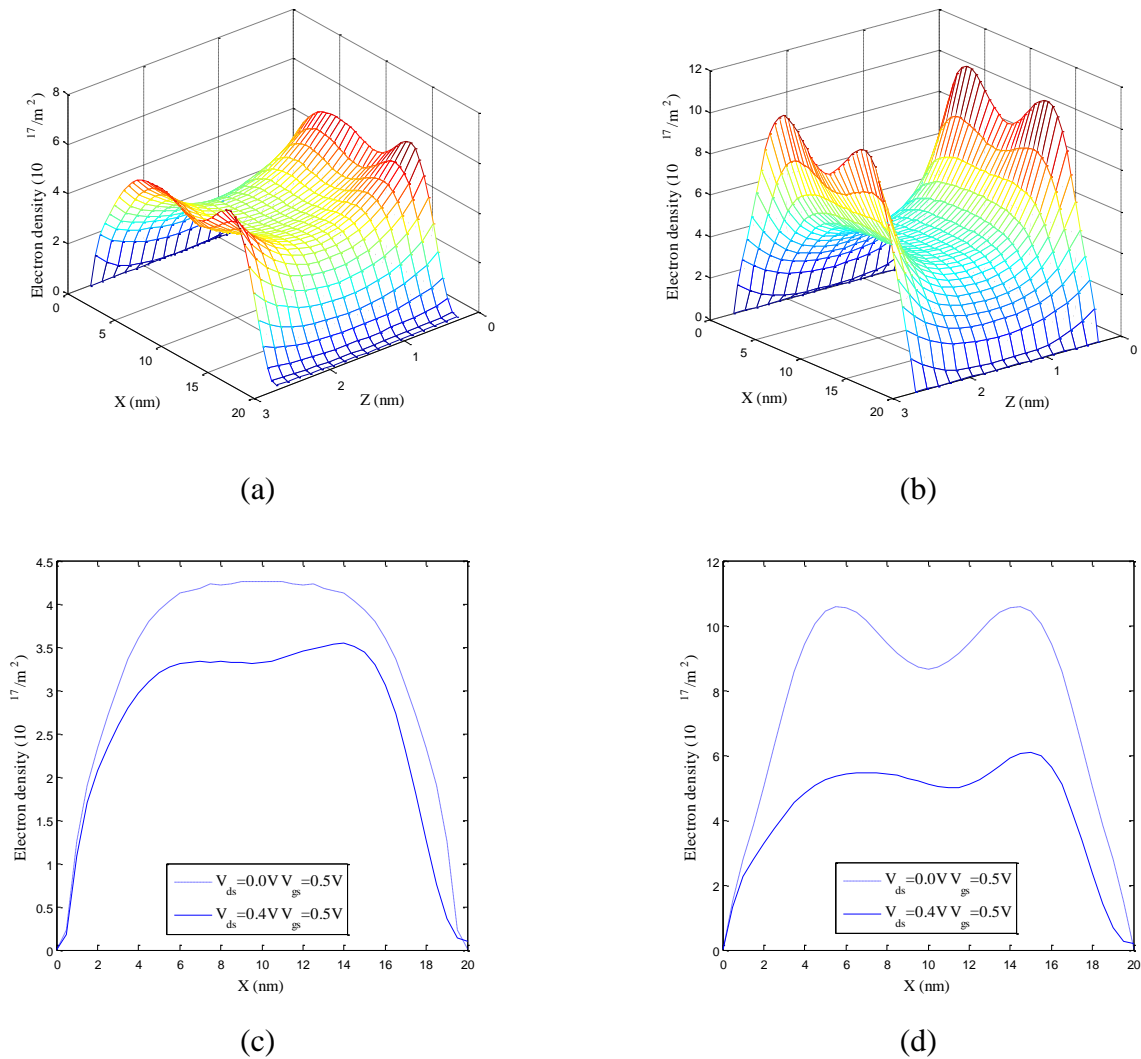


Figure 3.4: Simulation of the carrier density at $V_{gs} = 0.5V$. (a) 3D view of the net carrier density as a function of position at $V_{ds} = 0.0V$. (b) 3D view of the net carrier density as a function of position at $V_{ds} = 0.4V$. (c) Cross-section of carrier density for different V_{ds} at the centre of graphene sheet (d) Cross-section of carrier density for different V_{ds} at the edge of the graphene sheet.

Figures 3.5 (a) & (b), respectively, show the output characteristics of MOSFETs for a graphene ribbon and a carbon nanotube. The width of the graphene ribbon equals the circumference of CNT. Comparing the I-V characteristics of these devices it is observed that for graphene the maximum current drive is achieved at a much lower drain bias. This result suggests that circuits based on graphene MOSFETs may have a superior switching performance than those based on CNTs. The saturation currents for the graphene and CNT devices are $1.7\mu A$ and $3.3\mu A$, respectively. The low bias conductance of the devices can be approximated from the slope of the I-V characteristics. Based on this approximation, the maximum conductance for the graphene and CNT devices are $8.5\mu S$ and $17\mu S$, respectively.

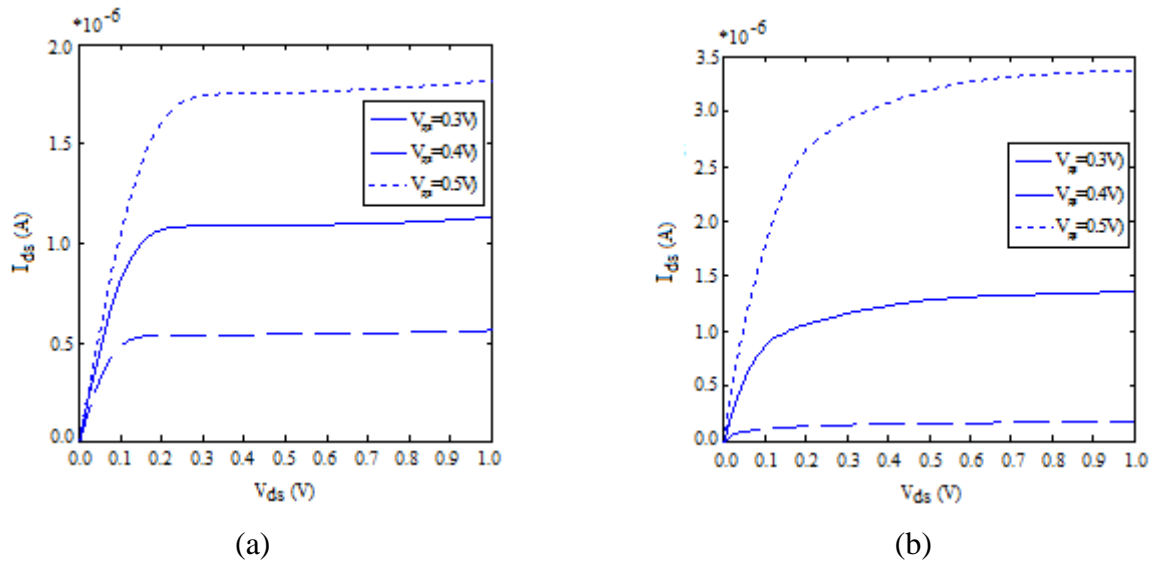


Figure 3.5: I-V characteristics of Graphene (a) and CNT (b)

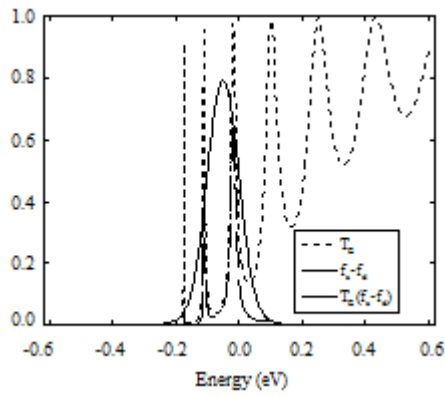
The physical origin of the difference in the output characteristics can be understood by considering the relationship between the drain current, I_{DS} , and the transmission probability, T_E and Fermi Dirac function $f(E)$:

$$I_{DS} = \frac{2e}{h} \int T_E (f_s - f_d) dE \quad (3.18)$$

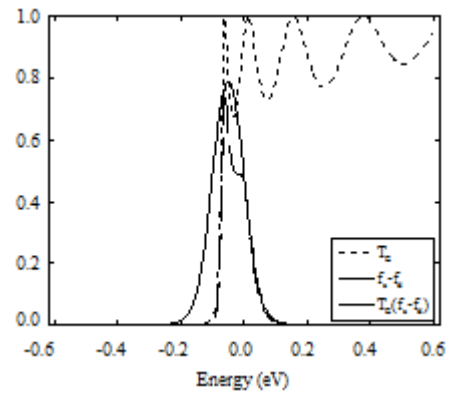
Figures 3.6 (a) – (f) show plots of T_E , $f_s - f_d$ and $T_E(f_s - f_d)$ for the graphene and CNT based MOSFETs at three drain-source voltages, $V_{ds} = 0.1, 0.24$ and $0.4V$. Figures 2.25 (a),

(c) & (e) are the results for the graphene-based device while figures 2.25 (b), (d), & (f) are the corresponding results for the CNT-based device. The drain current is represented by the area under the graph of $T_E(f_s - f_d)$ versus energy. The physical difference in the output characteristics of the two devices stems from differences in transmission probabilities. For the graphene based device the transmission probability rises rapidly but oscillates between 80% and 100%. However, in the CNT based device, transmission probability rises slowly with energy and exhibits oscillations between 5% and 90% where $f_s - f_d$ is significant.

$$V_{ds} = 0.1V$$

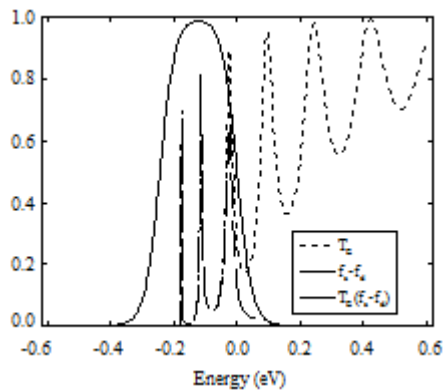


(a)

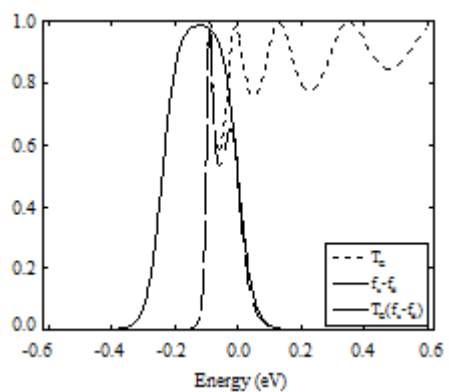


(b)

$$V_{ds} = 0.24V$$



(c)



(d)

$$V_{ds} = 0.4V$$

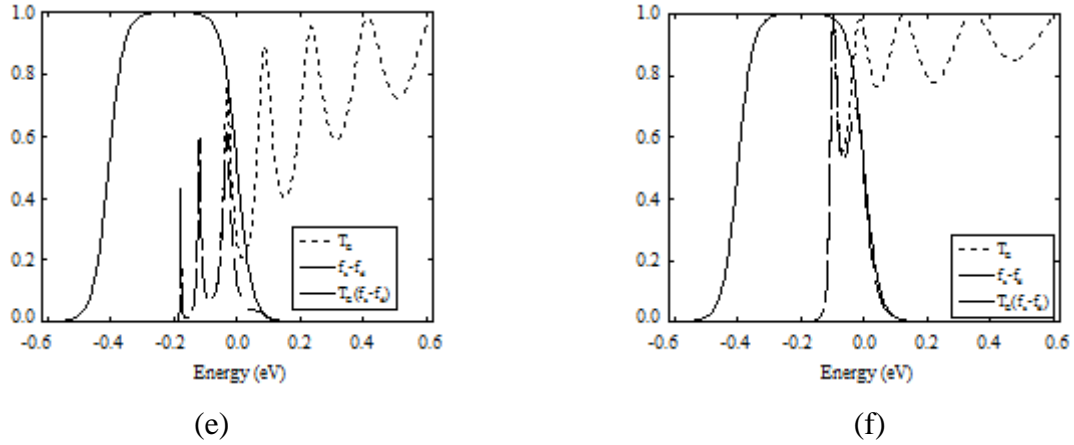


Figure 3.6: Transmission Probability and Fermi Dirac Distribution for different V_{ds} . Carbon nanotubes – (a), (c), (e) and graphene – (b), (d), (f)

As shown in Fig. 3.6, the current increases until the maximum value of $(f_s - f_d)$ is unity. Beyond that point, the current is mainly determined by T_E while the change in $(f_s - f_d)$ has no effect on the net current. The T_E plot shows that above the conduction band edge all the energy states in graphene make a contribution to the current where the transmission probabilities are well above zero. For a CNT, the transmission probabilities for electrons at some states are close to zero thereby making little contribution to the current and increasing the magnitude of V_{ds} required to obtain maximum current.

3.5 Conclusions

In this work charge transport in MOS systems based on graphene nanoribbon and carbon nanotubes has been modeled and compared. Poisson's equation is discretized in three-dimensions and solved self-consistently with Schrödinger's equation. The latter is solved using the scattering matrix method enabling resonance effects to be taken into account. The band structure of graphene is obtained through a tight-binding Hamiltonian of the armchair-edge nanoribbon. To improve immunity to short channel effects, a fully wrapped gate is assumed for both devices [13].

In the graphene-based FET edge effects influence the energy band structure and charge density. Differences are observed in the output characteristics of the two devices that stem from differences in transmission probabilities. For CNFET's the transmission probability is the same at all points on the circumference of the nanotube. However, the structure chosen for the graphene FET results in potential differences between the edges and the centre of the graphene sheet leading to differences in the amplitudes of the electron wavefunction. The total transmission probability for the graphene FET is, therefore, a summation of transmission probabilities over the width of the graphene nanoribbon. As each element of the summation has the characteristic form exhibited by the CNT structure the total transmission probability for the nanoribbon displays smaller oscillations and a more rapid rise in average value with increasing energy.

The output characteristics of the CNFET and GFET devices are largely dependent on the contacts used to terminate the device ends. In the next chapter, electron transport in CNTs is studied using non-contacting means. The contactless studies were carried out on CNTs as samples are readily available.

3.6 References

- [1] J. Guo, S. Datta, M. P. Anantram and M. Lundstrom, Atomistic Simulation of Carbon Nanotube Field-Effect Transistors Using Non-Equilibrium Green's Function Formalism, *Journal of Computational Electronics*, Volume 3, Numbers 3-4, 373-377, 2005.
- [2] D. L. John, L. C. Castro, P. J. S. Pereira, and D. L. Pulfrey, A Schrodinger-Poisson Solver for Modeling Carbon Nanotube FETs, *Proc. NSTI Nanotech*, vol. 3, pp. 65-68, 2004.
- [3] M. Pourfath, H. Kosina, and S. Selberherr, A fast and stable Poisson-Schrodinger solver for the analysis of carbon nanotube transistors, *Journal of Computational Electronics*, vol. 5, pp. 155-159, 2006.
- [4] R. Saito, G. Dresselhaus, and M. S. Dresselhaus, *Physical Properties of Carbon Nanotubes*. London: Imperial College Press, 1998.
- [5] K. S. Novoselov, A. K. Geim, S. V. Morozov, D. Jiang, Y. Zhang, S. V. Dubonos, I. V. Grigorieva, and A. A. Firsov, Electric Field Effect in Atomically Thin Carbon Films. vol. 306: American Association for the Advancement of Science, 2004, pp. 666-669.
- [6] J. Fernandez-Rossier, J. J. Palacios, and L. Brey, Electronic structure of gated graphene and graphene ribbons, *Physical Review B*, vol. 75, pp. 205441, 2007.
- [7] G. Gu, S. Nie, R. M. Feenstra, R. P. Devaty, W. J. Choyke, W. K. Chan, and M. G. Kane, Field effect in epitaxial graphene on a silicon carbide substrate, *Applied Physics Letters*, vol. 90, pp. 253507-3, 2007.
- [8] D. Gunlycke and C. T. White, Tight-binding energy dispersions of armchair-edge graphene nanostrips, *Physical Review B*, vol. 77, pp. 115-116, 2008.
- [9] J. Charlier, P. C. Eklund, J. Zhu, and A. C. Ferrari, Electron and Phonon Properties of Graphene: Their Relationship with Carbon Nanotubes, *TOPICS IN APPLIED PHYSICS*, vol. 111, pp. 673, 2008.

- [10] D. K. Ferry and S. M. Goodnick, *Transport in Nanostructures*, Cambridge University Press, 1997.
- [11] G. C. Liang, N. Neophytou, D. E. Nikonov, and M. S. Lundstrom, Performance projections for ballistic graphene nanoribbon field-effect transistors, *IEEE Transactions on Electron Devices*, vol. 54, pp. 677-682, Apr 2007.
- [12] C. Schonberger, *Bandstructure of Graphene and Carbon Nanotubes: An Exercise in Condensed Matter Physics*, April 2000.
- [13] Y. Ouyang, Y. Yoon, and J. Guo, Scaling Behaviors of Graphene Nanoribbon FETs: A Three-Dimensional Quantum Simulation Study, *Electron Devices, IEEE Transactions on*, vol. 54, pp. 2223-2231, 2007.

Chapter 4

Experiment – Contactless Measurements of Electron Transport in Carbon Nanotubes

4.1 Introduction - Metallic Contact Limitations

There has been intensive research on carbon nanotubes (CNTs) to examine their electron transport properties and their possible use as future nanoscale devices. So far, experimental results have shown that these new carbon structures have the potential to be the building blocks of electronic systems for various applications [1][2].

The electronic properties of CNTs have mostly been observed by connecting electrodes to the nanotube ends but quantised conductance appears on making contacts [3]. There is a fundamental ballistic conductance which sets a saturation of the device current with a quantum resistance. As shown in Fig. 4.1, there is a broadening of the energy level that accompanies the coupling of the nanotube to the electrodes. As a result, part of the energy level spreads outside the energy range between electrochemical potentials μ_1 and μ_2 where current flows, consequently reducing the expected current. The ballistic conductance G of the device is expressed as:

$$G = \frac{I}{V_{ds}} = \frac{q^2}{2C\hbar} \quad (4.1)$$

where I is the device current, V_{ds} is the drain voltage, q is the electron charge, \hbar is the reduced Planck's constant, and C is the coupling strength. In chapter 2, it was observed that

the on-current of a CNFET device depends on the tunnelling barrier, the height of which is determined by the end contacts.

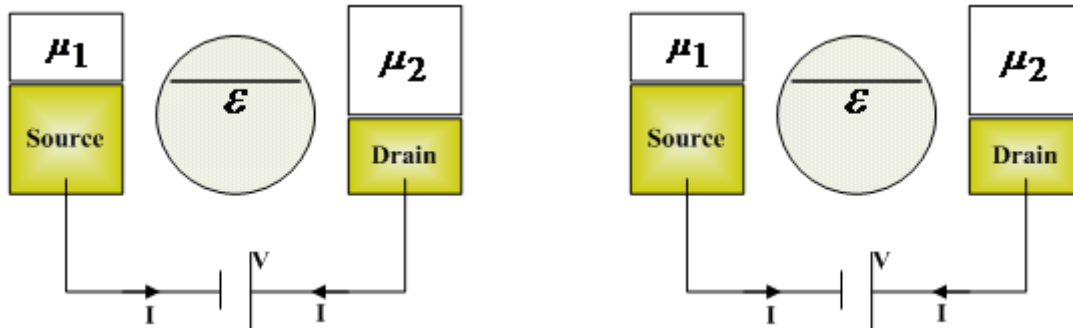


Figure 4.1: (a) A small drain bias applied across the channel causing a splitting of the electrochemical potentials. (b) Energy level broadening due to the process of coupling to the channel.

Experimentally, it is difficult to control the contact effects of the electrodes, which is one of the issues in the development of CNT devices. So, there is still a need to determine the fundamental properties of CNTs, accurately.

In this chapter, electron transport in CNTs is studied using non-contacting means, by inducing current in individual nanotubes using microwave energy. A sample of nanotubes is inserted into the high field region of a hairpin resonator cavity, and this drives current along the nanotubes. The electronic properties of the CNTs are then examined using cavity perturbation theory [4]. In this study, the very nature of current in the sample is specified by imposing Ohm's law to be satisfied within the lossy sample.

In the next section, the experimental techniques used to observe the morphology and microstructure of the CNTs are introduced.

4.2 Experimental Techniques

Detailed information of the nanotube sample topography is obtained using scanning electron microscopy (SEM), high-resolution transmission electron microscopy (HRTEM) and energy dispersive X-ray spectroscopy (EDX). The microstructure of the CNTs is examined using HRTEM, and the morphology of the sample is examined using SEM. EDX is used on selected areas of the CNT for composition analysis.

4.2.1 Scanning Electron Microscopy/Transmission Electron Microscopy [5]

A scanning electron microscope images the surface of samples using a high-energy beam of electrons [5]. Electrons from a field-emission cathode are accelerated through a voltage difference between the cathode and anode, in the range of 0.1keV and 50keV . The smallest beam cross-section at the gun is demagnified by a two- or three-stage electron lens system so that an electron probe is formed at the surface of the specimen. Detectors inside the chamber record the emitted electron spectrum. The emitted electrons interact with the atoms in the molecule producing signals that contain information about the sample. A deflection coil system raster scans the electron probe across the specimen in synchronisation with the electron beam of a separate cathode-ray tube (CRT). One of the signals recorded modulates the intensity of the CRT to form an image.

Transmission electron microscopy (TEM) is one of the main tools used for observing the microstructural characterization of materials [6]. A variation in the intensity of electron diffraction across a thin specimen, known as diffraction contrast, is used for making images of defects. In HRTEM, the phase of the diffracted electron wave is preserved and allowed to

interfere with the phase of the transmitted wave. The phase contrast imaging technique is used to form images of columns of atoms. The high-energy electrons in the microscope cause electronic excitations of the atoms in the specimen and chemical information can be obtained from the electron excitations.

4.2.2 Energy Dispersive X-ray Spectroscopy [7]

Energy dispersive X-ray spectroscopy is an analytical technique used predominantly for the elemental analysis of a specimen [7]. X-rays of a variety of energies are generated by the specimen and strike a silicon crystal. When the X-ray strikes the silicon crystal, it releases its energy in series of collision events and each event gives rise to one electron and one hole.

Since there is a voltage bias of $1kV$ between the gold layers at the surface of the silicon crystal, the electrons and holes are attracted to the opposite sides of the crystal, causing a pulse of current to occur. The energy of the X-ray entering the crystal is proportional to the number of electron-hole pairs generated. Therefore, the current pulse is also proportional to the X-ray energy. The generated current pulse is converted to a voltage pulse, and the height of the voltage pulse is proportional to the energy of the incident X-ray. The pulse height analyser measures the height of the voltage pulse and stores the result.

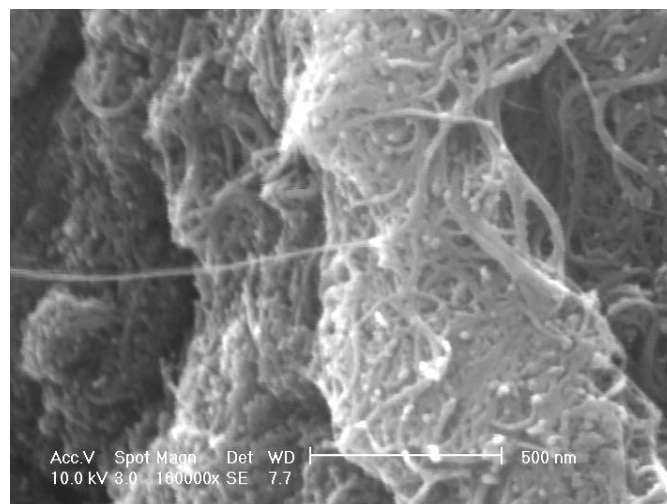
The information of the pulse stored after a period is a spectrum, which has as its ordinate the X-ray energy and its abscissa the number of pulses proportional to the number of X-rays that entered the silicon crystal of this energy.

In the next section, the morphology and the microstructure of the CNTs sample used for this experiment are examined. Powdered nanotubes were obtained from Thomas Swan Ltd. The nanotubes were grown at $800^{\circ}C$ by thermal chemical vapour decomposition (CVD) on Ni/Si substrates, giving a mixture of semiconducting and metallic SWNTs.

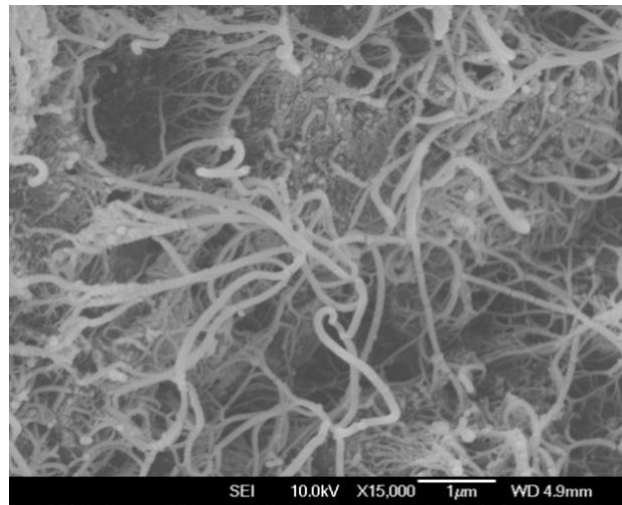
4.3 Microstructure and Morphology of the CNTs

Using a mortar and pestle, the clumped nanotubes are manually ground, turning them into fine particles. The surface topography and microstructure were analysed using SEM and TEM, respectively. A Cu/Rh grid covered with formvar was used for the TEM grid [8]. About 0.5mg of nanotube powder is dispersed in 2ml of toluene solvent, followed by an hour sonication in order to achieve full dispersion, and a drop was deposited on the grid. In addition, Energy Dispersive X-ray Spectroscopy is used to examine the composition of the nanotubes sample.

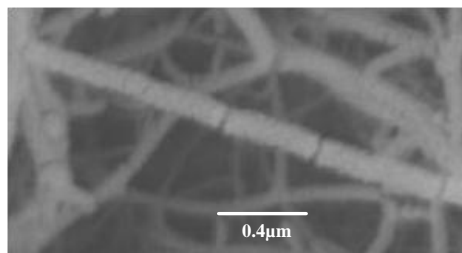
Figure 4.2 shows the SEM image of the nanotubes before and after manual grinding. The long nanotubes are broken into smaller segments and it is possible to obtain a finer sample. This confirms the production of short carbon nanotubes, which has been previously reported using the ball milling technique [8].



(a)



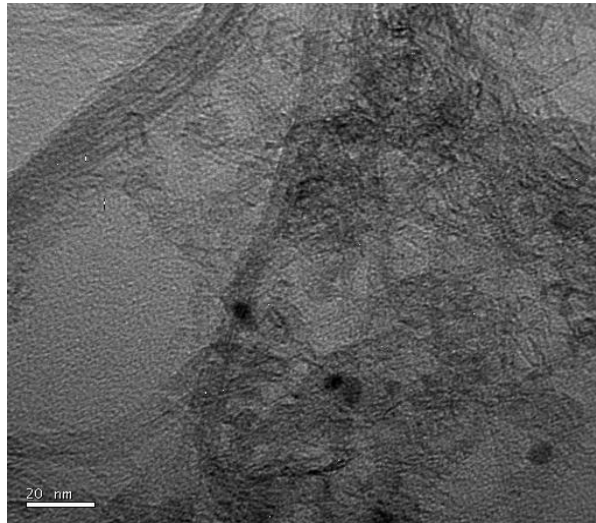
(b)



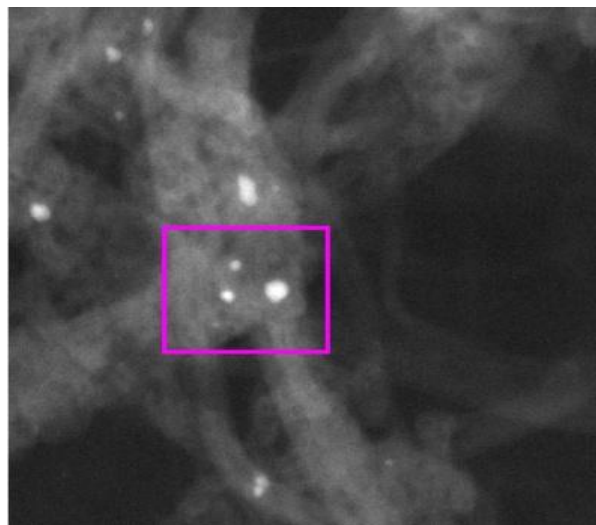
(c)

Figure 4.2: SEM image of the CNTs used for this experiment (a) before and (b,c) after manual grinding.

Structural characteristics of the nanotubes were observed by TEM. From TEM observations, the nanotube length can be measured and the distribution of the nanotubes within the bulk sample can be examined. Fig. 4.3 shows the TEM images of the nanotubes with diameters ranging from 1.2nm to 1.7nm and the length ranging from 100nm to $4\mu\text{m}$. Scanning transmission microscopy (STEM) of the nanotubes shows that there are iron (Fe) impurities on the surface of the nanotubes. These magnetic impurities are from the substrate used to stimulate the growth of the nanotubes during production [8]. More TEM images of the nanotubes are shown in Appendix 7.



(a)



(b)

Figure 4.3: (a) The TEM image of the nanotube sample, the dark spots representing the impurities and (b) an evidence of the Fe content (inset) in the STEM image of the sample.

The EDX analysis also confirmed the presence of iron (Fe) impurities in the chemical composition of the nanotubes sample. The volume of contamination is less than 3% of the entire sample. As shown in Table 4.1, EDX gives atomic % ratios of 96.5:2.7:0.8 for C:O:Fe. Since the small amount of Fe in the nanotube sample is well dispersed, it is not expected to influence the microwave measurements.

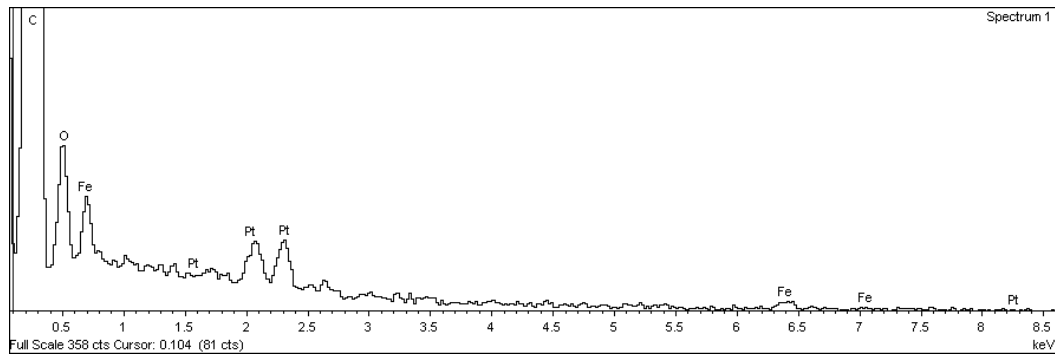


Figure 4.4: EDX result showing the composition of the CNTs.

Element	Weight %	Atomic %
Carbon, C	92.99	96.48
Oxygen, O	3.52	2.74
Iron, Fe	3.49	0.78
Totals	100.00	100.00

Table 4.1: Elemental analysis of the nanotubes sample using EDX.

In the next section, the hairpin resonator used to study the electronic properties of the CNTs is described.

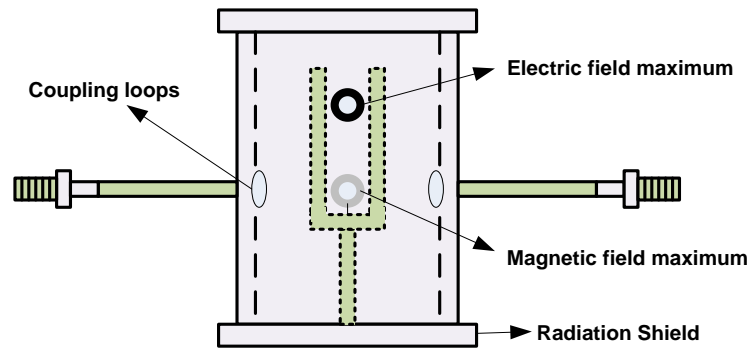
4.4. Copper Hairpin Resonator

A hairpin resonator is equivalent to a quarter wavelength long resonant transverse electromagnetic transmission line (TL) [9]. A schematic representation of a hairpin resonator is shown in Fig. 4.5. Microwaves are coupled into the resonator cavity through a pair of loop-coupled coaxial cables, which induce a standing quarter wave resonance along the hairpin resonator. A segment of the TL resonates when its length equals odd integer multiples of a quarter wavelength. The fundamental resonant mode occurs at $l = \lambda/4$ and its corresponding resonant frequency is:

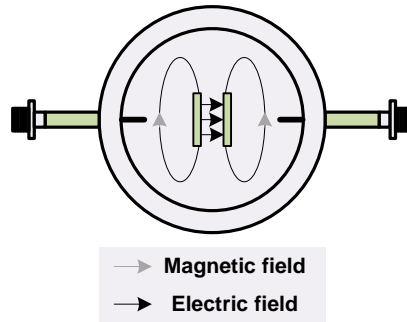
$$f_0 = \frac{c}{4l} \quad (4.2)$$

where l represents the length of the hairpin and c is the speed of light. As shown in Fig. 4.5a, the electromagnetic fields mainly occupy the volume of the parallel plates. There are two insertion points in the radiation shield of the resonator, top and bottom and correspond to the electric field maximum and magnetic field maximum, respectively. Samples can be placed in either the magnetic field or the electric field region depending on the required measurement.

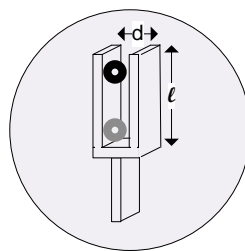
A vector network analyser (VNA) is used to measure the magnitude of the voltage transmission coefficient (S_{21}) of the hairpin resonator as a function of frequency. VNAs are usually employed for measuring the quality factor (Q) and the resonant frequency (f_0).



(a)



(b)



(c)

Figure 4.5: A schematic of the hairpin resonator used for the microwave measurements [9].
 (a) Side view (b) Top view and (c) Inner structure.

The quality factor of the resonator is the ratio of the resonant frequency f_0 to the frequency of the bandwidth at half-maximum power f_B . It gives an indication of the overall sensitivity of the resonator and it should be large enough to show the maximum change in the bandwidth when a sample is inserted. When the quality factor is high for a small volume of the parallel plates in the resonator, there is high filling factor when the sample is inserted into the cavity, leading to a very sensitive measurement. The ideal spectral response of a resonator operating in the transmission mode is shown in Fig. 4.6.

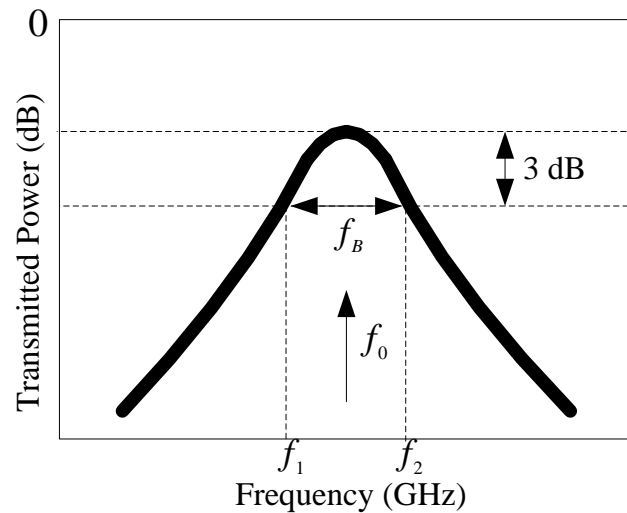


Figure 4.6: The spectral response of a resonator in transmission mode observed using the Agilent E5071B Network Analyser.

The cavity perturbation technique is based on first-order perturbation theory [10], and it is frequently employed when resonators are modified by the introduction of small samples into their cavities. The main assumption in the perturbation technique is that $\Delta f_0 \propto \varepsilon_1$ and $\Delta(1/Q) \propto \varepsilon_2$, where ε_1 is the permittivity, ε_2 is the loss factor, Δf_0 and $\Delta(1/Q)$ are changes in f_0 and $1/Q$ due to sample insertion, respectively [11].

4.5 Experimental Analysis using Cavity Perturbation Technique

In this experiment, a sample of CNTs is inserted in the high magnetic field region of the hairpin resonator cavity. The electrical properties of the CNTs were then examined using cavity perturbation technique. Fig. 4.7 shows the hairpin resonator used for this experiment. The hairpin resonator is treated as a transmission-line antenna that is shorted at one end while opened at the other end, forming a two-plated hairpin structure [12]. The fundamental resonant frequency of the hairpin resonator is determined by Eq. 4.2. At resonance, the electric field is at its maximum at the open circuit end and zero at the short circuit end. On the other hand, the magnetic field is largest at the short circuit end and zero at the open circuit end.

The hairpin resonator used in this experiment was constructed from a 1mm thick copper sheet with a length of 23mm . According to Eq. 4.2, these dimensions yield a resonant frequency of 3GHz . The hairpin structure was enclosed in a copper radiation shield having a diameter of 20mm . The radiation shield ensured that a high Q was obtained by avoiding the loss of the stored energy through emission of the electromagnetic radiation.

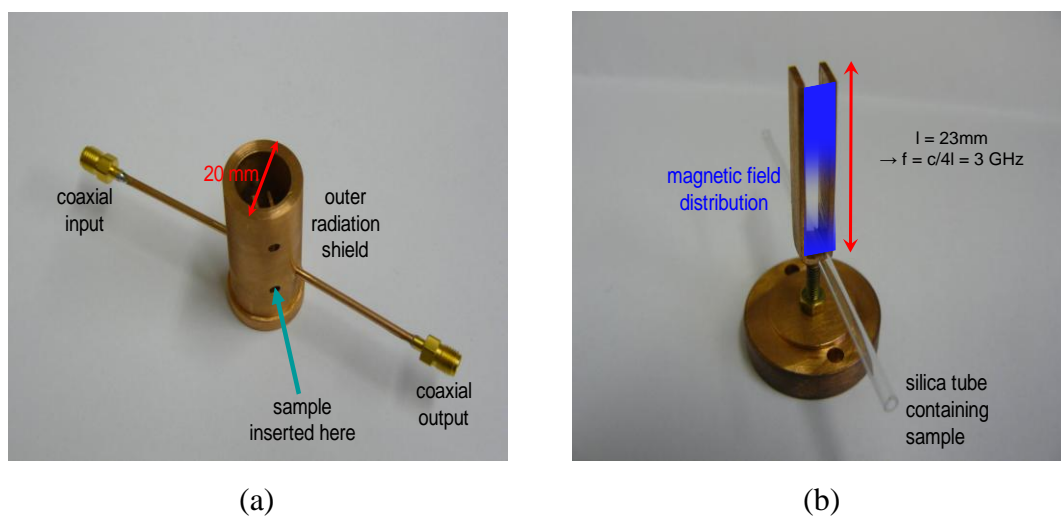


Figure 4.7: (a) 3GHz copper hairpin resonator & (b) Inner structure of the resonator.

The sample is inserted in the region of high magnetic field via the small hole created on the outer shield of the resonator. The magnetic field is generated from the microwave energy applied through the coaxial input shown in Fig. 4.7a. The microwave energy undergoes a change, as it passes through the inner structure of the resonator, dependent on the loaded sample. The output energy of the hairpin resonator is then measured at the coaxial output. The input and output energies differ if the sample absorbs some of the applied microwave energy and the electrical properties of the sample from the recorded energy loss can be examined.

As shown in Fig. 4.8, when the sample is inserted in the region of uniform magnetic field, a screening current can be induced. If this screening current is large enough, there will be a large inverse internal magnetic field that attempts to cancel the changing applied magnetic field, according to Lenz's law. During this process, the sample acquires a magnetic dipole moment m and the internal magnetic field H_1 is reduced compared to the external applied magnetic field H_0 .

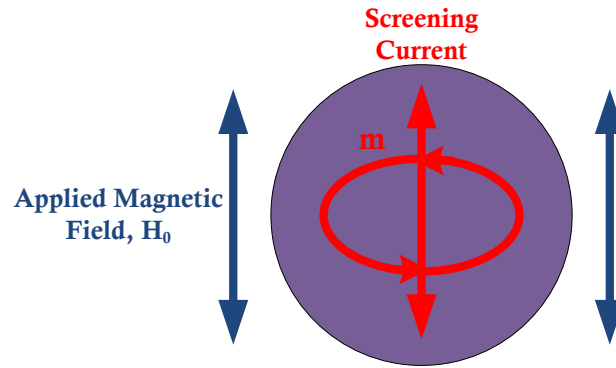


Figure 4.8: Screening current in the CNTs sample due to applied magnetic field.

The resulting perturbations on a host resonator used to apply the field are [11]:

$$\frac{\Delta f_0}{f_0} = \frac{\mu_0}{4U} \text{Re}(mH_0) \quad (4.3)$$

$$\frac{\Delta f_B}{f_0} = \frac{\mu_0}{2U} \text{Im}(mH_0) \quad (4.4)$$

where μ_0 is the magnetic constant, U is stored energy, Δf_0 is the increased resonant frequency, Δf_B is the increased bandwidth. The total energy stored U is the sum of electric and magnetic energies, which are equal at resonance [13]:

$$U = 2U_m = \frac{1}{2} \int_V \mu_0 H_0^2 dV \quad (4.5)$$

where V is the cavity volume and U_m is the stored magnetic energy. As shown in Eq. 4.3 and Eq. 4.4, the real and imaginary parts of the applied magnetic field are related to the stored energy and therefore, the electrical properties of the loaded sample can be examined from the stored energy.

Now, an expression that relates the applied magnetic field H_0 to the internal magnetic field H_1 is derived. The magnetic moment and the internal magnetic field depend on the geometry of the CNTs. Since this varies for different measurements, the analysis is semi-quantitative.

The screening current is calculated from the generated internal magnetic field. Fig. 4.9 shows the possible screening current directions in the nanotubes. In the analysis, the individual nanotube is treated as a conductor and quantisation is ignored, allowing electrons to move freely along the length of the nanotube.

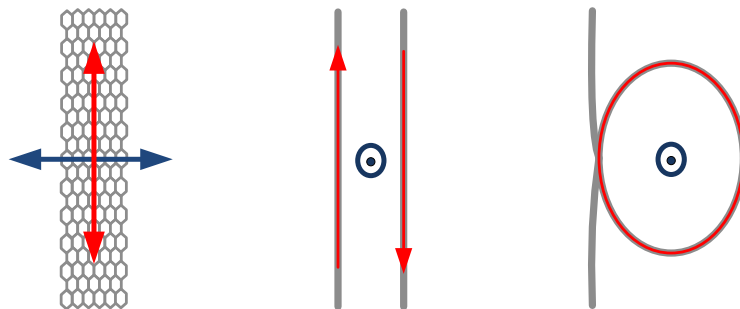


Figure 4.9: Possible screening current patterns for various orientations of the CNTs in the bulk sample.

The relationship between the internal magnetic field H_1 and the applied magnetic field H_0 is derived for all possible screening current directions in the sample. Fig. 4.10 shows one of the possible geometries of the nanotubes in the bulk sample. The magnetic moment m of the system measures the strength and the direction of its magnetisation. The relationship between the magnetic moment and the screening current is given by:

$$m = IA \quad (4.6)$$

where I is the screening current and A is the area enclosed by the loop. The magnetisation M is the quantity of magnetic moment per unit volume V_s . In the system, m is related to V_s by:

$$m = V_s M = V_s (H_0 - H_1) \quad (4.7)$$

Solving for the internal magnetic field H_1 , equating Eq. 4.6 to Eq. 4.7 yields:

$$(H_0 - H_1)A \cdot \partial z = IA \quad (4.8)$$

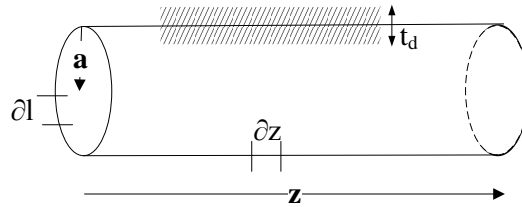


Figure 4.10: One of the possible geometries of the nanotubes in the bulk sample.

According to Faraday's law of electromagnetic induction, the induced electric field is related to the magnetic field by:

$$\nabla \times E = -\mu \frac{\partial H}{\partial t} \quad (4.9)$$

$$\oint E \cdot \partial l = -\frac{\partial}{\partial t} \oint B \cdot \partial s \quad (4.10)$$

$$E \cdot 2\pi a = -\mu_0 \pi a^2 \frac{\partial H_1}{\partial t} \quad (4.11)$$

$$E = -\frac{\mu_0 a}{2} \frac{\partial H_1}{\partial t} \quad (4.12)$$

where a is the radius of the nanotube. The current density J is proportional to the electric field E , as expressed by Ohm's law:

$$J = \sigma E \quad (4.13)$$

$$I = J t_d \cdot \partial z \quad (4.14)$$

where t_d is the thickness of the graphene wall of the nanotube, which is around 0.1nm . Solving Eq. 4.8 and Eq. 4.13 together yields:

$$(H_0 - H_1) = \sigma E \cdot t_d \quad (4.15)$$

$$(H_0 - H_1) = \frac{E}{R_{sq}} \quad (4.16)$$

where the electrical conductivity σ , is related to the sheet resistance R_{sq} by:

$$\sigma t_d = \frac{1}{R_{sq}} \quad (4.17)$$

Substituting Eq. 4.12 into Eq. 4.16, we have

$$(H_0 - H_1) = -\frac{\mu_0 a}{2R_{sq}} \frac{\partial H_1}{\partial t} \quad (4.18)$$

$$(H_0 - H_1) = -\tau \frac{\partial H_1}{\partial t} \quad (4.19)$$

$$\frac{\partial H_1}{\partial t} \rightarrow j\omega H_1 \quad (4.20)$$

In all three cases described in Fig. 4.9, the internal magnetic field is related to the applied magnetic field through Eq. 4.21.

$$H_1 = \frac{H_0}{1+j\omega\tau} \quad (4.21)$$

From Eq. 4.18, the relaxation time τ , is defined as:

$$\tau \approx \frac{\mu_0 a}{R_{sq}} \quad (4.22)$$

Based on Eq. 4.21, effective screening only occurs in the limit when $\omega\tau > 1$. This leads to the limits on the sheet resistance, which is $R_{sq} < \mu_0 a\omega$, as obtained from Eq. 4.22. For the magnetic field applied to the CNTs sample, the main results are [11]:

$$\frac{\Delta f_0}{f_0} = - \frac{\omega^2 \tau^2}{1 + \omega^2 \tau^2} \frac{V_s}{V_{eff}} \quad (4.23)$$

$$\frac{\Delta f_B}{f_0} = \frac{\omega\tau}{1 + \omega^2 \tau^2} \frac{V_s}{V_{eff}} \quad (4.24)$$

where, V_s is the total sample volume, V_{eff} is the effective cavity volume defined via:

$$V_{eff} = \int_{cavity} (H_0/H_1)^2 dV \approx lWd/2 \quad (4.25)$$

where l , W , and d are the length, width and diameter of the hairpin, respectively.

The radius of the nanotube sample is much less than the skin depth, and the sample can be treated as a lossy dielectric with a uniform internal magnetic field H_1 responding to the applied magnetic field H_0 . Therefore, the change in the spectral response bandwidth due to the loaded nanotubes sample is proportional to the conductivity of the sample.

In the next section, the experimental results obtained using the 3GHz microwave host cavity to study the electronic properties of single-walled carbon nanotubes (SWNTs) are discussed.

4.6 Experimental Results

The CNTs were dispersed in paraffin wax using 10% by volume powder:wax composite, in a uniform manner. Samples were loaded into low-loss quartz tubes (inner diameter of 1.3mm and wall thickness of 0.35mm) and placed parallel to the magnetic field in the 3GHz quarter-wave copper hairpin cavity with magnetic coupling, shown in Fig. 4.7.

The transmitted microwave power was measured in the frequency domain using an Agilent E5071B network analyser operating in the transmission mode (S_{21}). The spectral response of the resonator was observed with and without the nanotubes sample. The recorded bandwidth when the resonator contains an empty quartz tube is subtracted from the recorded bandwidth when the resonator contains the sample plus quartz tube. The interaction between the microwave energy and the quartz tube is very small. Therefore, the tube does not affect the magnetic field in its vicinity.

Fig. 4.11 shows the spectral response of the hairpin resonator when empty. Microwave energy is transferred into the resonator cavity and the output power, which depends on the content of the resonator, is measured from the coaxial output. The spectral response plot shows the transmitted power, which is the ratio of the input and output microwave energy measured in decibels against frequency in Hertz. The bandwidth f_B , the centre frequency f_0 , and the quality factor Q are determined from the spectral response plot. The quality factor of the empty cavity is around 1200, which is large for its small volume ($\approx 600\text{mm}^3$), thus enhancing the sample filling factor for sensitive measurements.

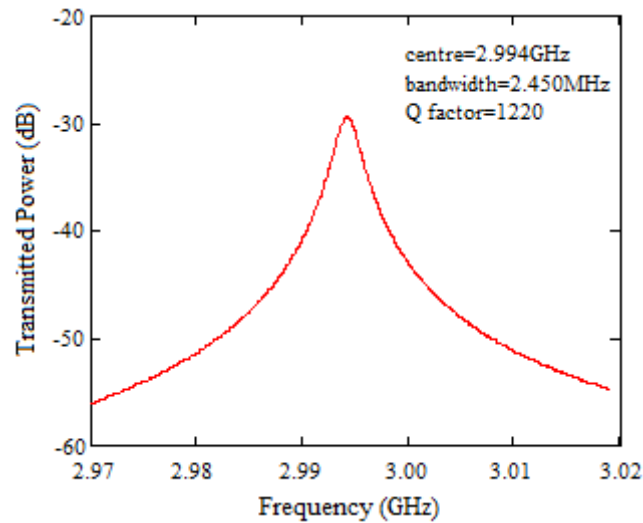
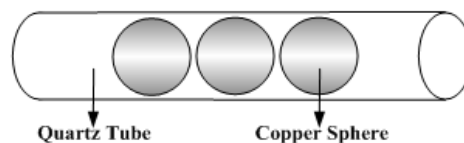


Figure 4.11: Spectral response of the empty hairpin resonator.

As part of the experimental analysis, a calibration was carried out. Small copper spheres of radii $330\mu\text{m}$ were inserted into the same magnetic field region of the resonator cavity. As shown in Fig. 4.12, a frequency shift of $\Delta f_0 = 1.3 \pm 0.01$ MHz per sphere is observed, which allows comparison of the experimental effective cavity volume of $270 \pm 2 \text{ mm}^3$ to the expected value of $lWd/2 \approx 290 \text{ mm}^3$. The length l , width W and diameter d are 23 mm , 5 mm and 5 mm , respectively



(a)

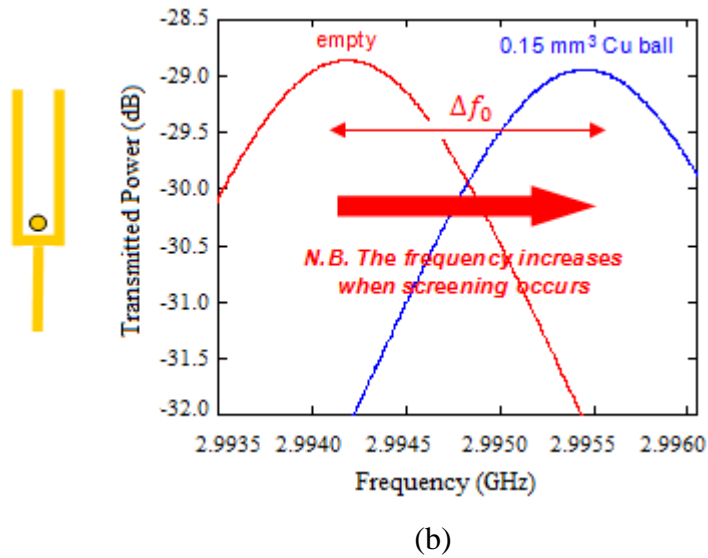


Figure 4.12: Calibration experiment: (a) Quartz tube loaded with copper spheres. (b) Spectral response of the hairpin resonator when loaded with small copper spheres.

Fig. 4.13 shows the spectral response when the nanotube sample is inserted into the cavity of the hairpin resonator. A shift in the resonant frequency (Δf_0) is observed due to the loaded sample. The response of the nanotubes to the surrounding magnetic field has an effect on the transmitted microwave energy, leading to a change in the spectral response of the resonator. An increased resonant frequency of about 9.0 ± 0.3 MHz was recorded when the sample was inserted into the cavity. An increased 3dB bandwidth of $\Delta f_B = 18 \pm 1$ MHz was also recorded, which confirms that the nanotubes sample is lossy.

There is a shift in the resonant frequency, Δf_0 because the sample screens the applied magnetic field, which shows that the sample is conductive. The magnitude of the screening current is proportional to the conductivity of the sample. The observed broadening of the spectral response bandwidth is also an effect of the sample conductivity. The overall loss in the resonator cavity decreases with increasing conductivity of the loaded sample, which consequently leads to the broadening of the bandwidth.

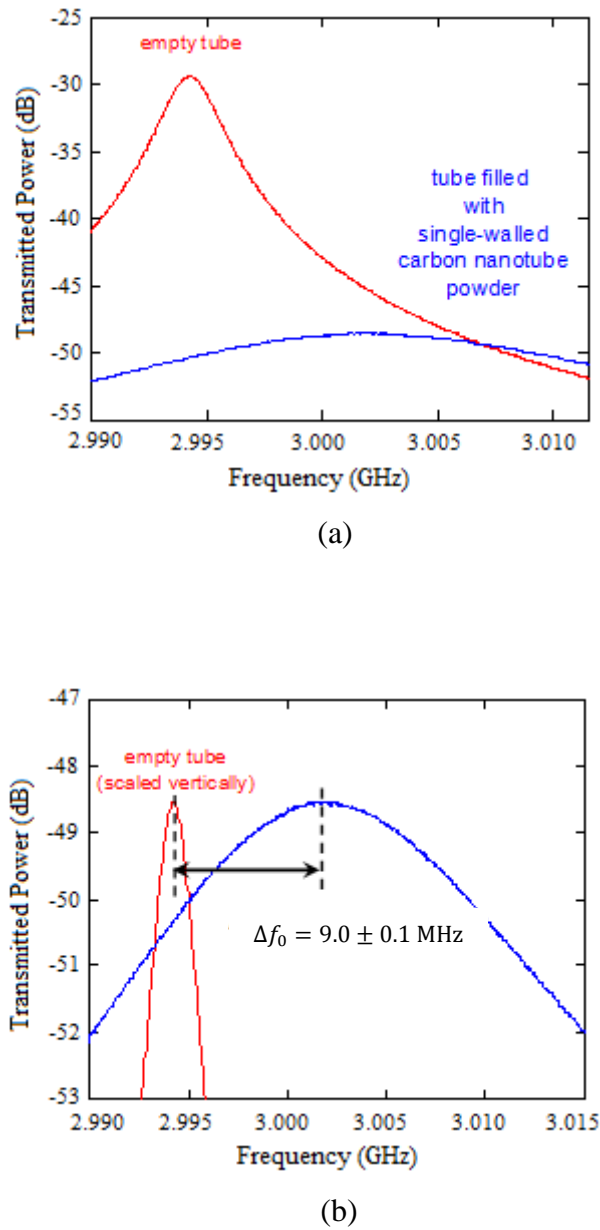


Figure 4.13: (a) Spectral response of the hairpin resonator when loaded with nanotubes sample, (b) Scaled plot of the spectral response shown in (a).

The observed resonant frequency shift is largely dependent on how the magnetic field is screened within the nanotubes. From the measurements, the screened volume is $1.7 \pm 0.02 \text{ mm}^3$ with an estimated nanotube volume of $0.40 \pm 0.05 \text{ mm}^3$ (estimated from powder mass of 1.3 mg). As shown in Fig. 4.13, the screening current is quite high for such a small sample mass, which confirms that the conductivity of the CNTs is high. As shown in Eq. 4.22, an effective screening of the magnetic energy only occurs in the limit when $\omega\tau > 1$, therefore, $R_{sq} < \omega\mu_0 a \approx 10^{-5} \Omega/\text{sq}$ based on a mean nanotube radius of 0.7 nm . Also, based on the recorded bandwidth increase, the calculated sheet resistance is $2 \times 10^{-5} \Omega/\text{sq}$. Using Eq. 4.17, the calculated conductivity σ of an individual CNT is $\sim 10^{15} \text{ S/m}$, which is extremely high.

Fig. 4.14 shows the spectral response of the hairpin resonator when loaded with graphite. A similar measurement performed on graphite shows that the conductivity of graphite is not sufficient for measurable screening, justifying the experimental procedure.

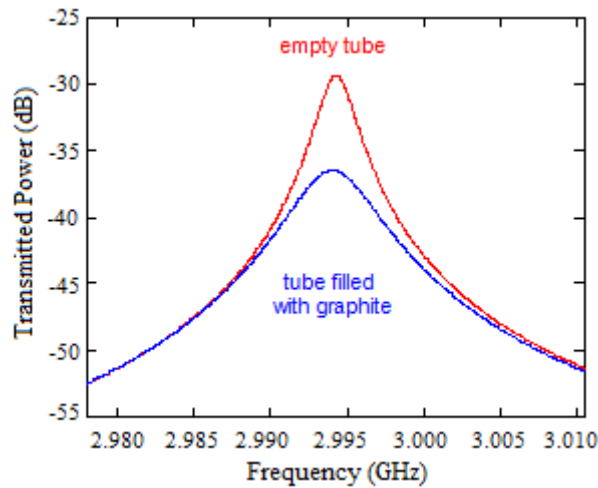


Figure 4.14: Resonant traces for graphite powder.

In addition, the sample magnetisation was examined because the nanotube powder attracts magnets. The magnetisation as a function of the applied magnetic field was measured using a vector vibrating sample magnetometer [14]. Fig. 4.15 shows the magnetisation versus the applied magnetic field curves for the nanotubes. The detailed properties of the hysteresis loop were not included in the analysis because a tiny magnetic signature was observed in the CNTs sample. The size of the coercive field, saturation fields and the remanences in the hysteresis loop are too small to analyse.

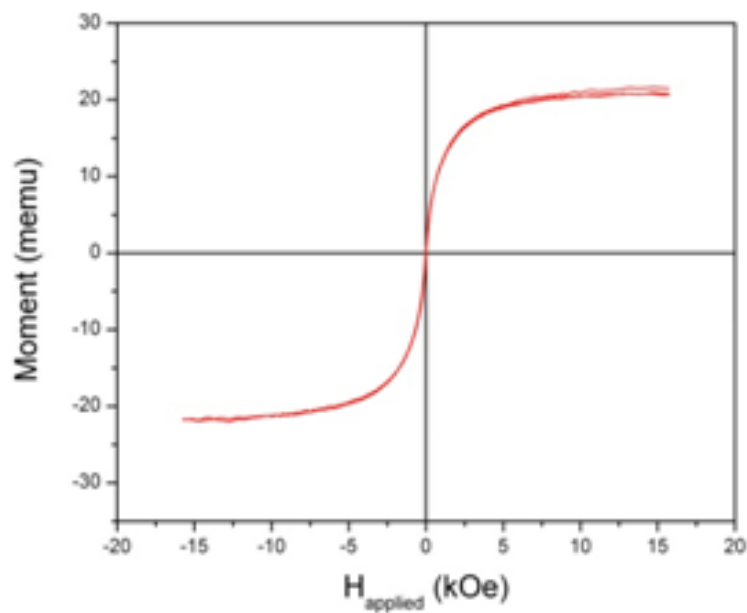


Figure 4.15: Magnetisation versus applied magnetic field curve for the sample with a mass of 7mg .

4.7 Conclusions

In this work, microwaves have been used as a means of exciting currents in CNTs, thus avoiding the requirement for electrical contacts. In the experiments, a powder CNT sample is placed in a region of high microwave magnetic field in a 3GHz copper hairpin cavity and the electrical properties of the CNTs are determined using the cavity perturbation technique.

The sample exhibited screening of the microwave magnetic field, that is, an increased resonant frequency $\Delta f_0 = 9.0 \pm 0.3\text{MHz}$ relative to the empty tube, together with very large losses, that is, an increased 3dB bandwidth of $\Delta f_B = 18 \pm 1\text{MHz}$. Such screening is usually observed only in powdered metals having a conductivity large enough for the mean particle size to become much greater than the microwave skin depth. Based on a mean nanotube radius of 0.7nm , the recorded nanotube sheet resistance is $R_{sq} \approx 10\mu\Omega$. An extremely high conductivity of $\sim 10^{15}\text{S/m}$ was estimated from the sheet resistance of individual nanotube. The nanotubes appear to have the highest conductivity of any non-superconducting material.

The morphology and microstructural studies conducted on the CNTs sample confirmed the presence of magnetic impurities in the sample. EDX gave atomic % ratios of 96.5:2.7:0.8 for C:O:Fe. These impurities are thought to arise from the substrate used to stimulate the growth of the nanotubes during production. Since the small amount of Fe is well dispersed, it is not expected to influence the microwave measurements significantly.

Since the properties of CNTs are very sensitive to their geometries, the applied magnetic field could have changed their internal structures, thus causing the magnetic signatures in the CNTs. This work is inconclusive because not all samples examined show such striking behaviour, so future work should consider experimenting on wider range of frequencies and on well-aligned nanotubes.

4.8 References

- [1] N. Patil, J. Deng, S. Mitra, and H. S. Philip Wong, Circuit-Level Performance Benchmarking and Scalability Analysis of Carbon Nanotube Transistor Circuits, *IEEE Transactions on Nanotechnology*, Vol. 8, No. 1, January 2009.
- [2] G. F. Close, S. Yasuda, B. Paul, S. Fujita, and H. S. Philip Wong, A 1 GHz Integrated Circuit with Carbon Nanotube Interconnects and Silicon Transistors, *Nano Lett.*, 2008, 8 (2), pp. 706–709.
- [3] M. P. Anantram and F. Leonard, *Physics of Carbon Nanotube Electronic Devices*, Institute of Physics Publishing, *Rep. Prog. Phys.* 69 (2006), pp. 507-561.
- [4] D. M. Pozar, *Microwave Engineering*, 3rd Edition, Page 266, John Wiley & Sons, Inc., ISBN: 978-0-471-44878-5, 2005.
- [5] L. Reimer, T. Tamir, A. L. Schawlow, *Scanning Electron Microscopy: Physics Of Image Formation and Microanalysis Mark*, 2nd Edition, Springer Berlin Heidelberg, ISBN: 3540639764, 1998.
- [6] B. Fultz, J. M. Howe, *Transmission electron microscopy and diffractometry of materials*, 3rd Edition, Springer, ISBN: 3540738851, 2007
- [7] G. H Bourne, J. F. Danielli, *International Review of Cytology: A Survey of Cell Biology*, volume 58, Academic Press, ISBN-10 / ASIN: 0123643589, 1979.
- [8] N. Pierard, A. Fonseca, Z. Konya, I. Willems, G. Van Tendeloo and J. B.Nagy, Production of short carbon nanotubes with open tips by ball milling, *Chemical Physics Letters* 335 (2001) 1-8.
- [9] P. A. Anderson, A. R. Armstrong, P. D. Barkera, M. J. Edmondson, P. P. Edwards and A. Porch, Rubidium doped zeolite rho: structure and microwave conductivity of a metallic zeolite, *Dalton Transactions*, DOI: 10.1039/b402668c, July 2004.
- [10] A. P. Gregory and R. N. Clarke, A Review of RF and Microwave Techniques for Dielectric Measurements on Polar Liquids, *IEEE Transactions on Dielectrics and Electrical Insulation*, Vol. 13, No. 4, pp. 727-743, August 2006.
- [11] A. Porch, Private Communications, 2007-2008.

- [12] B. L. Sands, N. S. Siefert, and B. N. Ganguly, Design and measurement considerations of hairpin resonator probes for determining electron number density in collisional plasmas, IOP Publishing, Plasma Sources Sci. Technol. 16 (2007), pp. 716–725.
- [13] D. Kajfez and P. Guillon (Editors), Dielectric Resonators, Second Edition, Noble Publishing Corporation, Atlanta, 1998, ISBN 1-884932-05-3.
- [14] B. C. Dodrill, J. R. Lindemuth, and J. K. Krause, Magnetic Anisotropy: Measurements with a Vector Vibrating Sample Magnetometer, Lake Shore Cryotronics, Inc., 575 McCorkle Blvd., Westerville, Ohio, USA.

Chapter 5

3D Electromagnetic Simulation of Hairpin Resonator for the Microwave Characterisation of Carbon Nanotubes Sample

5.1 Introduction

A 3D modelling of the characterisation of tightly packed nanotubes using a hairpin resonator is now described. The hairpin resonator is modelled using the COMSOL multiphysics software. It is examined how the presence of nanotubes can change the magnitude of the magnetic field screening in the hairpin resonator. The magnetic field screening is examined from the shift in the resonant frequency of the hairpin resonator by introducing different conductivities. Also, the broadening of the spectral response bandwidth of the hairpin resonator when the nanotubes are introduced into the cavity is examined. As part of the analysis, the Q of the hairpin resonator is calculated from the simulation and its value compared with that obtained from experiment.

In this simulation, COMSOL serves to solve a complex Helmholtz equation. The Helmholtz equation relates the amplitude of the magnetic potential to the electrical conductivity of the measurement sample. The partial differential equation (PDE) that describes the electromagnetic system is formulated, and the solution of this PDE used to examine the properties of the nanotubes sample. More detailed information of the COMSOL software is provided in the following section.

5.2 Background

COMSOL multiphysics [1] is a finite element analysis software used for the modeling and simulation of any physics-based system. The original COMSOL codes were written by graduate students for a graduate course at the Royal Institute of Technology in Stockholm, Sweden [1]. The COMSOL multiphysics modelling environment has a functionality optimised for the analysis of electromagnetic effects, components and systems. The underlying equations for electromagnetics are available in all the application modes, which is a feature unique to COMSOL multiphysics. Any model developed using the electromagnetic module can be transformed into a model described by the underlying partial differential equations. Simulation models can be exported to COMSOL script and MATLAB. Also, it is possible to incorporate the models with other products in the MATLAB family such as Simulink.

In COMSOL, the finite element method approximates the solution within each element using some elementary shape function, which can be constant, linear, or of higher order. The mesh for the problem must be generated before it can be solved, and the requirement for a finer or coarser mesh depends on the element order in the model. The mesh resolution is determined by the variation in the solution, which could be due to geometrical factors, skin effect, or wavelength.

Also, the COMSOL package is equipped with an option to make a selection from a set of solvers for PDE-based problems. The selection of the solver type is dependent on the application mode and the analysis type, which includes stationary, eigenfrequency, transient, time-dependent, and parametric analyses. The simulation results obtained from the solver are analysed using the postprocessing and visualization tools, which include advanced graphics, data display and export functions. From the postprocessing tool, the solutions of the electromagnetic problem such as the field patterns, resonant frequency, f_0 and the quality factor, Q can be retrieved. It is possible to undertake further postprocessing calculations by exporting the solutions to MATLAB.

The later sections discuss the detailed modeling and postprocessing of the hairpin resonator.

5.2.1 Theory of COMSOL Multiphysics [4]

In this work, the AC Power Electromagnetics mode is employed for the electromagnetic simulation of the hairpin resonator. COMSOL computes the PDE coefficients based on the parameters of the application mode [2].

The PDE for this application mode is formulated by deriving the equation this mode solves, starting with the Ampere's law [3]:

$$\nabla \times \mathbf{H} = \mathbf{J} + \frac{\partial \mathbf{D}}{\partial t} = \sigma \mathbf{E} + \sigma \mathbf{v} \times \mathbf{B} + \mathbf{J}^e + \frac{\partial \mathbf{D}}{\partial t} \quad (5.1)$$

where \mathbf{H} is the magnetic field intensity, \mathbf{J} is the electric current density, \mathbf{D} is the electric flux density, \mathbf{E} is the electric field intensity, \mathbf{v} is the velocity of the conductor and \mathbf{B} is the magnetic flux density. Assuming time-harmonic fields and using the potentials yields:

$$\mathbf{B} = \nabla \times \mathbf{A} \quad (5.2)$$

$$\mathbf{E} = -\nabla V - \frac{\partial \mathbf{A}}{\partial t} \quad (5.3)$$

Combining Eq. 5.2 and Eq. 5.3 with the constitutive relationships $\mathbf{B} = \mu_0(\mathbf{H} + \mathbf{M})$ and $\mathbf{D} = \epsilon_0 \mathbf{E} + \mathbf{P}$, the Ampere's law is rewritten as

$$(j\omega\sigma - \omega^2\epsilon_0)\mathbf{A} + \nabla \times (\mu_0^{-1}\nabla \times \mathbf{A} - \mathbf{M}) - \sigma \mathbf{v} \times (\nabla \times \mathbf{A}) + (\sigma + j\omega\epsilon_0)\nabla V = \mathbf{J}^e + j\omega\mathbf{P} \quad (5.4)$$

where σ is the electrical conductivity, ω is the angular frequency, \mathbf{A} is the magnetic vector potential, \mathbf{M} is the magnetisation and \mathbf{P} is the polarisation density.

The following boundary and interface conditions are applied to the electromagnetic problem. The interface condition is [2]:

$$\mathbf{n}_2 \times (\mathbf{H}_1 - \mathbf{H}_2) = \mathbf{J}_s \quad (5.5)$$

The magnetic field boundary condition that specifies the tangential component of the magnetic field strength at the boundary is:

$$\mathbf{n} \times \mathbf{H} = \mathbf{n} \times \mathbf{H}_0 \quad (5.6)$$

In addition, specify the surface current flowing along the longitudinal direction (z -direction) and the surface-current boundary condition:

$$-\mathbf{n} \times \mathbf{H} = J_{sz} \mathbf{e}_z; \quad \mathbf{n} \times (\mathbf{H}_1 - \mathbf{H}_2) = J_{sz} \mathbf{e}_z \quad (5.7)$$

The electric insulation boundary condition sets the magnetic field to zero:

$$\mathbf{n} \times \mathbf{H} = \mathbf{0} \quad (5.8)$$

The magnetic potential boundary condition that specifies the magnetic potential is given by:

$$A_z = A_{0z} \quad (5.9)$$

The magnetic insulation boundary condition that sets the magnetic potential to zero at the boundary is:

$$A_z = 0 \quad (5.10)$$

The continuity boundary condition that allows the continuity of the tangential component of the magnetic field is:

$$\mathbf{n} \times (\mathbf{H}_1 - \mathbf{H}_2) = \mathbf{0} \quad (5.11)$$

A solution to an AC power electromagnetic problem is required for a conductor carrying alternating currents [3]. Consider a homogenous dielectric with a dielectric constant ϵ and magnetic permeability μ , and it is assumed that there is no charge at any point. The fields must satisfy a set of Maxwell equations:

$$\nabla \times E = -\mu \frac{\partial H}{\partial t} \quad (5.12)$$

$$\nabla \times H = -\varepsilon \frac{\partial E}{\partial t} + J \quad (5.13)$$

where E is the electric field, H is the magnetic field and J is the current density. When there is no current, the magnetic field H can be eliminated from the second set and both fields satisfy wave equations with wave speed v :

$$v = \sqrt{\varepsilon\mu} \quad (5.14)$$

$$\Delta E - \varepsilon\mu \frac{\partial^2 E}{\partial t^2} = 0 \quad (5.15)$$

$$\Delta H - \varepsilon\mu \frac{\partial^2 H}{\partial t^2} = 0 \quad (5.16)$$

For the charge-free homogenous dielectric with conductivity σ , the current density is:

$$J = \sigma E \quad (5.17)$$

The ohmic resistance damps the waves, leading to Eq. 5.18 & Eq. 5.19.

$$\Delta E - \mu\sigma \frac{\partial E}{\partial t} - \varepsilon\mu \frac{\partial^2 E}{\partial t^2} = 0 \quad (5.18)$$

$$\Delta H - \mu\sigma \frac{\partial H}{\partial t} - \varepsilon\mu \frac{\partial^2 H}{\partial t^2} = 0 \quad (5.19)$$

Using the complex form, the case of time-harmonic field is treated by replacing E with $E^{j\omega t}$. The conductivity is calculated using Eq. 5.18 & 5.19, and it can be used to examine the skin effect and other properties of the current-carrying conductor.

Before solving a radio frequency (RF) cavity problem, the cavity layout must be described in such a way that it can be utilized as input for solution of the Helmholtz equation. Given a source-free, linear, isotropic, homogenous region, the Maxwell-Curl equations [4] that constitute two equations for the two unknowns, \bar{E} and \bar{H} in phasor form are:

$$\nabla \times \bar{E} = -j\omega\mu\bar{H} \quad (5.20)$$

$$\nabla \times \bar{H} = j\omega\varepsilon\bar{E} \quad (5.21)$$

Solve Eq. 5.20 and Eq. 5.21 for either \bar{E} or \bar{H} by taking the Curl of these equations to yield:

$$\nabla \times \nabla \times \bar{E} = -j\omega\mu\nabla \times \bar{H} = \omega^2\mu\varepsilon\bar{E} \quad (5.22)$$

Eq. 5.22 is simplified using the vector identity $\nabla \times \nabla \times \bar{A} = \nabla(\nabla \cdot \bar{A}) - \nabla^2\bar{A}$, which is valid for the rectangular components of an arbitrary vector \bar{A} . Since $\nabla \cdot \bar{E} = 0$ in a source-free region,

$$\nabla^2\bar{E} + \omega^2\mu\varepsilon\bar{E} = 0 \quad (5.23)$$

Eq. 5.23 is known as the wave equation or Helmholtz equation for \bar{E} . Derive an identical equation for \bar{H} using the same steps:

$$\nabla^2\bar{H} + \omega^2\mu\varepsilon\bar{H} = 0 \quad (5.24)$$

Using the AC Power Electromagnetics mode [5], the equation solved in COMSOL is a complex Helmholtz equation for the amplitude of the magnetic potential:

$$-\nabla \cdot \left(\frac{1}{\mu} \nabla A_z \right) + k^2 A_z = 0 \quad (5.25)$$

$$k = \sqrt{j\omega\sigma - \omega^2\varepsilon} \quad (5.26)$$

The boundary conditions are considered carefully, and either the magnetic potential A_z or the normal derivative of the same field is specified on the outer surface. The final solution of the AC Power Electromagnetics equation is a complex value that reflects the time lag between the surface and the interior.

5.2.2 Skin Depth

The skin effect is observed during the flow of an alternating current. Electrons tend to move along the surface of the conductor and the current density near the surface of the conductor is greater than that at its core. A change in the amplitude and direction of the current induces a magnetic field that pushes electrons towards the exterior of the conductor. As shown in Eq. 5.28, the skin depth increases when the applied frequency decreases. In an infinitely thick plane conductor, the current density decreases exponentially with depth d from the surface, yielding [6]:

$$J = J_s e^{-d/\delta_s} \quad (5.27)$$

where δ_s is the skin depth. The skin depth, also known as the characteristic depth of penetration, is defined as

$$\delta_s = \sqrt{\frac{2}{\omega\mu\sigma}} = \sqrt{\frac{1}{\pi f\mu_0\sigma}} \quad (5.28)$$

where f is the frequency, σ is the conductivity, μ_0 is the permeability of free space and ω is the angular frequency. The skin depth δ_s of the conductor is the depth at which the current density reduces in magnitude to $1/e$ or 36.8%.

Skin depth plays an important role when investigating screening in a conducting sample. The radius of the conducting sample must be larger than the skin depth for screening to be observed.

Since conductivity of the sample is an input parameter in this simulation, the average conductivity of a CNT is now derived starting from the density of states calculation.

5.2.3 Calculation of the Charge Density in a Carbon Nanotube

In chapter 4, it was reported that the resonant frequency (f_0) of a hairpin resonator increased when a sample of carbon nanotubes (CNTs) was placed in the magnetic field anti-node of the resonator cavity. The resonant frequency increased because the sample screened the microwave magnetic field. It was also observed that the resonant frequency increased when small copper spheres were inserted into the hairpin cavity. According to the experimental analyses in section 4.6, the nanotubes served to screen the microwave magnetic field more than the copper spheres. This is remarkable as copper (Cu) is known to have a very high conductivity but the experimental results suggest that the conductivity of a CNT is higher. Consider a comparison of a CNT to a copper wire. The physical dimensions of the structures are shown in Fig. 5.1.

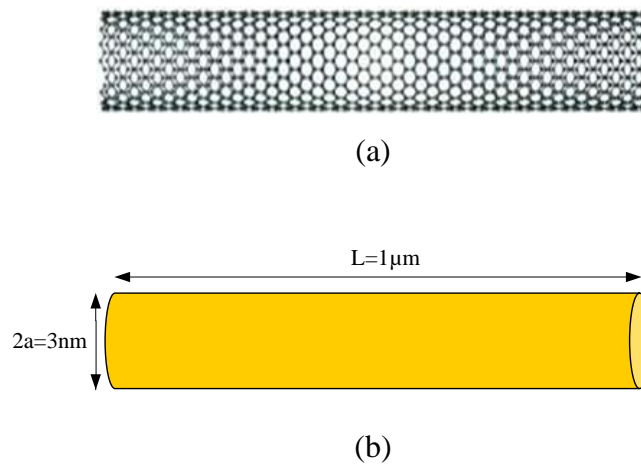


Figure 5.1: Cylindrical geometry of (a) carbon nanotube, and (b) copper wire.

For both structures shown in Fig. 5.1, the length and radius are $1\mu\text{m}$ and 1.5nm , respectively. The charge density in the CNT is compared to that of copper wire using fundamental calculations. Since the structures are treated as conductors and quantisation ignored, classical calculations can be used to describe the movement of electrons along their lengths. The electron concentration in copper is $8.5 \times 10^{28}/\text{m}^3$ but only the free electrons are included in

this calculation. The free electrons occupy the lowest energy states and they form a sphere in momentum space [7]. Fig. 5.2 shows the surface of the sphere also known as the Fermi surface. The free electrons that contribute to current flow are those near the Fermi surface, and it is assumed that they are $k_B T$ below the Fermi energy, where k_B is Boltzmann's constant and T is the absolute temperature [7].

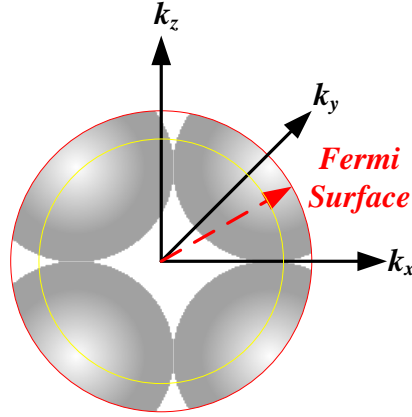


Figure 5.2: The representation of the Fermi surface in momentum space [7].

The radius of the Fermi sphere (red) and the inner sphere (yellow) shown in Fig. 5.2 are expressed in Eq. 5.29 and Eq. 5.30, respectively [7].

$$K_1 = \sqrt{\frac{2mE_F}{\hbar^2}} \quad (5.29)$$

$$K_2 = \sqrt{\frac{2mE_F - k_B T}{\hbar^2}} \quad (5.30)$$

where E_F is the Fermi energy of copper, \hbar is the reduced Planck's constant and m is the electron mass. In order to determine the number of free electrons in copper, the ratio of the volume of the Fermi sphere to the volume of the inner sphere is calculated, yielding:

$$ratio = 1 - \frac{(E_F - k_B T)^{3/2}}{(E_F)^{3/2}} \quad (5.31)$$

Based on the expression shown in Eq. 5.31 and applying E_F of $7eV$, the calculated ratio is 0.0056. Therefore, the number of free electrons in copper is the known number of electrons divided by 178, which is the inverse of the calculated ratio.

The charge density per unit length, Q , in the copper wire is given by:

$$Q = NA \quad (5.32)$$

where N is the number of free electrons per cubic meter and A is the cross-sectional area of the copper wire. From Eq. 5.32, the charge density in the copper wire is $3.4 \times 10^9/m$.

To calculate the charge density in the CNT, start from the density of states calculation [8]. The density of states $D(E)$ for the CNT is determined using Eq. 5.33.

$$D(E) = \sum_v \frac{2L}{\pi a \gamma} \frac{E}{\sqrt{E^2 - E_v^2}} \quad (5.33)$$

$$E_v = \frac{2a\gamma}{d} \left(b - \frac{2m}{3} \right) \quad (5.34)$$

where L is the nanotube length, d is the diameter, $a = 3a_0/2$, a_0 is the carbon-carbon length, m is an index of the CNT, b is the energy subband index, E is energy, and γ is the tight-binding overlap integral. Fig. 5.3 shows the plot of the density of states for the CNT considered. The charge density in the CNT structure is related to $D(E)$ and the Fermi-Dirac distribution $f(E)$ by:

$$Q_{cnt} = \int_0^\infty D(E) f(E) dE \quad (5.35)$$

Performing the integration described in Eq. 5.35 over all possible energies, the charge density in the CNT structure is $4.3 \times 10^7/m$. An atom density of $3.6 \times 10^7/m$ is estimated using the formula shown in Eq. 2.25 (section 2.1.2). These separate calculations point to similar number of atoms contributing to the conducting ‘‘cloud’’.

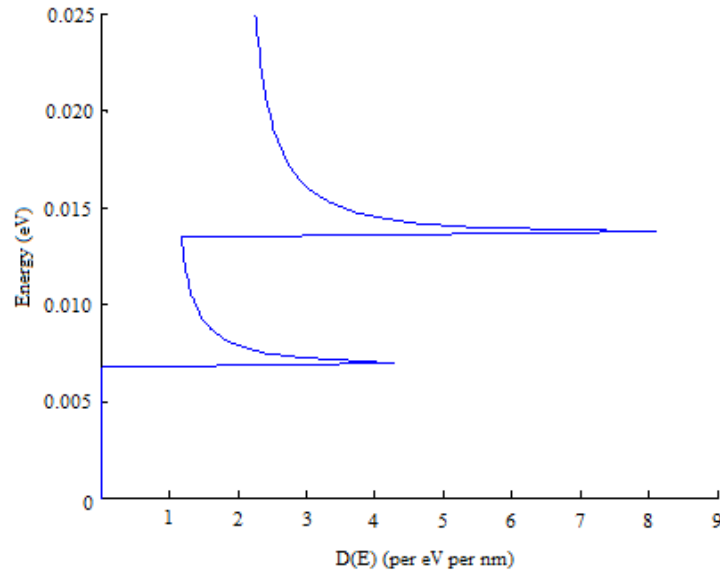


Figure 5.3: Density of states $D(E)$ for a carbon nanotube calculated using Eq. 5.33.

Since the conductivity of copper is known to be $5.96 \times 10^7 S/m$ [7], the conductivity of the nanotube can be estimated using Eq. 5.37. Conductivity is related to the number of electrons in the structure and Fermi velocity of charge carriers as:

$$\sigma \propto Nqv \quad (5.36)$$

The charge carried by electrons in the structures shown in Fig. 5.1 is $Q \approx NqA$, which is related to conductivity as:

$$\frac{Q_{cu} \times v_{cu}}{Q_{cnt} \times v_{cnt}} \equiv \frac{\sigma_{cu}}{\sigma_{cnt}} \quad (5.37)$$

where v is the Fermi velocity and q is the electron charge. Using Eq. 5.37, the conductivity of an individual nanotube is estimated to be $4 \times 10^5 S/m$, which is lower than that of copper. This conductivity is significantly different from that extracted from (Δf_0) of the hairpin resonator described in chapter 4, where a conductivity of around $10^{15} S/m$ was obtained from the experiment.

The detailed 3D modelling of microwave characterization of CNTs sample using hairpin resonator is now discussed. This enables validation of the experimental results discussed in chapter 4. The average conductivity of the nanotubes derived is an input parameter in this simulation.

5.3 Modelling of Hairpin Resonator

5.3.1 Introduction

In this section, the 3D modelling of the hairpin resonator used to investigate the screening properties of nanotubes sample is presented. The fundamental theory of a hairpin resonator was introduced in section 4.4. The hairpin resonator is a variant of the wide microstrip line, which supports transverse electromagnetic waves (TEM) along its length [9]. The hairpin structure is made out of a copper strip bent at one end to form the short-circuited termination while open at the other end. Resonance occurs when the length, l of the hairpin is integer multiples of a quarter wavelength. The fundamental resonance mode occurs at $l = \lambda/4$ with the corresponding resonant frequency, f_0 given by [9][10]:

$$f_0 = \frac{c}{4l} \approx \frac{75}{l(\text{mm})} \text{ GHz} \quad (5.38)$$

As shown in Eq. 5.38, the resonant frequency, f_0 of the hairpin resonator only depends on l . Fig. 5.4 shows a schematic diagram of the hairpin resonator considered in this work.

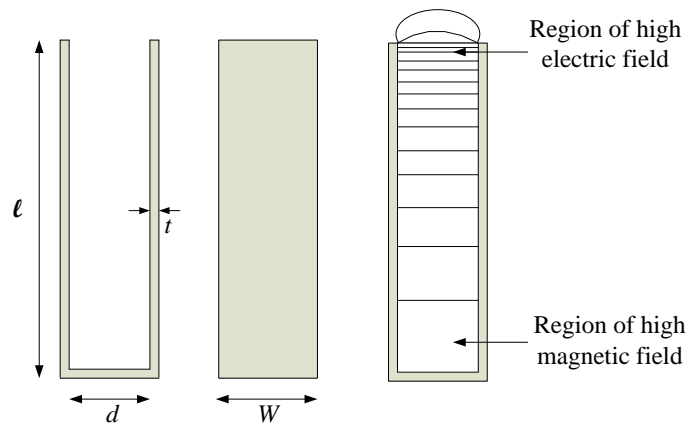


Figure 5.4: Schematics of the hairpin resonator, where l is the plate length, W is the plate width, d is the separation between the plates and t is the plate thickness [9][11].

When the hairpin resonates, the electric and magnetic fields increase drastically and a standing wave occurs on the hairpin such that the voltage (current) is maximum (minimum) at the open circuit end and minimum (maximum) at the short circuit end. As illustrated in Fig. 5.4, the electric field along the length of the hairpin is concentrated at the open circuit end and zero at the short circuit end. The magnetic field is largest at the short circuit end and minimal at the open circuit end. In this work, the concentrated magnetic field is used to induce current in a tightly packed sample of carbon nanotubes.

The quality factor, Q is another parameter relevant to the studies in this chapter. The unloaded quality factor, Q_U of the hairpin resonator is derived starting with the transmission line (TL) resonator [9][10]. As shown in Eq. 5.39, the Q_U of transmission line resonators has two components (Q_c and Q_d):

$$Q_U^{-1} = Q_c^{-1} + Q_d^{-1} \quad (5.39)$$

$$Q_c = n\pi/4\alpha_c l \quad (5.40)$$

$$Q_d = n\pi/4\alpha_d l = (\tan \delta)^{-1} \quad (5.41)$$

where α_c is the attenuation constant due to conductor loss, α_d is the attenuation constant due to dielectric loss, δ is the skin depth of copper, Q_c is the conductor quality factor and Q_d is the dielectric quality factor. Since the spacing between the plates of the hairpin structure is filled with air, $\tan \delta = \alpha_d = 0$ and Q_d becomes infinitely large. Therefore, the unloaded quality factor of the hairpin resonator is only dependent on Q_c .

$$Q_U = Q_c = \pi/4\alpha_c l \quad (5.42)$$

The attenuation constant due to conductor loss, α_c is related to the hairpin resistance R and characteristic impedance Z_0 as:

$$\alpha_c = R/2Z_0 \quad (5.43)$$

$$Z_0 = \sqrt{L/C} \quad (5.44)$$

The inductance L and capacitance C are related to the hairpin structure as:

$$L \approx \mu_0 d / W \quad (5.45)$$

$$C \approx \varepsilon_0 W / d \quad (5.46)$$

Substituting the equations for L and C into Eq. 5.44 yields

$$Z_0 = \sqrt{\frac{\mu_0}{\varepsilon_0}} \left(\frac{d}{W} \right) \quad (5.47)$$

The hairpin resistance per unit length is given by [9][10]:

$$R = \frac{\rho l}{W\delta} + \frac{\rho l}{W\delta} = \frac{2R_s}{W} \quad (5.48)$$

where ρ is the resistivity, surface resistance, $R_s = \rho/\delta$ and $W\delta$ is the area of each hairpin plate. Substituting Eq. 5.47 and Eq. 5.48 into Eq. 5.43 yields:

$$\alpha_c = \frac{R_s}{\sqrt{\mu_0/\varepsilon_0} d} \quad (5.49)$$

$$Q_U = \frac{\pi \sqrt{\mu_0/\varepsilon_0} d}{4R_s l} \quad (5.50)$$

Applying $f_0 = c/4l$ and $c = 1/\sqrt{\varepsilon_0\mu_0}$ into Eq. 5.50, the Q_U of the hairpin resonator becomes:

$$Q_U = \frac{\pi f_0 \mu_0 d}{R_s} \quad (5.51)$$

The relationship between the loaded quality factor, Q_L of the resonator and Q_U is given by [12]:

$$Q_L = Q_U (1 - 10^{IL/20}) \quad (5.52)$$

where IL is the insertion loss.

In the next section, the hairpin resonator is modelled to give a resonance frequency of 3GHz. The field patterns, resonant frequency and the quality factor are obtained directly from the output file of the COMSOL software.

5.3.2 Hairpin Resonator Model

The electromagnetic simulation of the hairpin resonator used for observing screening in CNTs is now described. The simulation is performed using COMSOL Multiphysics. Fig. 5.5 shows the 3D structure of the hairpin resonator used in this work. The hairpin is constructed from a 1mm thick copper sheet with length $l = 23\text{mm}$, width $W = 5\text{mm}$, and diameter $d = 3\text{mm}$. Based on these dimensions, the resonant frequency, f_0 of the hairpin resonator is 3GHz. The hairpin structure is enclosed in a radiation shield made out of copper. As shown in Fig. 5.5, the radiation shield has two parts; the cylindrical housing surrounding the hairpin and the base for the cylindrical housing fitting. The radiation shield prevents the loss of stored energy to the surroundings, ensuring high quality factor.

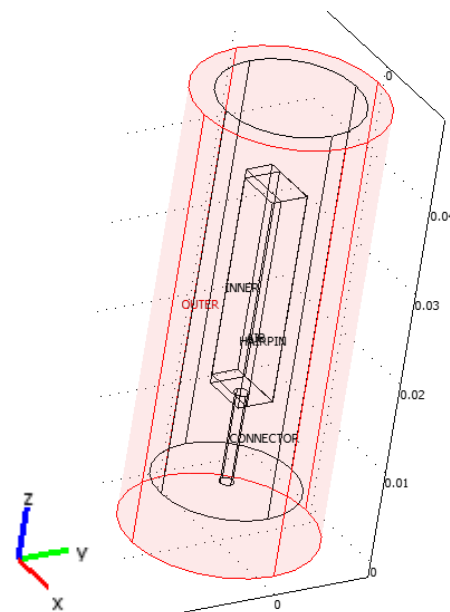


Figure 5.5: 3D geometry of the hairpin resonator modelled using COMSOL Multiphysics.

Different regions of the resonator are defined in the subdomain settings of COMSOL by stating the properties of the material such as permittivity and permeability. In the boundary settings function, the boundary conditions described in section 5.2.1 are applied. At the interface between two different media, the continuity boundary condition shown in Eq. 5.11 is applied.

In order to reduce the size of the cavity problem and achieve a converged solution, only one half of the problem geometry is specified as shown in Fig. 5.6. The ‘create composite object’ function was used to cut the hairpin resonator model in half. An efficient boundary condition is then applied on the truncated section of the geometry to minimize the problem size.

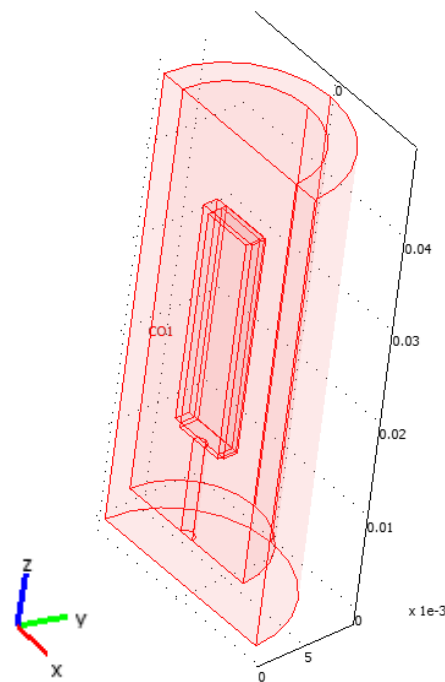


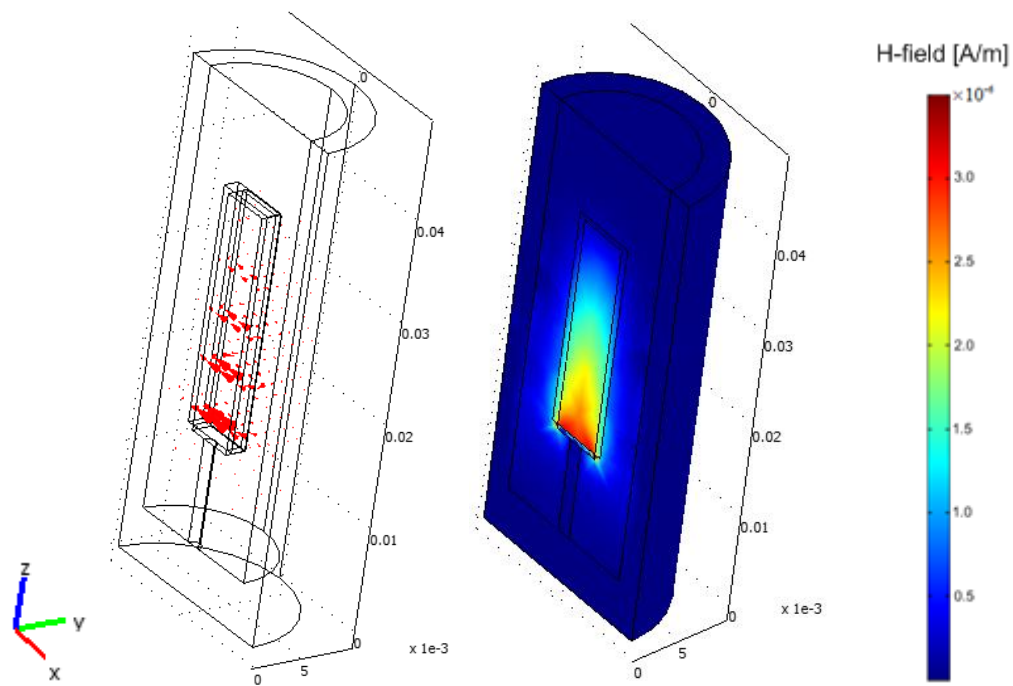
Figure 5.6: 3D geometry of the hairpin resonator cut in half to reduce the size of the RF cavity problem.

The mesh for the hairpin structure to be analysed is set before solving the Helmholtz equation (Eq. 5.25) that describes the RF cavity problem. A finer mesh is applied where the electromagnetic field is highly concentrated, which aids the solution convergence. The

eigenfrequency solver is used to obtain f_0 and Q of the hairpin resonator. In this case, COMSOL computes the solutions of the transverse electric (TE) mode to obtain the field patterns, and they are stored in the post-processing tool of COMSOL. This allows interpolation of the fields at various points to compute other quantities such as conductor losses, energy stored within the cavity and screening.

5.3.3 Simulation Results

The 3D simulation of the hairpin resonator using the RF module in COMSOL is now presented. In the 3D solid shown in Fig. 5.6, the x -axis, y -axis and z -axis represent the positions along the width, radius and length of the hairpin resonator, respectively. Fig. 5.7a and Fig. 5.7b show the streamline and contour plot of the magnetic field and electric field in the empty hairpin resonator, respectively. As expected the magnetic field is concentrated at the short-circuited end of the hairpin while the electric field is largest at the open end of the hairpin. As depicted by the bar in Fig. 5.7, the maximum magnetic field strength is around 3.5×10^{-6} A/m while the maximum electric field is around 4.2×10^{-1} V/m.



(a)

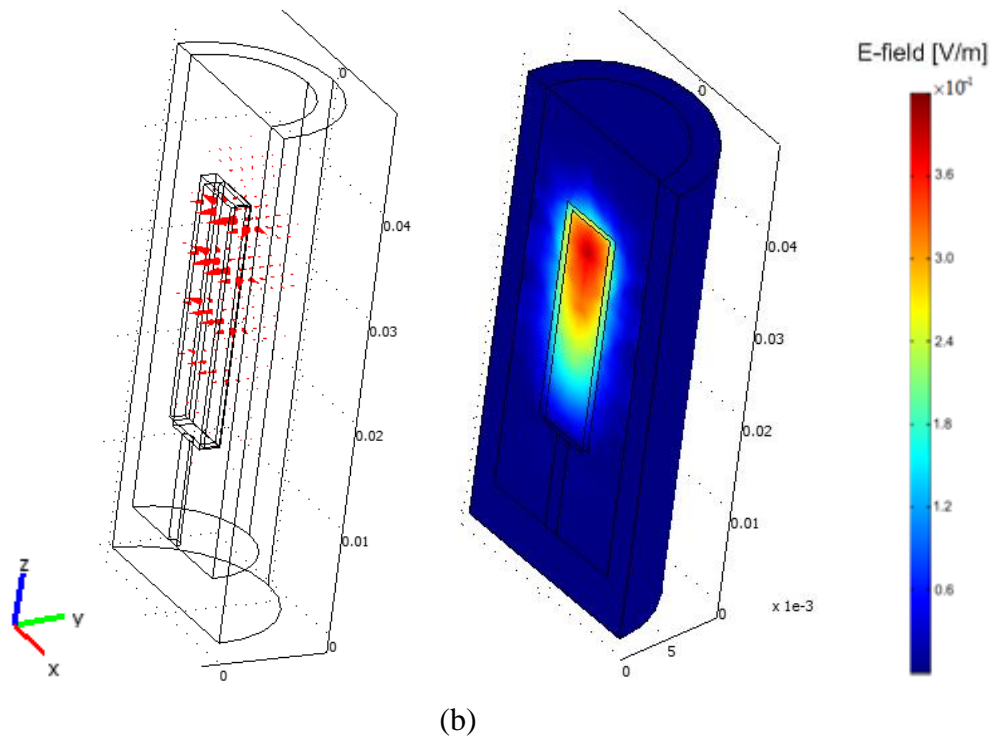


Figure 5.7: Field concentration and distribution within the hairpin. (a) High magnetic field concentration observed at the short-circuited end of the hairpin. (b) Electric field is maximum at the open end of the hairpin.

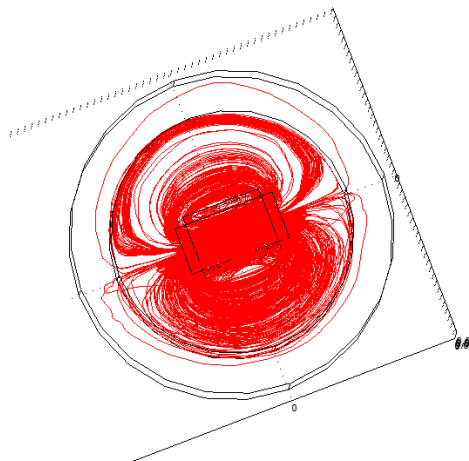


Figure 5.8: Top view of the magnetic field pattern within the radiation shield of the hairpin resonator.

In COMSOL the resonant frequency, f_0 is computed by numerically integrating the field components at various points. Based on the simulation results, the resonance frequency of the empty hairpin resonator is 3.009GHz, which is very close to the value of 3GHz recorded in the experiment using a network analyzer. The Q_U of the empty hairpin resonator obtained from the simulation is 1399, and the corresponding Q_L value calculated using Eq. 5.52 is 1220. A Q_L value similar to the 1200 recorded in the experiment was obtained.

As shown in Fig. 5.9 the sample of nanotubes is introduced in the high magnetic field region of the hairpin structure. The nanotubes sample had a packing density of 3.25g/cm^3 and a conductivity of $4 \times 10^5 \text{ S/m}$, estimated in section 5.1. As shown in Fig. 5.7 and Fig. 5.9, there is no obvious change in the magnetic field strength when the sample is introduced into the resonator cavity. The maximum magnetic field strength only reduced from $3.5 \times 10^{-6} \text{ A/m}$ to $3.2 \times 10^{-6} \text{ A/m}$ because the sample absorbed some of the field.

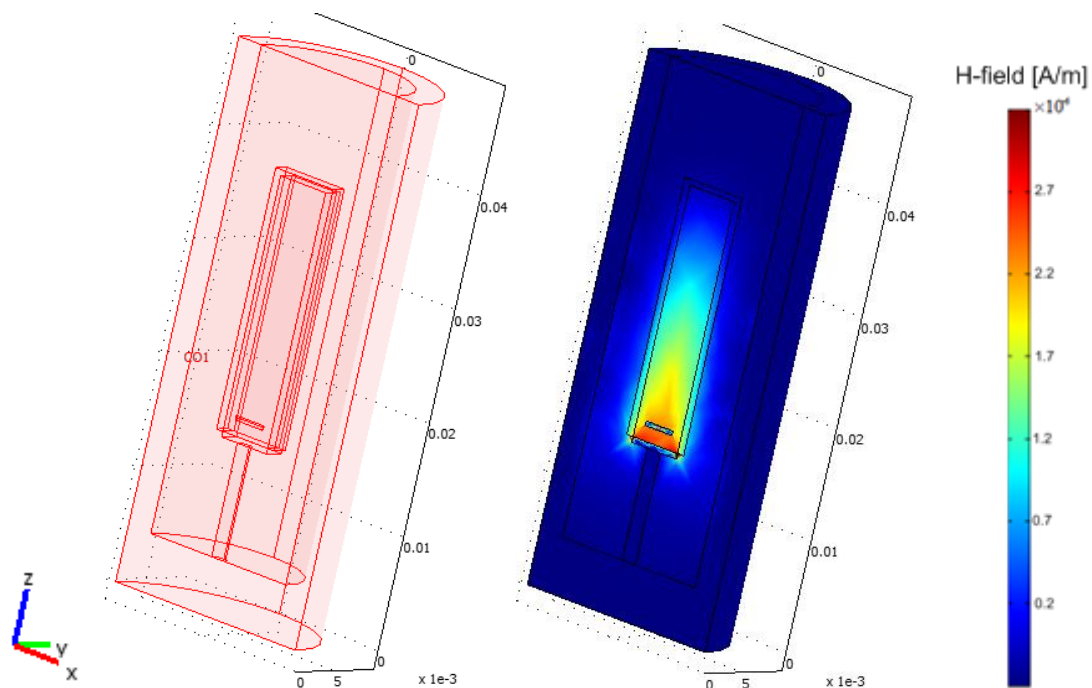


Figure 5.9: The hairpin resonator is loaded with tightly packed nanotubes sample (0.4mm^3 in volume corresponding to a sample mass of 1.3mg).

Furthermore, based on the results shown in Table 5.1, there is no significant change in f_0 when the conductivity of the sample is 4×10^5 S/m, implying the conductivity is not high enough to screen the field. The magnitude of field screening is examined from the change in the resonant frequency (Δf_0) of the hairpin resonator by introducing materials with different conductivities. Table 5.1 shows the trend of the field screening as the conductivity of the sample increases. The simulation result confirms that Δf_0 increases as the conductivity of the sample increases. Screening was only observed when the conductivity of the sample is higher than 10^7 S/m.

A conductivity of $\sim 10^{15}$ S/m was found in the experiment, therefore computation of Δf_0 was conducted for this conductivity. A value of $\Delta f_0 = 10$ MHz was observed, which is similar to that of the experiment, and validates the simulation procedure.

In addition, a validation of the simulation has been carried out by introducing copper into the resonator cavity. As discussed in chapter 4, a resonant frequency shift of 1.4 MHz was observed on insertion of copper spheres ($\sigma = 5.99 \times 10^7$ S/m) into the cavity. A similar scenario has been confirmed in the COMSOL simulation by inserting a copper rod into the resonator cavity, which results in a resonant frequency shift of 1.5 MHz. This confirms that the simulation result is nearly the same as that of the experiment with an error of $< 5\%$.

Conductivity (S/m)	Resonant Frequency (Hz)	Q_U	Q_L
1×10^5	3001417305	908	794
1×10^6	3005485516	1181	1032
1×10^7	3008674750	1327	1160
1×10^8	3010474929	1372	1199
1×10^9	3011215490	1391	1216
1×10^{10}	3012371644	1394	1218
1×10^{15}	3019527680	1398	1220

Table 5.1: Recorded increase in the resonant frequency as the conductivity of the nanotubes sample increases.

Also, the quality factor, Q was computed when the nanotubes sample is in the hairpin resonator cavity. The field components are extracted from the COMSOL output file and a numerical integration was performed to obtain the parameters required for the hairpin resonator Q calculations (Eq. 5.52).

For an empty resonator, the value of Q_L is 1220 but when a sample of nanotubes having a conductivity of 4×10^5 S/m is inside the region of high magnetic field, the value of Q_L reduces to 1160. There is a reduction in the value of Q_L because the sample absorbed some of the microwave energy. The sample of nanotubes introduced some loss in the resonant device, which is evident from the Q_L value.

The Q_L value was used to calculate the change in the spectral response bandwidth Δf_B from the well-known Q factor expression, $Q = f_0/\Delta f_B$. The bandwidth increased by 2.5MHz because of the microwave loss introduced by the nanotubes. The sample decreased the overall loss of the resonator, leading to bandwidth broadening.

In this simulation, similar Δf_0 have been observed when compared to that of the experiment but there is difference in Δf_B . In the experiment, Δf_B was found to be 18MHz while that recorded in this simulation is only 2.5MHz. This suggests that there is something else contributing to the experimental observations.

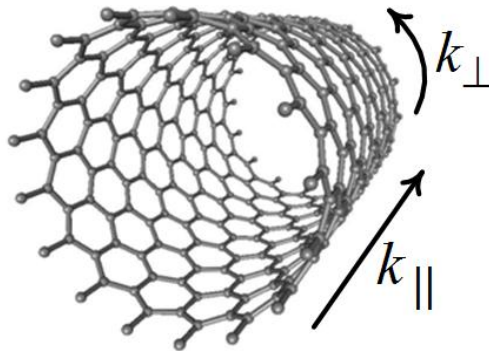
In the following section, quantization in CNTs and the effect of axial magnetic fields on their electronic structure are discussed.

5.4 Discussion

In a CNT, the electron wave number perpendicular to the axis of the CNT, k_{\perp} , is quantized. The quantized k_{\perp} are determined by the boundary condition shown in Eq. 5.53 [13].

$$\pi d k_{\perp} = 2\pi j \quad (5.53)$$

where j is an integer and d is the nanotube diameter. Fig. 5.10 shows the quantization of wave-states around a CNT. As shown in Fig. 5.10, there is a significant spacing between the quantised values of k_{\perp} for CNTs with small diameters ($\sim 1\text{nm}$). Fig. 5.10b shows the contour plot of graphene valence states for a CNT. The parallel lines represent the wavevectors allowed in the cylindrical boundary condition, and each line is a 1D subband. Electrons are free to move over long distances when the electron wave number is continuous.



(a)

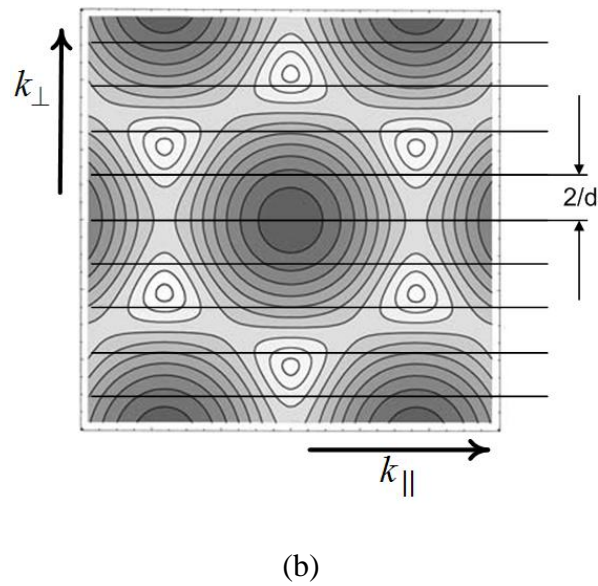


Figure 5.10: Quantization of electronic wave states around a carbon nanotube. (a) The parallel and perpendicular axes of a CNT. (b) The contour plot of graphene valence states for a CNT [13].

For a CNT with large diameter, the spacing between the values of k_{\perp} are small, which may lead to continuum of k_{\perp} states. In such case, electrons could travel in the circumferential direction of the CNT as shown in Fig. 5.11. Since some of the CNTs in the experimental sample have diameters much larger than 5nm, electrons travelling in the circumferential directions can acquire magnetic moments, and consequently screen the surrounding magnetic field.

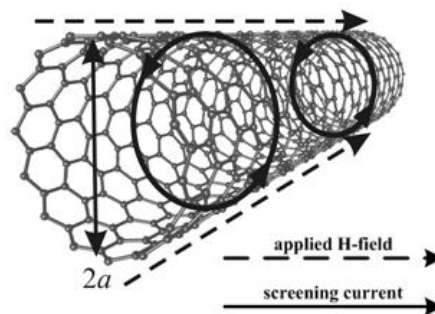


Figure 5.11: Screening currents for the microwave magnetic field applied parallel to the nanotube axis.

When a magnetic field is applied parallel to a CNT, the allowed k_{\perp} states in the CNT are modified by an Aharonov-Bohm phase [13]. In the presence of an axial magnetic field, the boundary condition for electron wave states around the CNT is given by:

$$\pi d k_{\perp} + 2\pi \frac{\phi}{\phi_0} = 2\pi j \quad (5.54)$$

$$\phi = \frac{B_{\parallel} \pi d^2}{4} \quad (5.55)$$

where ϕ is the flux passing through the CNT, B_{\parallel} is the axial magnetic field, and $\phi_0 = h/e$ is the flux quantum. The second term in Eq. 5.54 is the Aharonov-Bohm phase acquired by the electrons as they encircle a magnetic flux. The allowed k_{\perp} states is shifted by an amount $(2/d)(\phi/\phi_0)$, which consequently changes the bandgap of the CNT. The change in the bandgap of the CNT is given by [13][14]:

$$\frac{dE_{gap}}{dB} \approx 2\hbar v_F \frac{dk_{\perp}}{dB} \approx 2 \frac{ev_F d}{4} \quad (5.56)$$

where E_{gap} is the energy bandgap, \hbar is the reduced Planck's constant, v_F is the Fermi velocity and the quantity, $\mu_{orb} = ev_F d/4$ is the orbital magnetic moment. Electronic states near the energy gap are predicted [14][15] to have an orbital magnetic moment much larger than Bohr magneton, which is the magnetic moment due to an electron spin. This large moment is thought to cause the magnetic behaviour of CNTs [16][17].

5.5 Conclusions

In this chapter, the 3D modelling of tightly packed carbon nanotubes using a hairpin resonator was described. The conductivity of the sample is one of the input parameters of this simulation. An expression for the average conductivity of the CNTs was derived starting from the density of states calculations. Based on the calculations described in section 5.1, the conductivity used in the simulation is 4×10^5 S/m.

For a conductivity of 4×10^5 S/m, the resonant frequency of the hairpin decreases by 3.5MHz. An incremental shift was observed in the resonant frequency of the hairpin resonator only when a sample of highly conductive nanotubes ($> 10^7$) is inside its cavity. In such a case, the resonant frequency increased because the sample screened the applied microwave energy. As shown in Table 5.1, there is a trend in Δf_0 as the conductivity of the sample is varied incrementally. Also, the screening properties of the sample were observed when its conductivity is $\sim 10^{15}$ S/m (based on the value extracted from the experimental results). The resonant frequency increased from 3.009GHz to 3.090GHz, which is comparable to that recorded in the experiment.

In addition, it was examined how Q_L changes when the hairpin cavity is loaded with the nanotubes sample. The Q_L value reduces from 1220 to 1160 due to the microwave loss introduced by the sample in the resonant device. The broadening of the spectral response bandwidth (i.e. 2.5MHz) is also due to the sample loss.

In the simulations, a resonant frequency shift was observed only when the sample inside the cavity has a high conductivity ($> 10^7$ S/m). This observation suggests that the nanotubes used in the experiment have extremely low sheet resistance.

5.6 References

- [1] COMSOL Multiphysics, Model Library, COMSOL Multiphysics Version 3.2, September 2005.
- [2] COMSOL Multiphysics Modelling Guide by COMSOL AB, Version 3.2, Application Modes, Page 2.
- [3] COMSOL Multiphysics Modelling Guide by COMSOL AB, Version 3.2, AC Power Electromagnetics Page(s): 96-99.
- [4] M. N.O. Sadiku, Numerical Techniques in Electromagnetics, Wave Equations Page 8, CRC Press, Boca Raton, 1992.
- [5] COMSOL Multiphysics Model Library by COMSOL AB, Version 3.2, Skin Effect in a Conductor Page(s): 72-79.
- [6] Electromagnetics Module, COMSOL Multiphysics User's Guide by COMSOL AB, Version 3.2, Skin Depth Page(s): 172-190.
- [7] N. W. Ashcroft, N. David Mermin, Solid State Physics, Harcourt College Publishers, New York, 1st Edition, 1976.
- [8] S. Datta, Quantum Transport: Atom to Transistor, Schrodinger Equation Page 33, Cambridge University Press, ISBN - 139780521631457.
- [9] A. Porch, Private Communications, 2008
- [10] D. M. Pozar, Microwave Engineering, Third Edition, John Wiley and Sons, N. Y., 2005.
- [11] R. Goritz, A. Masood, O. Castell, D. A. Barrow, C. Allender and A. Porch Microwave Compositional Analysis of Solvent Matrices in Microcapillary Manifold Systems, The Proceedings of MicroTAS 2007 Conference, Paris, pp. 1689-1691, October 2007.
- [12] A. Masood, Thesis: Microwave Resonators for Highly Sensitive Compositional Analysis of Solvents in Microcapillary Systems, Cardiff University, June 2009.
- [13] E. D. Minot, Yuval Yaish, Vera Sazonova and Paul L. McEuen, Determination of Electron Orbital Magnetic Moments in Carbon Nanotubes (Letters to Nature),

Laboratory of Atomic and Solid-State Physics, Cornell University, Ithaca, New York 14853, USA.

- [14] J. P. Lu, Novel Magnetic Properties of Carbon Nanotubes, *Physical Review Letter* 74, pp. 1123-1126 (1995).
- [15] H. Ajiki and T. Ando, Electronic States of Carbon Nanotubes, *J. Phys. Soc. Jpn* 62, pp. 1255-1266 (1993).
- [16] A. P. Ramirez et al. Magnetic-Susceptibility of Molecular Carbon Nanotubes and Fullerite, *Science* 265, pp. 84-86 (1994)
- [17] O. Chauvert et al. Magnetic Anisotropies of Aligned Carbon Nanotubes, *Physical Review B* 52 R6963-R6966 (1995).

Chapter 6

Conclusions and Future Work

6.1 General Observation

In this work, theoretical and experimental studies of the conductivity of carbon nanotubes (CNTs) in steady state and at microwave frequencies have been described. A numerical simulation was used to understand the operation and performance of a Metal-Oxide-Semiconductor (MOS) device based on a CNT. The simulation technique employed is based on a numerical algorithm employed by John et. al [1]. Poisson's equation is solved self-consistently with Schrodinger's equation using the finite difference and scattering matrix techniques, respectively. Knowledge of the CNT bandstructure is required for this simulation method. Using the zone-folding method (ZFM), we obtained the bandstructure of CNTs from the pi-orbital nearest-neighbour tight-binding bandstructure of graphene.

From the simulation results in chapter 2 it was observed that a MOS device based on a semiconducting CNT exhibits intriguing electronic properties. The I-V characteristics shown in Fig. 2.21 show that the current of the CNFET device saturates at a drain-source bias of 0.2V. This shows that carbon nanotube field-effect transistors (CNFETs) have good switching performance, which makes them useful in low voltage power switching applications.

In chapter 3, the output characteristics of a CNFET device were compared to those of a graphene field-effect transistor (GFET). To improve immunity to short channel effects, a fully wrapped gate is assumed for both devices. The simulation result in chapter 3 suggests that circuits based on graphene FETs may have a superior switching performance than those

based on CNTs. Comparing the I-V characteristics of these devices we observed that a full current saturation is achieved for the GFET because the transmission probability for electrons rises rapidly with energy.

The output characteristics of CNFETs depend on the nature of source and drain contacts, which is one of the issues in the development of CNT devices. In the simulation, the on-current of the CNFET device depends on the tunnelling barrier, the height of which is determined by the end contacts. The electronic properties of CNFETs having different end contacts (Silver (*Ag*), Iron (*Fe*), and Gold (*Au*)) was compared. A higher on-current was observed when *Ag* is used as the device contacts. This is because the barrier height for *Ag* is smaller when compared to that of *Fe* and *Au*.

Since the DC transport properties of CNTs vary considerably with differing contacts, we electron transport in CNTs was studied using non-contact means (chapter 4). In the experiment, a 3GHz microwave host cavity was used to study the conductivity of carbon nanotubes. Placing the CNTs in the high magnetic field region of the resonator cavity induces current in the CNTs. The CNTs used in the experiment screen the applied microwave magnetic field. The sheet resistance of the CNTs was extracted from the shift in the resonant frequency of the resonator when the CNTs are introduced into the cavity. A very low sheet resistance of $\sim 10^{-5} \Omega/sq$ was observed, which is very small for a non-superconducting material. Based on the sheet resistance, the conductivity of an individual nanotube was estimated to be $\sim 10^{-15} S/m$. Further experiment needs to be carried out on aligned nanotubes to justify this high conductivity.

Morphological and microstructural studies of the carbon nanotubes conducted on the sample of nanotubes confirmed the presence of impurities. Energy dispersive X-ray spectroscopy (EDX) gives atomic % ratios of 96.5:2.7:0.8 for Carbon:Oxygen:Iron.. The *Fe* impurities are from the substrates used to stimulate the growth of the nanotubes during production. Since the small amount of *Fe* is well dispersed, it is not expected to influence the microwave measurements significantly.

In chapter 5, a numerical simulation of a hairpin resonator was used to validate the experimental procedure. Conductivity of the sample is an input parameter in this simulation. The average conductivity of a CNT is $4 \times 10^5 \text{S/m}$ as estimated from its charge density. In the simulation, it was observed that the tightly packed CNTs only screen when the conductivity is $> 10^7 \text{S/m}$. The conductivity estimated from the charge density of a CNT is not high enough to produce a screening effect. This suggests that there might be something else contributing to the screening observed in chapter 4.

When the sample of CNTs is placed next to a magnet, it is attracted. The magnetic properties of the CNTs may have caused the screening effect observed in the microwave experiment. We have investigated ferromagnetism in the CNTs using vibrating sample magnetometer. As shown in Fig. 4.14, the hysteresis loops of the CNTs displayed a tiny magnetic hysteresis. Other researchers have also reported ferromagnetism in CNTs but the magnetic behaviour of the CNTs was linked to spin transport from the substrate to the nanotubes [2].

Since the properties of CNTs are very sensitive to their geometries, the applied magnetic field could have altered the energy bandgaps of the nanotubes, thus changing the microwave properties of the CNTs. This work is inconclusive because not all samples examined show such striking behaviour, so future work should consider experimenting on wider range of frequencies and on well-aligned nanotubes.

6.2 Future Outlook

As reported in this work, CNTs have intriguing electronic and magnetic properties. Therefore, they can serve as the building blocks of future magneto-electronic devices. Since device scaling is one of the technological challenges facing magnetoelectronics [3], CNTs can be employed as magneto-devices due to their small dimensions. Experimentally, a MOS

device having a doped nanotube as the source and drain contacts has been developed [4] but a magnetic device based on a nanotube is yet to be explored.

The presence of magnetic impurities in these CNTs and the variation in the sample geometry made it difficult to conclude the experimental work adequately. For future work, the experimental measurements should be repeated on pure and aligned nanotubes, which would make the microwave experiment more quantitative. In addition, it would give a better view of the magnetic behaviour of CNTs.

For microwave experiment on aligned nanotubes, one of the likely drawbacks is that the coating substance used during production may contaminate the nanotubes. It is possible to examine the properties of the aligned nanotubes if the properties of the coating substance are known. The microwave technique employed in this work can be used to obtain the properties of the coating substance in a similar procedure presented in section 4.5. In addition, future contactless experiment on CNTs should be performed over a wider range of frequencies.

Experimentally, it will be difficult to miniaturize a hairpin resonator on which to take measurement of samples with volumes much smaller than the one considered in this work. It is easier to miniaturize a dielectric resonator because its internal properties depend mainly on the type of dielectric used [5]. In Appendix 8, the simulation described in chapter 5 was repeated using a sapphire dielectric resonator. In future work, the sapphire dielectric resonator should be constructed and used to study a well-aligned nanotube sample.

In future work, microwaves studies should be conducted on graphene. Microwave characterisations of graphene would be more quantitative because they have a planar structure, and can be produced more easily.

6.3 References

- [1] D. L. John, L. C. Castro, P. J. S. Pereira, and D. L. Pulfrey, A Schrodinger-Poisson Solver for Modeling Carbon Nanotube FETs, Proc. NSTI Nanotech, vol. 3, pp. 65-68, 2004.
- [2] M. F. Islam, D. E. Milkie, O. N. Torrens, A. G. Yodh, and J. M Kikkawa, Magnetic Heterogeneity and Alignment of Single Wall Carbon Nanotubes, Physical Review 71, 201401(R), 2005
- [3] J. De Boeck, W Van Roy, J. Das, V. Motsnyi, Z. Liu, L. Lagae, H. Boeve, K. Dessenin and G. Borghs, Technology and Materials Issues in Semiconductor-Based Magnetoelectronics, Institute of Physics Publishing, Semicond. Sci. Technol. 17 (2002), pp. 342-354.
- [4] A. Javey, J. Guo, D. B. Farmer, Q. Wang, D. Wang, R. G. Gordon, M. Lundstrom, and H. Dai, Carbon Nanotube Field-Effect Transistors with Integrated Ohmic Contacts and High-K Gate Dielectrics, Nano Letters, Vol. 4, No. 3, pp. 447-450, 2004.
- [5] J. C. Sethares and S. J. Naumann, Design of Microwave Dielectric Resonators, IEEE Transactions on Microwave Theory and Techniques, Vol. 14, No. 1, pp. 2-7, Current Version: January, 2003.

Appendix 1

A1. Detailed Procedure for Implementing a Finite Difference Algorithm

The finite difference methods are based upon approximations, which permit replacing differential equations by finite difference equations. These finite difference approximations are algebraic in form and they relate the value of the dependent variable at a point in the solution region to some neighbouring point's value. A finite difference solution involves three steps:

- Dividing the solution region into a grid of nodes
- Approximating the specified differential equation by finite difference equivalent that relates the dependent variable at a point in the solution region to its value at the neighbouring points
- Solving the difference equations subject to the prescribed boundary conditions

The course of action depends on the nature of the problem, the solution region and the boundary conditions. The most commonly used grid patterns for two-dimensional problems are shown in Fig.1.1.

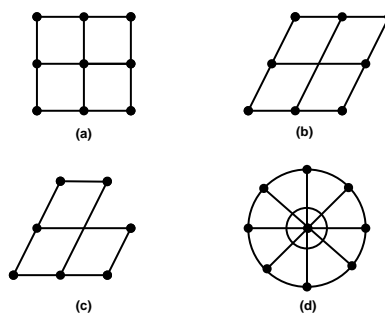


Figure A1.1: Common grid patterns: (a) rectangular grid, (b) skew grid, (c) triangular grid, (d) circular grid.

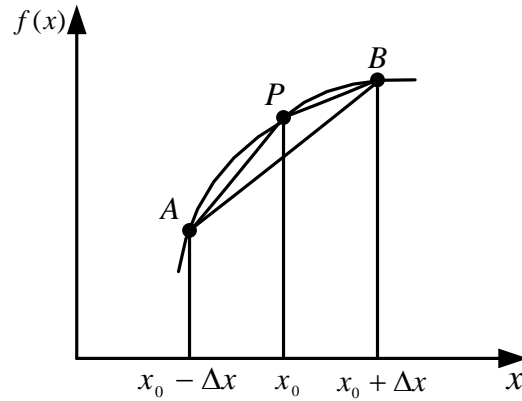


Figure A1.2: Estimates for the derivative of $f(x)$ at P using forward, backward, and central differences.

Constructing the finite difference approximations from a given differential equation involves estimating derivatives numerically. Given a function $f(x)$ shown in Fig. A1.2, its derivative i.e. the slope of the tangent at P by the slope of arc PB, can be approximated using the forward-difference formula

$$f'(x_0) \approx \frac{f(x_0 + \Delta x) - f(x_0)}{\Delta x} \quad (\text{A1.1})$$

Or the slope of the arc AP, yielding the backward-difference formula as

$$f'(x_0) \approx \frac{f(x_0) - f(x_0 - \Delta x)}{\Delta x} \quad (\text{A1.2})$$

Or the slope of the arc AB, resulting in the central-difference formula;

$$f'(x_0) \approx \frac{f(x_0 + \Delta x) - f(x_0 - \Delta x)}{2\Delta x} \quad (\text{A1.3})$$

Also, the second derivative of $f(x)$ at P can be estimated as

$$f''(x_0) \approx \frac{f'(x_0 + \Delta x/2) - f'(x_0 - \Delta x/2)}{\Delta x} = \frac{1}{\Delta x} \left[\frac{f(x_0 + \Delta x) - f(x_0)}{\Delta x} - \frac{f(x_0) - f(x_0 - \Delta x)}{\Delta x} \right] \quad (\text{A1.4})$$

OR

$$f''(x_0) \approx \frac{f(x_0+\Delta x) - 2f(x_0) + f(x_0-\Delta x)}{(\Delta x)^2} \quad (\text{A1.5})$$

Any approximation of a derivative in terms of values at a discrete set of points is known as finite difference approximation. In order to use the finite difference approach to find the solution of a function $\Phi(x, t)$, the solution region in the $(x - t)$ plane is divided into equal rectangles or meshes of sides Δx and Δt as shown in Fig. A1.3.

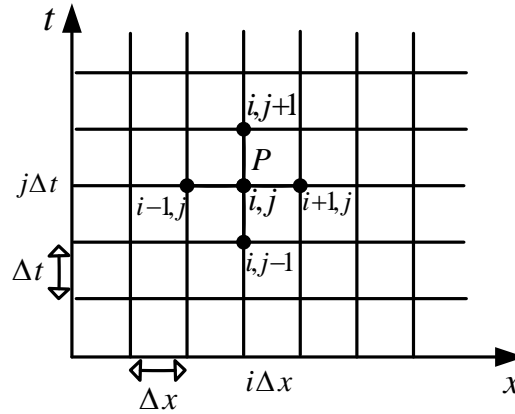


Figure A1.3: Finite difference mesh for two independent variables x and t .

Let the coordinates (x, t) of a typical grid point or node be

$$x = i\Delta x, \quad i = 0, 1, 2, 3, \dots \quad (\text{A1.6})$$

$$t = j\Delta t, \quad j = 0, 1, 2, 3, \dots \quad (\text{A1.7})$$

and the value of Φ at P be

$$\Phi_P = \Phi(i\Delta x, j\Delta t) = \Phi(i, j) \quad (\text{A1.8})$$

With this notation, the central difference approximations of the derivatives of Φ at the $(i, j)^{th}$ node are

$$\Phi_x|_{i,j} \approx \frac{\Phi(i+1,j) - \Phi(i-1,j)}{2\Delta x} \quad (\text{A1.9})$$

$$\Phi_t|_{i,j} \approx \frac{\Phi(i,j+1) - \Phi(i,j-1)}{2\Delta t} \quad (\text{A1.10})$$

$$\Phi_{xx}|_{i,j} \approx \frac{\Phi(i+1,j) - 2\Phi(i,j) + \Phi(i-1,j)}{(\Delta x)^2} \quad (\text{A1.11})$$

$$\Phi_{tt}|_{i,j} \approx \frac{\Phi(i,j+1) - 2\Phi(i,j) + \Phi(i,j-1)}{(\Delta t)^2} \quad (\text{A1.12})$$

Appendix 2

A2. Explanation of the Scattering Matrix Method by Analysing a Single Symmetric Planar Barrier of Defined Width and Height

To explain the scattering matrix method, consider a single symmetric planar barrier of defined width and height shown in Fig. A2.1. Let us assume a parabolic dispersion relation for an electron in the conduction band incident on the left side of the barrier. The solution of this dispersion relation can be separated into parallel and perpendicular parts relative to the barrier. Then, solve the 1D Schrödinger equation for the stationary solutions in the z -direction, which is perpendicular to the barrier.

$$\left(\frac{-\hbar^2}{2} \frac{\partial}{\partial z} \frac{\partial}{\partial m^*(z)} \frac{\partial}{\partial z} + V(z) \right) \Psi(z) = E\Psi(z) \quad (\text{A2.1})$$

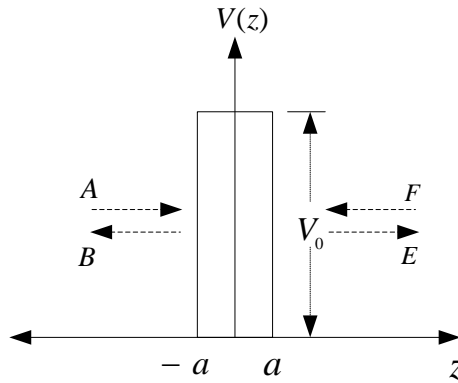


Figure A2.1: A simple rectangular tunnelling barrier

The solution of the Schrödinger equation (Eq.A2.1) can be written for different region of the barrier as

$$\Psi(z) = \begin{cases} Ae^{ikz} + Be^{-ikz} & z < -a \\ Ce^{\gamma z} + De^{-\gamma z} & -a < z < a \\ Ee^{ikz} + Fe^{-ikz} & z > a \end{cases} \quad (\text{A2.2})$$

$$k = \frac{\sqrt{2m^*E}}{\hbar} \quad (\text{A2.3})$$

$$\gamma = \frac{\sqrt{2m^*(V_0-E)}}{\hbar} \quad (\text{A2.4})$$

where k, γ are the wavevectors and a is the thickness of the barrier. The incoming and outgoing waves on the left side of the barrier are represented by coefficients A and B , respectively. Coefficients E and F are the incoming and outgoing waves on the right side of barrier, respectively. For the continuity of the envelope wavefunction Ψ , the coefficients A to F are related to each other through the boundary conditions. The boundary conditions is set by matching the wavefunctions and its derivatives at interfaces $z = -a$ and $z = a$. For instance, at $z = -a$:

$$\Psi_I(-a_-) = \Psi_{II}(-a_+) \quad (\text{A2.5})$$

$$\left. \frac{\partial \Psi_I}{\partial z} \right|_{-a_-} = \left. \frac{\partial \Psi_{II}}{\partial z} \right|_{-a_+} \quad (\text{A2.6})$$

$$Ae^{-ika} + Be^{ika} = Ce^{-\gamma a} + De^{\gamma a}, \quad (\text{A2.7})$$

$$ik[Ae^{-ika} - Be^{ika}] = \gamma[Ce^{-\gamma a} - De^{\gamma a}] \quad (\text{A2.8})$$

$$\begin{bmatrix} A \\ B \end{bmatrix} = \begin{bmatrix} \left(\frac{ik+\gamma}{2ik}\right) e^{(ik-\gamma)a} & \left(\frac{ik-\gamma}{2ik}\right) e^{(ik+\gamma)a} \\ \left(\frac{ik-\gamma}{2ik}\right) e^{-(ik+\gamma)a} & \left(\frac{ik+\gamma}{2ik}\right) e^{-(ik-\gamma)a} \end{bmatrix} \begin{bmatrix} C \\ D \end{bmatrix} \quad (\text{A2.9})$$

$$Ce^{\gamma a} + De^{-\gamma a} = Ee^{ika} + Fe^{-ika}, \quad (\text{A2.10})$$

$$\gamma[Ce^{\gamma a} - De^{-\gamma a}] = ik[Ee^{ika} - Fe^{-ika}] \quad (\text{A2.11})$$

$$\begin{bmatrix} C \\ D \end{bmatrix} = \begin{bmatrix} \left(\frac{ik+\gamma}{2\gamma}\right) e^{(ik-\gamma)a} & -\left(\frac{ik-\gamma}{2\gamma}\right) e^{-(ik+\gamma)a} \\ -\left(\frac{ik-\gamma}{2\gamma}\right) e^{(ik+\gamma)a} & \left(\frac{ik+\gamma}{2\gamma}\right) e^{-(ik-\gamma)a} \end{bmatrix} \begin{bmatrix} E \\ F \end{bmatrix} \quad (\text{A2.12})$$

$$\begin{bmatrix} A \\ B \end{bmatrix} = \begin{bmatrix} M_{11} & M_{12} \\ M_{21} & M_{22} \end{bmatrix} \begin{bmatrix} E \\ F \end{bmatrix} \quad (\text{A2.13})$$

where the 2×2 array elements are calculated from the matrix multiplication of the 2×2 arrays appearing in Eq. A2.9 and Eq. A2.12. A different matrix relation can be defined in terms of the outgoing fluxes, B and E , and incoming fluxes, A and F , on either side of the barrier as shown in Eq. A2.14.

$$\begin{bmatrix} B \\ E \end{bmatrix} = \begin{bmatrix} S_{11} & S_{12} \\ S_{21} & S_{22} \end{bmatrix} \begin{bmatrix} A \\ F \end{bmatrix} \quad (\text{A2.14})$$

where the S-Matrix is known as the scattering matrix. The transmission and reflection coefficients are obtained by setting $F = 0$, which yields Eq. A2.15 and Eq. A2.16.

$$T = |S_{21}|^2 k_1/k \quad (\text{A2.15})$$

$$R = |S_{11}|^2 \quad (\text{A2.16})$$

Considering the incident waves from the right side of the barrier, the transmission and reflection coefficients are determined by setting $A = 0$.

$$T = |S_{12}|^2 k_1/k \quad (\text{A2.17})$$

Appendix 3

A3. Derivation of the Laplace equation as a Function of Polar and Cylindrical Coordinates

In a closed metallic cylinder system, Poisson's equation restricted to just two dimensions by azimuthal symmetry is analysed below. In the CNT model devices, use of the polar and $x = r \cos(\theta)$ cylindrical coordinates is more convenient as the model is closer to this form. Now, the Laplace's equation for a function of polar and cylindrical coordinates is derived.

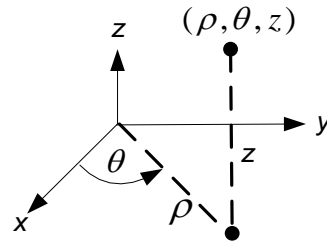


Figure A3.1: Cylindrical Coordinates.

Cylindrical and rectangular coordinates as shown in the Fig. A3.1 are related by

$$x = r \cos(\theta), y = r \sin(\theta), z = z, x^2 + y^2 = r^2 \text{ and } \theta = \tan^{-1} \left(\frac{y}{x} \right) \quad (\text{A3.1})$$

For instance, if x and y are both negative then y/x is positive but (x, y) is in the third quadrant which implies that θ must be between π and $3\pi/2$. Assuming v , which is a function of (x, y, z) , is continuous with continuous first and second partial derivatives in some region R . In view of the first equation in Eq. A3.1, v can be considered as a function of r , θ and z . Applying the chain rule to Eq. A3.1 yields:

$$\frac{\partial v}{\partial x} = \frac{\partial v}{\partial r} \frac{\partial r}{\partial x} + \frac{\partial v}{\partial \theta} \frac{\partial \theta}{\partial x} + \frac{\partial v}{\partial z} \frac{\partial z}{\partial x} = \frac{x}{\sqrt{x^2 + y^2}} \frac{\partial v}{\partial r} - \frac{y}{x^2 + y^2} \frac{\partial v}{\partial \theta} \quad (\text{A3.2})$$

$$\frac{\partial v}{\partial x} = \frac{x}{r} \frac{\partial v}{\partial r} - \frac{y}{r^2} \frac{\partial v}{\partial \theta} \quad (\text{A3.3})$$

Note: x and z are independent, which implies

$$\frac{\partial z}{\partial x} = 0 \quad (\text{A3.4})$$

Similarly,

$$\frac{\partial v}{\partial y} = \frac{y}{r} \frac{\partial v}{\partial r} - \frac{x}{r^2} \frac{\partial v}{\partial \theta} \quad (\text{A3.5})$$

Now the second derivatives are calculated by differentiating Eq. A3.5 with respect to x yielding

$$\frac{\partial^2 v}{\partial x^2} = \frac{\partial v}{\partial r} \frac{\partial}{\partial x} \left(\frac{y}{r} \right) - \frac{\partial v}{\partial \theta} \frac{\partial}{\partial x} \left(\frac{y}{r^2} \right) - \frac{x}{r} \frac{\partial}{\partial x} \left(\frac{\partial v}{\partial r} \right) - \frac{y}{r^2} \frac{\partial}{\partial x} \left(\frac{\partial v}{\partial \theta} \right) \quad (\text{A3.6})$$

On applying the chain rule to the last two terms of Eq. A3.6, we have

$$\frac{\partial^2 v}{\partial x^2} = \frac{y^2}{r^3} \frac{\partial v}{\partial r} + \frac{2xy}{r^4} \frac{\partial v}{\partial \theta} + \frac{x^2}{r^2} \frac{\partial^2 v}{\partial r^2} - \frac{2xy}{r^3} \frac{\partial^2 v}{\partial r \partial \theta} + \frac{y^2}{r^4} \frac{\partial^2 v}{\partial \theta^2} \quad (\text{A3.7})$$

Differentiating Eq. A3.5 with respect to y yields

$$\frac{\partial^2 v}{\partial y^2} = \frac{x^2}{r^3} \frac{\partial v}{\partial r} + \frac{2xy}{r^4} \frac{\partial v}{\partial \theta} + \frac{y}{r^2} \frac{\partial^2 v}{\partial r^2} - \frac{2xy}{r^3} \frac{\partial^2 v}{\partial r \partial \theta} + \frac{x^2}{r^4} \frac{\partial^2 v}{\partial \theta^2} \quad (\text{A3.8})$$

Summing Eq. A3.7 and Eq. A3.8 gives the Laplacian in cylindrical coordinates

$$\nabla^2 v = \frac{\partial^2 v}{\partial r^2} + \frac{1}{r} \frac{\partial v}{\partial r} + \frac{1}{r^2} \frac{\partial^2 v}{\partial \theta^2} + \frac{\partial^2 v}{\partial z^2} \quad (\text{A3.9})$$

Finally, for Laplace's equation in cylindrical coordinates and restricting the above equation to just two dimensions by azimuthal symmetry, write

$$\nabla^2 v = \frac{\partial^2 v}{\partial r^2} + \frac{1}{r} \frac{\partial v}{\partial r} + \frac{\partial^2 v}{\partial z^2} \quad (\text{A3.10})$$

Appendix 4

A4. A Detailed Procedure for Computing the Electrostatic Potential within the CNFET Structure

The electrostatic potential within the CNFET structure is computed by solving Eq. A4.1 using a 2D finite difference algorithm.

$$\frac{\partial^2 V(\rho, z)}{\partial \rho^2} + \frac{1}{\rho} \frac{\partial V(\rho, z)}{\partial \rho} + \frac{\partial^2 V(\rho, z)}{\partial z^2} = -\frac{Q}{\epsilon_0 \epsilon_r} \quad (\text{A4.1})$$

From the Poisson's equation, let V_{ij} represent an approximation to $V(\rho, z)$. To discretize Eq. A4.1, we replace both ρ and z derivatives with centered finite differences. Now divide the 2D cylindrical structure into $N\rho \times Nz$ grids and number each grid by an index h , where

$$h_\rho = \frac{R_t}{N\rho - 1}, \quad h_z = \frac{L_t}{Nz - 1} \quad (\text{A4.2})$$

$$\rho = (i - 1)h_\rho \quad i = 1, 2 \dots N\rho \quad (\text{A4.3})$$

$$z = (j - 1)h_z \quad j = 1, 2 \dots Nz \quad (\text{A4.4})$$

$$\frac{\partial V(\rho, z)}{\partial \rho} = \frac{V_{i+1, j} - V_{i-1, j}}{2h_\rho} \quad (\text{A4.5})$$

$$\frac{\partial^2 V(\rho, z)}{\partial \rho^2} = \frac{V_{i+1, j} - 2V_{i, j} + V_{i-1, j}}{h_\rho^2} \quad (\text{A4.6})$$

$$\frac{\partial^2 V(\rho, z)}{\partial z^2} = \frac{V_{i, j+1} - 2V_{i, j} + V_{i, j-1}}{h_z^2} \quad (\text{A4.7})$$

$$\frac{V_{i+1, j} - 2V_{i, j} + V_{i-1, j}}{h_\rho^2} + \frac{V_{i+1, j} - V_{i-1, j}}{2(i-1)h_\rho^2} + \frac{V_{i, j+1} - 2V_{i, j} + V_{i, j-1}}{h_z^2} = -\frac{Q(i, j)}{\epsilon_0 \epsilon_r} \quad (\text{A4.8})$$

$$\frac{1}{h_z^2} V_{i, j+1} + \left(\frac{1}{h_\rho^2} + \frac{1}{2(i-1)h_\rho^2}\right) V_{i+1, j} + \left(-\frac{2}{h_\rho^2} - \frac{2}{h_z^2}\right) V_{i, j} + \left(\frac{1}{h_\rho^2} - \frac{1}{2(i-1)h_\rho^2}\right) V_{i-1, j} + \frac{1}{h_z^2} V_{i, j-1} = -\frac{Q(i, j)}{\epsilon_0 \epsilon_r} \quad (\text{A4.9})$$

Multiplying h_ρ^2 on both sides yields:

$$\alpha^2 V_{i,j+1} + \frac{2i-1}{2i-2} V_{i+1,j} + (-2 - 2\alpha^2) V_{i,j} + \frac{2i-3}{2i-2} V_{i-1,j} + \alpha^2 V_{i,j-1} = -\frac{h_\rho^2 Q(i,j)}{\epsilon_0 \epsilon_r} \quad (\text{A4.10})$$

Define $k = i + (j - 1) N_\rho$

$$\alpha^2 V_{k+N_\rho} + \frac{2i-1}{2i-2} V_{k+1} + (-2 - 2\alpha^2) V_k + \frac{2i-3}{2i-2} V_{k-1} + \alpha^2 V_{k-N_\rho} = -\frac{h_\rho^2 Q(i,j)}{\epsilon_0 \epsilon_r} = 0 \quad (\text{A4.11})$$

At $\rho = 0$ ($i = 1$)

$$\lim_{\rho \rightarrow 0} \frac{1}{\rho} \frac{\partial V(\rho, z)}{\partial \rho} = \frac{\partial^2 V(\rho, z)}{\partial \rho^2} \quad (\text{A4.12})$$

The singularity at $\rho = 0$ was addressed by applying L'Hopital's rule to the Poisson equation's, yielding

$$2 \frac{\partial^2 V(\rho, z)}{\partial \rho^2} + \frac{\partial^2 V(\rho, z)}{\partial z^2} = -\frac{Q(0, z)}{\epsilon_0 \epsilon_r} \quad (\text{A4.13})$$

$$2 \frac{V_{2,j} - 2V_{1,j} + V_{0,j}}{h_\rho^2} + \frac{V_{1,j+1} - 2V_{1,j} + V_{1,j-1}}{h_z^2} = -\frac{Q(1, j)}{\epsilon_0 \epsilon_r} \quad (\text{A4.14})$$

$$\frac{1}{h_z^2} V_{1,j+1} + \frac{2}{h_\rho^2} V_{2,j} + \left(-\frac{4}{h_\rho^2} - \frac{2}{h_z^2}\right) V_{1,j} + \frac{2}{h_\rho^2} V_{0,j} + \frac{1}{h_z^2} V_{1,j-1} = -\frac{Q(1, j)}{\epsilon_0 \epsilon_r} \quad (\text{A4.15})$$

$$\alpha^2 V_{1,j+1} + 2V_{2,j} + (-4 - 2\alpha^2) V_{1,j} + 2V_{0,j} + \alpha^2 V_{1,j-1} = -\frac{h_\rho^2 Q(1, j)}{\epsilon_0 \epsilon_r} \quad (\text{A4.16})$$

$$\left. \frac{\partial V(\rho, z)}{\partial \rho} \right|_{\rho=0} = 0 \quad (\text{A4.17})$$

$$V_{2,j} - V_{0,j} = 0 \quad (\text{A4.18})$$

Applying Eq. A4.17 and Eq. A4.18 gives

$$\alpha^2 V_{1,j+1} + 4V_{2,j} + (-4 - 2\alpha^2)V_{1,j} + \alpha^2 V_{1,j-1} = -\frac{h_\rho^2 Q(1,j)}{\epsilon_0 \epsilon_r} \quad (\text{A4.19})$$

When $\rho = 0$ ($i = 1$)

$$\alpha^2 V_{k+N\rho} + 4V_{k+1} + (-4 - 2\alpha^2)V_k + \alpha^2 V_{k-N\rho} = -\frac{h_\rho^2 Q(1,j)}{\epsilon_0 \epsilon_r} = 0 \quad (\text{A4.20})$$

At the CNT radius $\rho = R_T$ ($i = \text{round}(\frac{R_T}{h_\rho})$), use

$$\epsilon_0 \epsilon_{ins} \left. \frac{\partial V(\rho,z)}{\partial \rho} \right|_{\rho=R_T^+} - \epsilon_0 \epsilon_t \left. \frac{\partial V(\rho,z)}{\partial \rho} \right|_{\rho=R_T^-} = -\frac{Q}{2\pi R_T} \quad (\text{A4.21})$$

$$\left. \frac{\partial V(\rho,z)}{\partial \rho} \right|_{\rho=R_T^+} = \frac{V_{i+1,j} - V_{i,j}}{h_\rho} \quad (\text{A4.22})$$

$$\left. \frac{\partial V(\rho,z)}{\partial \rho} \right|_{\rho=R_T^-} = \frac{V_{i,j} - V_{i-1,j}}{h_\rho} \quad (\text{A4.23})$$

Applying Eq. A4.21 – Eq. A4.23 to the nanotube-insulator interface yields:

$$\epsilon_0 \epsilon_{ins} \frac{V_{i+1,j} - V_{i,j}}{h_\rho} - \epsilon_0 \epsilon_t \frac{V_{i,j} - V_{i-1,j}}{h_\rho} = -\frac{Q(j)}{2\pi R_T} \quad (\text{A4.24})$$

$$\epsilon_{ins}(V_{i+1,j} - V_{i,j}) - \epsilon_t(V_{i,j} - V_{i-1,j}) = -\frac{Q(j)h_\rho}{2\pi \epsilon_0 R_T} \quad (\text{A4.25})$$

$$\epsilon_{ins} V_{i+1,j} + (-\epsilon_{ins} - \epsilon_t)V_{i,j} + \epsilon_t V_{i-1,j} = -\frac{Q(j)h_\rho}{2\pi \epsilon_0 R_T} \quad (\text{A4.26})$$

The boundary conditions for the potential are given by

1. Apply V_g , when $\rho = R$ or ($i = N\rho$), $V_{i,all} = V_g$
2. Apply V_s , when $z = 0$ or ($j = 1$), $V_{all,j} = V_s$
3. Apply V_d , when $z = Length$ or ($j = Nz$), $V_{all,j} = V_d$

Express these derived equations in a matrix form as shown in Eq. A4.27.

$$AV = -\frac{h_\rho^2 Q}{\epsilon_0 \epsilon_r} \quad (\text{A4.27})$$

where $V = [V_1 V_2 \cdots V_\alpha \cdots V_{N\rho \times Nz}]^T$, $Q = [Q_1 Q_2 \cdots Q_\alpha \cdots Q_{N\rho \times Nz}]^T$ and A is a $(N\rho \times Nz)^2$ sparse matrix. Once the charge density vector Q has been computed, the potential at every grid by simply inverting the A -matrix is then determined.

$$V = -A^{-1} \frac{h_\rho^2 Q}{\epsilon_0 \epsilon_r} \quad (\text{A4.28})$$

Boundary conditions for the system

Inside the cylindrical system, Eq. A4.28 gives the general form for all the grids. As a case study, assume that the grid with index j is on the boundary. When the simulation gets to the j_{th} row of the A -matrix, the general equation is no longer applicable because it requires the knowledge of the potential outside the system. In order to avoid this problem, modify both the A -matrix and the j_{th} element of the charge density vector Q . Replace the value of the potential $(-h_\rho^2 Q_j / \epsilon_0 \epsilon_r)$ at the particular grid with the boundary condition, which could be the source- V_s , drain- V_d and gate- V_g voltage of the CNFET device.

$$V_s = -\frac{\varphi}{q} \quad (\text{A4.29})$$

$$V_g = V_s + V_{gs} \quad (\text{A4.30})$$

$$V_d = V_s + V_{ds} \quad (\text{A4.31})$$

where φ is the work function, V_{gs} is the gate-source voltage and V_{ds} is the drain-source voltage. The j_{th} row of the modified A -matrix becomes $[0 \cdots 1 \cdots 0]$ and Q_j is now the corresponding boundary condition.

Appendix 5

A5. A Detailed Description of the Grid Implementation for the CNFET Device

In this section, the details of the cylindrical system grid implementations are provided.

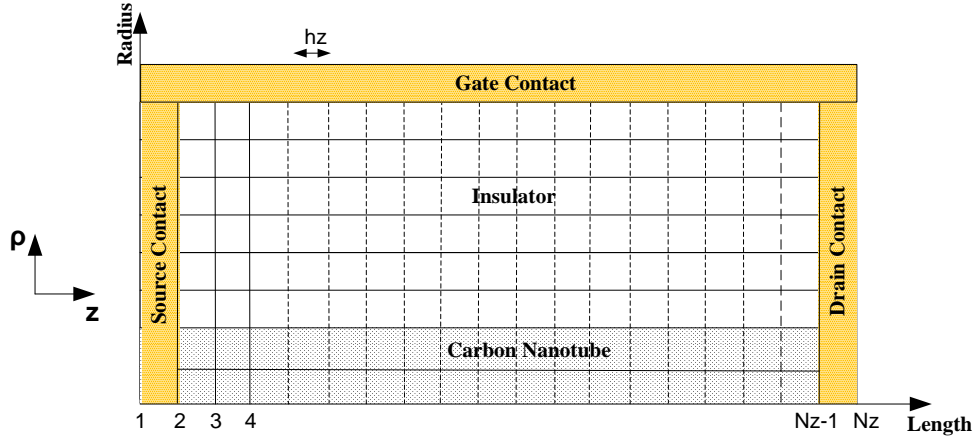


Figure A5.1: Grid implementation of the azimuthal symmetry in the coaxial CNFET.

$$z = (n-0.5)h_z \quad (\text{A5.1})$$

$$n = 1, 2, \dots, N_z - 1$$

$$A_n e^{ik_n z} + B_n e^{-ik_n z} = A_{n+1} e^{ik_{n+1} z} + B_{n+1} e^{-ik_{n+1} z} \quad (\text{A5.2})$$

$$k_n A_n e^{ik_n z} - k_n B_n e^{-ik_n z} = k_{n+1} A_{n+1} e^{ik_{n+1} z} - k_{n+1} B_{n+1} e^{-ik_{n+1} z} \quad (\text{A5.3})$$

$$L_n = \begin{bmatrix} e^{ik_n z} & e^{-ik_n z} \\ k_n e^{ik_n z} & -k_n e^{-ik_n z} \end{bmatrix} \quad (\text{A5.4})$$

$$R_n = \begin{bmatrix} e^{ik_{n+1} z} & e^{-ik_{n+1} z} \\ k_{n+1} e^{ik_{n+1} z} & -k_{n+1} e^{-ik_{n+1} z} \end{bmatrix} \quad (\text{A5.5})$$

$$[L_n] \begin{bmatrix} A_n \\ B_n \end{bmatrix} = [R_n] \begin{bmatrix} A_{n+1} \\ B_{n+1} \end{bmatrix} \quad (\text{A5.6})$$

For the source injection,

$$A_1 = \frac{2mf_s}{\pi\hbar^2k_s} \quad (\text{A5.7})$$

$$B_{N_z} = 0 \quad (\text{A5.8})$$

For drain injection,

$$A_1 = 0 \quad (\text{A5.9})$$

$$B_{N_z} = \frac{2mf_d}{\pi\hbar^2k_d} \quad (\text{A5.10})$$

$$[L_n] \begin{bmatrix} A_n \\ B_n \end{bmatrix} = [R_n] \begin{bmatrix} A_{n+1} \\ B_{n+1} \end{bmatrix} \quad (\text{A5.11})$$

$$\begin{bmatrix} A_n \\ B_n \end{bmatrix} = [L_n]^{-1}[R_n] \begin{bmatrix} A_{n+1} \\ B_{n+1} \end{bmatrix} \quad (\text{A5.12})$$

$$S_n = [L_n]^{-1}[R_n] \quad (\text{A5.13})$$

$$A^{-1} = \begin{bmatrix} a & b \\ c & d \end{bmatrix}^{-1} = \frac{1}{ad-bc} \begin{bmatrix} d & -b \\ -c & a \end{bmatrix} \quad (\text{A5.14})$$

$$\begin{bmatrix} A_1 \\ B_1 \end{bmatrix} = \prod_{n=1}^{N_z-1} S_n \begin{bmatrix} A_{N_z} \\ B_{N_z} \end{bmatrix} = [SS] \begin{bmatrix} A_{N_z} \\ B_{N_z} \end{bmatrix} \quad (\text{A5.15})$$

$$S_n = \frac{1}{L_{11}L_{22}-L_{12}L_{21}} \begin{bmatrix} L_{22} & -L_{12} \\ -L_{21} & L_{11} \end{bmatrix} \begin{bmatrix} R_{11} & R_{12} \\ R_{21} & R_{22} \end{bmatrix} \quad (\text{A5.16})$$

$$S_n = \frac{1}{L_{11}L_{22}-L_{12}L_{21}} \begin{bmatrix} L_{22}R_{11} - L_{12}R_{21} & L_{22}R_{12} - L_{12}R_{22} \\ L_{11}R_{21} - L_{21}R_{11} & L_{11}R_{22} - L_{21}R_{12} \end{bmatrix} \quad (\text{A5.17})$$

$$\begin{bmatrix} A_1 \\ B_1 \end{bmatrix} = \begin{bmatrix} SS_{11} & SS_{12} \\ SS_{21} & SS_{22} \end{bmatrix} \begin{bmatrix} A_{N_z} \\ B_{N_z} \end{bmatrix} \quad (\text{A5.18})$$

$$A_1 = SS_{11} A_{N_z} \quad (\text{A5.19})$$

$$A_{N_z} = \frac{A_1}{SS_{11}} \quad (\text{A5.20})$$

$$B_1 = SS_{21} A_{N_z} = \frac{SS_{21}}{SS_{11}} A_1 \quad (\text{A5.21})$$

Appendix 6

A6. Debye Length Theory

The Debye Length is the scale over which electrons screen out electric fields in a semiconductive material. The energy of a charge q in the potential to be screened is $q\varphi$, where φ is the potential. Using the Boltzmann distribution to define the probability of finding a particle within this energy, the number of particles within this potential is given by

$$N(\varphi) = N_0 e^{-q\varphi/(k_B T)} \quad (\text{A6.1})$$

where k_B is the Boltzmann constant, N_0 is the density when the potential is zero, T is the absolute temperature. The potential can be determined as a function of position by placing the charge density in Poisson's equation

$$\nabla^2 \varphi(r) = \frac{q N_0 (1 - e^{-q\varphi/(k_B T)})}{\epsilon_r \epsilon_0} \quad (\text{A6.2})$$

where ϵ_0 is the electric constant, ϵ_r is the relative static electric permittivity of the medium. The thermal voltage is defined as:

$$V_{th} = \frac{k_B T}{q} \quad (\text{A6.3})$$

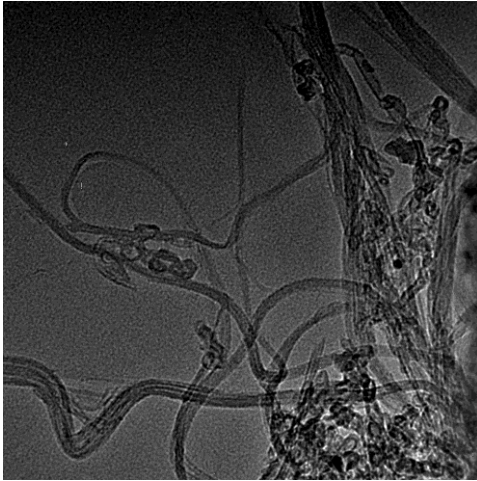
The Poisson equation becomes

$$\nabla^2 \left(\frac{\varphi(r)}{V_{th}} \right) = \left(\frac{1}{\lambda_D} \right)^2 (1 - e^{-\varphi(r)/V_{th}}) \quad (\text{A6.4})$$

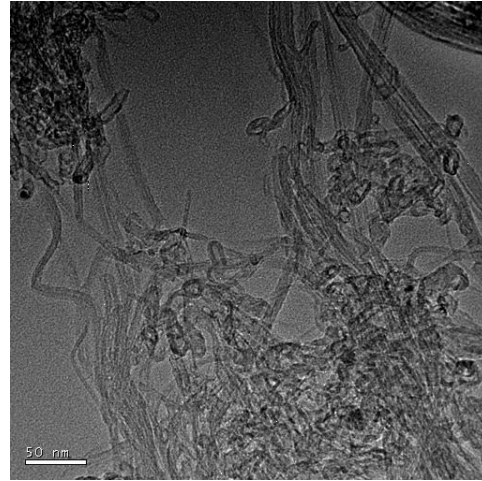
$$\lambda_D = \left(\frac{\epsilon_r \epsilon_0 k_B T}{q^2 N_0} \right)^{1/2} \quad (\text{A6.5})$$

Appendix 7

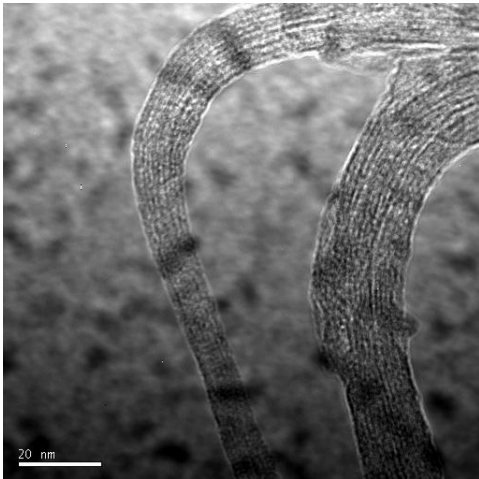
A7. The Images Obtained from the Morphology and Microstructural Studies Conducted on the Nanotube Sample



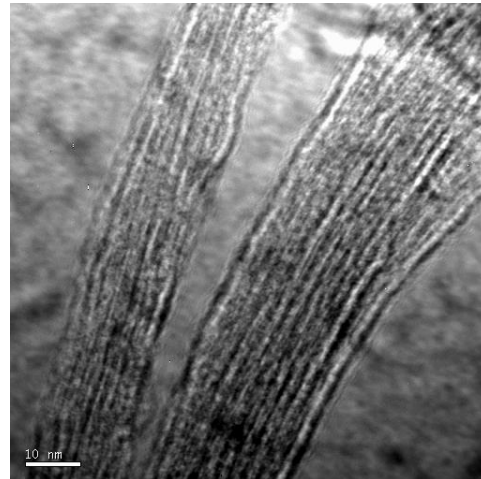
(a)



(b)



(c)



(d)

Figure A7.1: (a), (b) - Series of TEM micrographs showing the microstructure of the CNTs.

(c), (d) - Images (a) and (b) are magnified, black spots showing impurities.

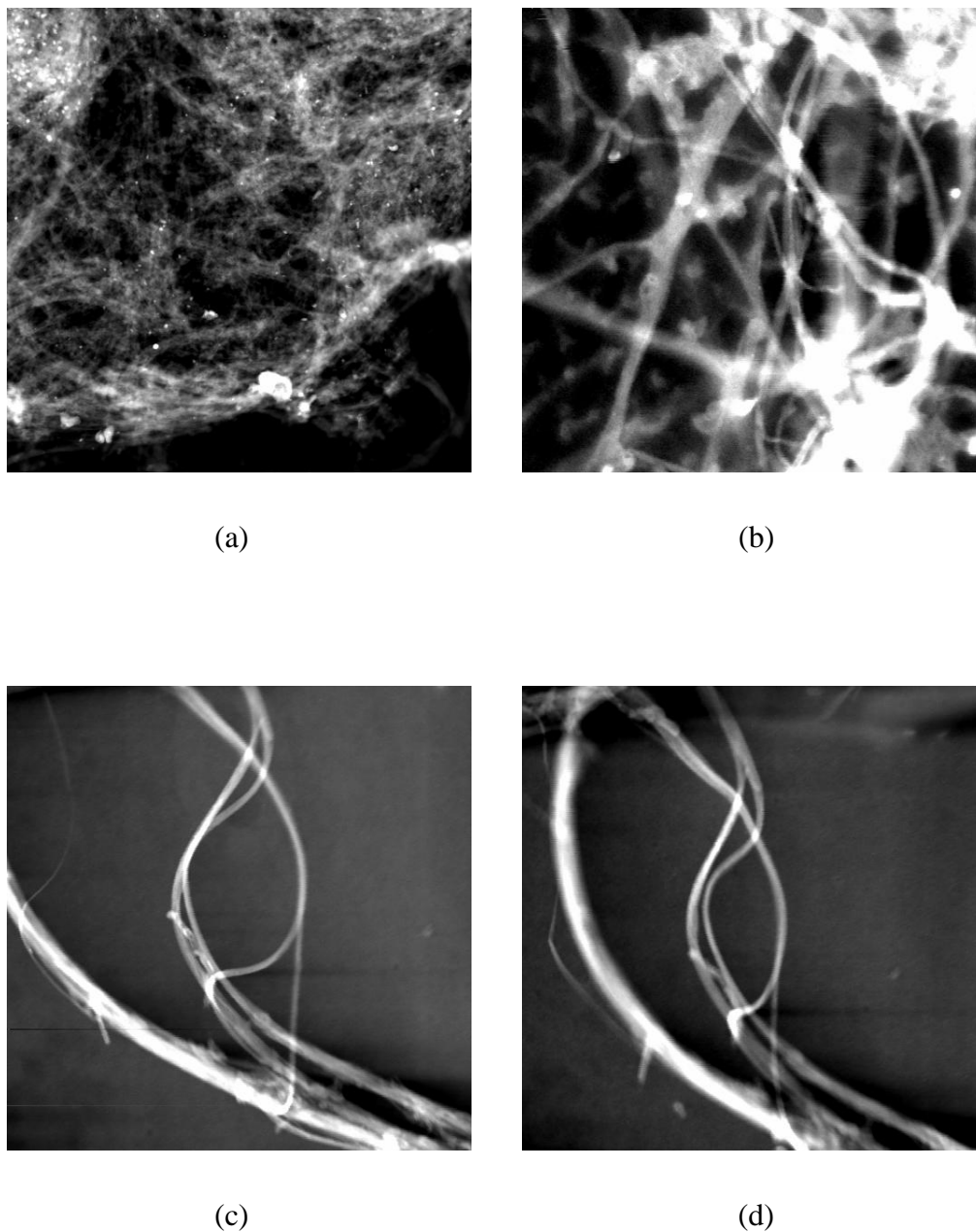
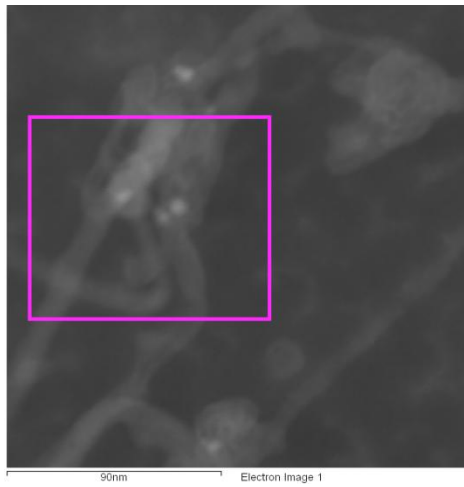
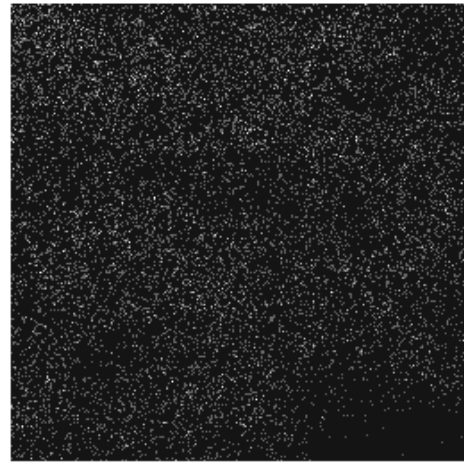


Figure A7.2: (a), (b) – Series of STEM photographs showing the bulk nanotube sample.
(c), (d) – Magnified to capture the presence of Fe particles (the bright dot)



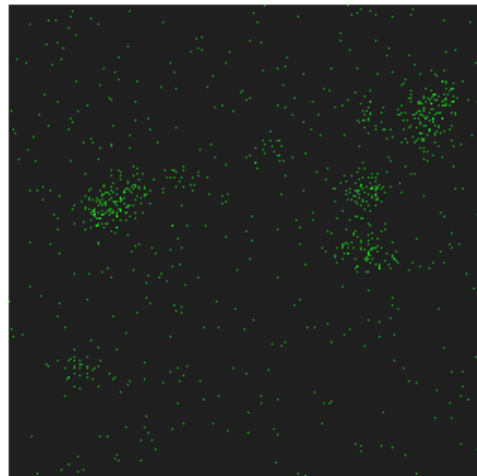
(a)



(b)



(c)



(d)

Figure A7.3: EDX analysis is performed on the inset shown in (a). (b) – Carbon, (c) – Silicon, and (d) – Iron

Appendix 8

A8. 3D Electromagnetic Simulation of Sapphire Dielectric Resonator for the Microwave Characterisation of Carbon Nanotubes Sample

A8.1 Introduction

Here the electrical conductivity of CNTs is examined by observing the change in the internal properties of a sapphire resonator when a nanotube powder is inside its cavity. The sapphire resonator is also modelled using COMSOL multiphysics. Our sapphire resonator model has a small disc of low-loss high dielectric constant (ϵ_1) that ensures most of the fields are contained within the dielectric, which results in a high Q-factor. The dielectric loss is due to a finite dielectric conductivity, or a finite phase angle between the dielectric polarisation and the electric field producing it. Therefore, the relative permittivity ϵ_r is complex and written as

$$\epsilon_r = \epsilon_1 - j\epsilon_2 = \epsilon_1(1 - j\tan\delta) \quad (\text{A8.1})$$

The real part (ϵ_1) of Eq. A8.1 measures the electrical energy stored in the dielectric while the imaginary part (ϵ_2) measures the loss in the medium as heat. This heat is due to damping of the vibrating dipole moments [1]. The radiation loss is very small and the quality factor of the dielectric (Q_d) is only limited by the losses inside the dielectric body. If the entire field of the resonant mode is stored inside the resonator and if there are no losses due to external fields, we have

$$Q_d = 1/\tan\delta \quad (\text{A8.2})$$

The quantity $\tan\delta$ is known as the loss tangent, which is defined as $\tan\delta = \epsilon_2/\epsilon_1$. The sapphire resonator was used to investigate the surface resistance of the nanotubes. For the TE_{011} resonant mode, a theoretical analysis of the electromagnetic fields allows the surface resistance and the current density to be determined from the value of the resonant frequency,

Q -value and dissipated power of the resonator. In dielectric resonators, the dielectric material in the resonator is used to concentrate the high frequency field on the measurement sample. The TE and TM modes with integer subscripts (m, n and p) are used to describe the resonant modes in dielectric resonators [1,2]. The subscripts m, n and p characterise half-period field variations in the circumferential, radial and axial directions, respectively. Most methods that measure surface resistance of samples use a TE_{01p} resonant mode. The TE_{01p} family of modes is unique because its electric field pattern is purely azimuthal. As shown in Fig. A8.1, the magnetic field in this mode is solenoidal in nature. Although there is no conducting material on the side of the walls of the dielectric rod, the mode still has a high Q -value. The resonant frequency of the isolated TE_{01p} mode in GHz is

$$f_0 = \frac{34}{a\sqrt{\epsilon_1}} \left[\frac{r}{l} + 3.45 \right] \quad (\text{A8.3})$$

where r and l represents the radius and length of the dielectric resonator, respectively.

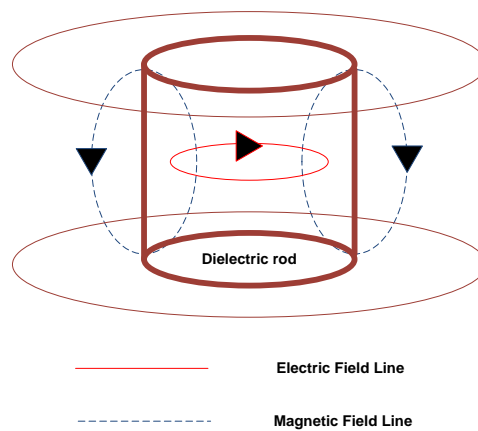
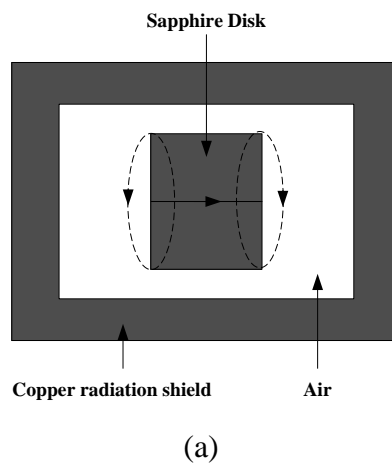


Figure A8.1: Field configuration for a TE_{011} resonant mode [3].

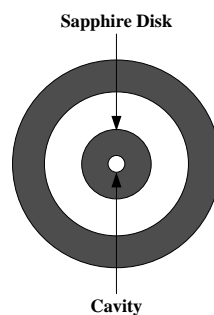
For this dielectric resonator method, a sapphire disk is attached permanently to a conducting plate. The Q -factor of the resonator is mainly dependent on the average value of the surface resistance of the conducting plate and the measurement sample.

A8.2 Sapphire Resonator Model

A cylindrical sapphire resonator-based measurement method is implemented for examining the electrical properties of CNTs. The main building block of this resonator is the single crystal sapphire, which has a cavity to allow the insertion of measurement samples. Sapphire is an anisotropic material and its dielectric constant is dependent on the direction of the electric field. In the model, the sapphire rod has a diameter of 4mm and a length of 7mm . To avoid radiation losses, we enclose the sapphire rod in a cylindrical copper shield. The internal diameter and the length of the copper shield are 16mm and 10mm , respectively. The model permits a hole of diameter 2mm in the sapphire cavity, and the sample is placed in this gap. Fig. A8.2 shows a schematic of the sapphire resonator used for this simulation. The resonant frequency of the resonator is around 3GHz .



(a)



(b)

Figure A8.2: A schematic of the cylindrical sapphire resonator. (a) Resonator with the field lines, dotted lines represent magnetic field patterns while the solid lines represent the electric field patterns (b) Top view of the structure.

The TE_{011} resonant mode of the sapphire dielectric resonator is used for our simulation. The sapphire resonator was placed in an electromagnetic field, which excites a TE_{011} resonant mode. Using COMSOL, the conducting sample inside a 2mm quartz tube is modelled. It is good to point out that the quartz tube is assumed to be filled with nanotubes sample. Therefore, an effective screening from the bulk nanotubes was observed. The loaded quartz tube is in the cylindrical cavity of the sapphire rod shown in Fig. A8.2. The permittivity of the sapphire rod is determined from the resonant frequency. The simulation is started by defining the conductivity of the sample. The sample is in the region of high magnetic field, which is in the middle of the sapphire rod. Screening current is induced in the sample if its conductivity is high enough. During the flow of this current, the skin effect arises and electrons tend to move along the surface of the sample. The estimation of the skin depth is crucial when predicting how thick the sample in the quartz tube needs to be in order to minimise field penetration. The computed skin depth is compared to that obtained theoretically using the known surface resistivity model. The nanotubes in the bulk sample have various orientations, and there are physical contacts between the nanotubes.

From the quality factor, Q of the resonator shown in Fig. A8.2, the loss of the resonant system can be measured. The overall Q of the resonator device reflects the properties of the sample occupying the resonator. For this particular sapphire resonator, the Q is defined as [2]

$$Q = \omega_0 \frac{\text{time-averaged stored energy}}{\text{time-averaged power dissipated}} = \omega_0 \frac{\langle U \rangle}{\langle P \rangle} \quad (\text{A8.4})$$

$$\langle P \rangle = \langle P_{cnt} \rangle + \langle P_D \rangle + \langle P_R \rangle \quad (\text{A8.5})$$

where $\langle P_{cnt} \rangle$ is the power loss in the sample, $\langle P_D \rangle$ is the dielectric power loss and $\langle P_R \rangle$ is the power loss due to fields radiation. The sapphire rod is placed in a closed cavity with high conductive walls. Therefore, the field radiation is assumed to be zero, leaving us with $\langle P_{cnt} \rangle$ and $\langle P_D \rangle$.

$$\frac{1}{Q} = \frac{\langle P_{cnt} \rangle}{\omega_0 \langle U \rangle} + \frac{\langle P_D \rangle}{\omega_0 \langle U \rangle} = \frac{1}{Q_{cnt}} + \frac{1}{Q_D} \quad (\text{A8.6})$$

where Q_{cnt} is the sample Q factor and Q_D is the Q factor of the sapphire rod. For Q_{cnt} calculations, we have

$$\langle P_{cnt} \rangle = \frac{1}{2} R_S \int_S H_S^2 dS \quad (\text{A8.7})$$

$$\langle U \rangle = \frac{1}{2} \int_V \mu_0 H^2 dV \quad (\text{A8.8})$$

where R_S is the surface resistance, S is the surface area of the cavity, V is the volume of the cavity, μ_0 is the permeability of free space and H is the magnetic field strength. Therefore, Q_{cnt} becomes

$$Q_{cnt} = \frac{\omega_0 \mu_0 \int_V H^2 dV}{R_S \int_S H_S^2 dS} \quad (\text{A8.9})$$

For Q_D calculations,

$$\langle P_D \rangle = \frac{1}{2} \omega_0 \varepsilon_0 \varepsilon_2 \int_{ins} E^2 dV \quad (\text{A8.10})$$

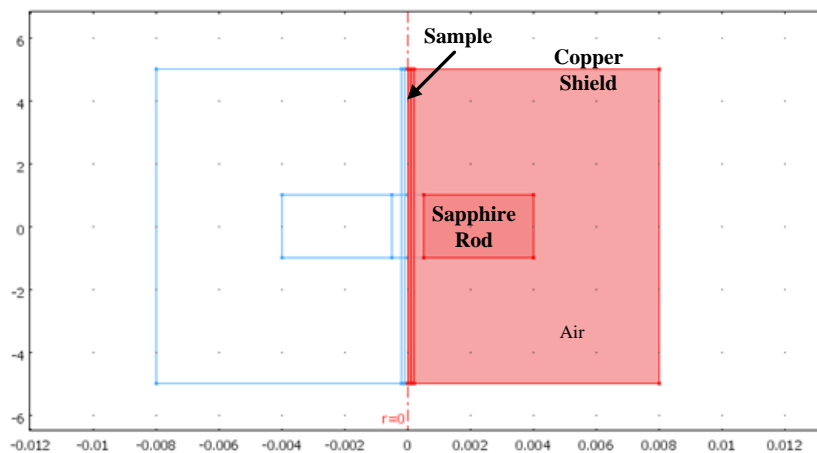
$$\langle U \rangle = \frac{1}{2} \int_{ins} \varepsilon_0 \varepsilon_1 E^2 dV + \frac{1}{2} \int_{out} \varepsilon_0 \varepsilon_2 E^2 dV \quad (\text{A8.11})$$

where ε_0 is the permittivity of free space, ε_1 is the permittivity in the air region, ε_2 is the permittivity of the dielectric, E is the electric field, *ins* represents the region inside the dielectric, *out* represents the air region between the copper shield and the dielectric, $\langle U \rangle$ is the total energy stored inside the dielectric and the air around it [2]. Therefore, Q_D becomes

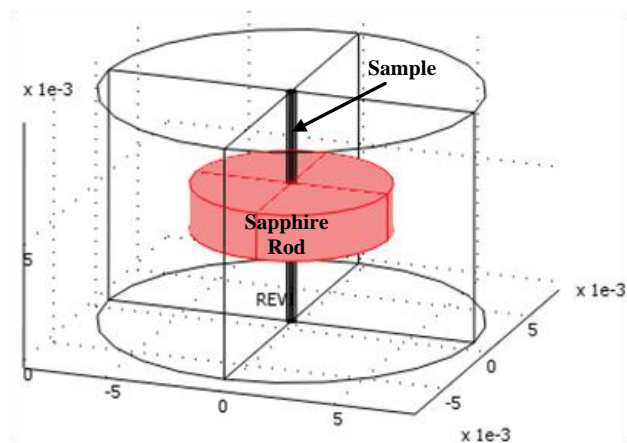
$$Q_D = \frac{\omega_0 \left(\frac{1}{2} \int_{ins} \varepsilon_0 \varepsilon_1 E^2 dV + \frac{1}{2} \int_{out} \varepsilon_0 \varepsilon_2 E^2 dV \right)}{\frac{1}{2} \omega_0 \varepsilon_0 \varepsilon_2 \int_{ins} E^2 dV} \quad (\text{A8.12})$$

A8.3 Simulation Results

The sapphire resonator was designed using the axisymmetric electromagnetics application mode in COMSOL. The simulation method presents the cylindrical structure of the resonator as a rectangular geometry due to the nature of this application mode. The modelling plane is a $r - z$ plane, where the r -axis represents the horizontal axis and the z -axis represents the vertical axis. The actual 3D geometry of the model can be obtained by revolving the 2D geometry around the z -axis. Fig. A8.3 shows the 2D and 3D geometries of the sapphire resonator modelled using COMSOL.



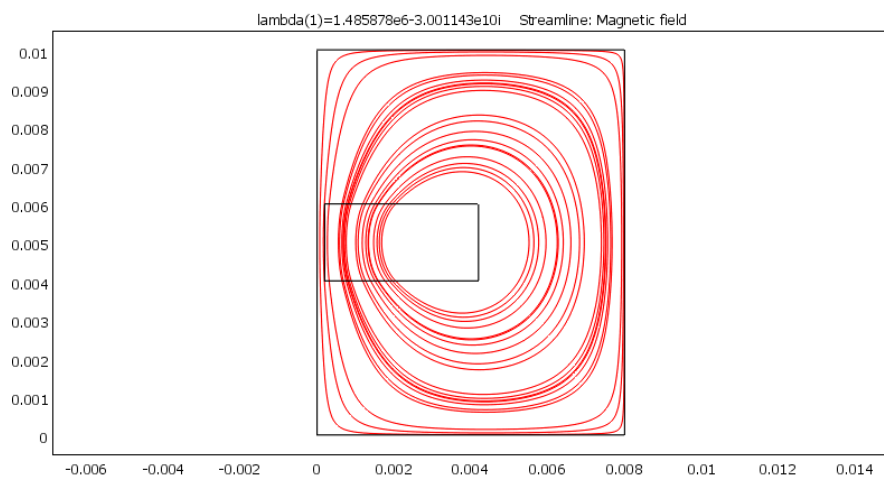
(a)



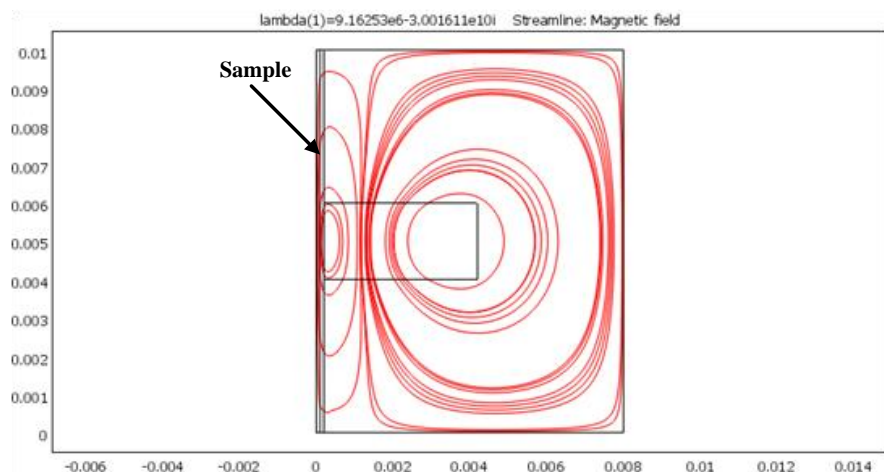
(b)

Figure A8.3: 2D & 3D geometries of the sapphire resonator modelled using COMSOL.

A TE_{011} resonant mode is excited due to the ratio of *length/diameter* (0.5) of the cylindrical resonator. Fig. A8.4 shows the field patterns in the resonator with and without the sample. Sapphire is a high dielectric material and when operating in the TE_{011} mode, most of the stored electric energy and magnetic energy are contained within the material. As shown in Fig. A8.4, the remainder of the energy is distributed around the dielectric resonator in the space within the shield. Current is driven through the conductive sample using the region concentrated with magnetic field.



(a)



(b)

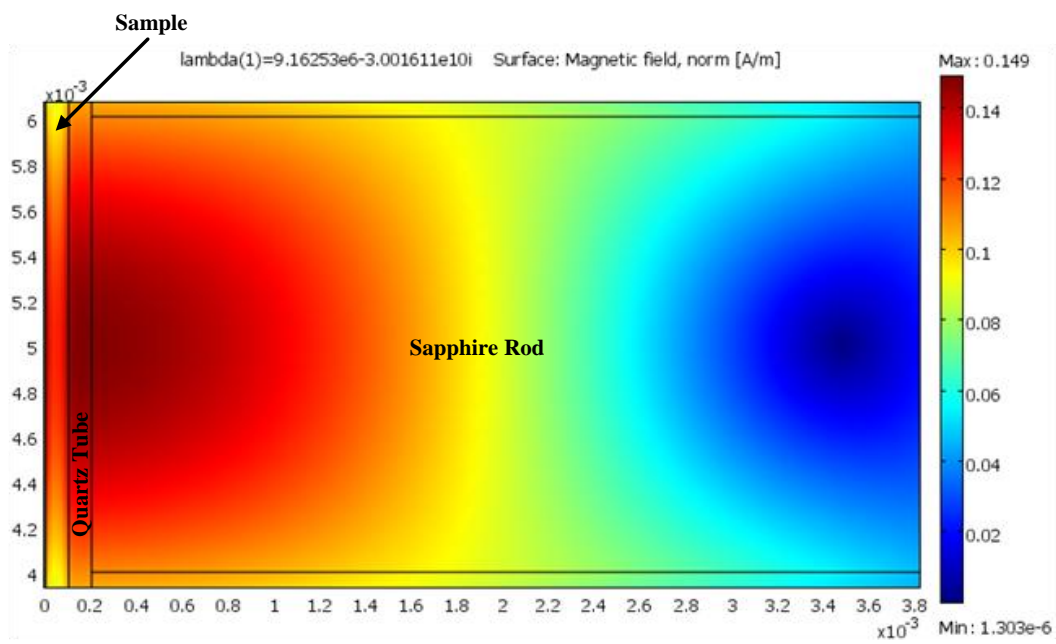
Figure A8.4: The TE_{011} magnetic field pattern in the sapphire resonator simulated using COMSOL (a) before inserting the conducting sample, (b) after inserting the sample.

For an assumed conductivity of 10^6 S/m, a skin depth of $7.3\mu\text{m}$ was computed for the conducting sample. The sample fills a quartz tube having a length of $100\mu\text{m}$ and a diameter of $10\mu\text{m}$. The current density at the surface of the sample is much higher than that within the interior of the sample due to the skin effect. The accuracy of the simulation model was investigated by comparing the computed skin depth to that theoretically calculated using the surface resistivity model. As analysed in Table A8.1, the skin depth varies with the conductivity of the sample. As the conductivity increases, the skin depth decreases and the electrons move along the surface of the sample, which validates the simulation method.

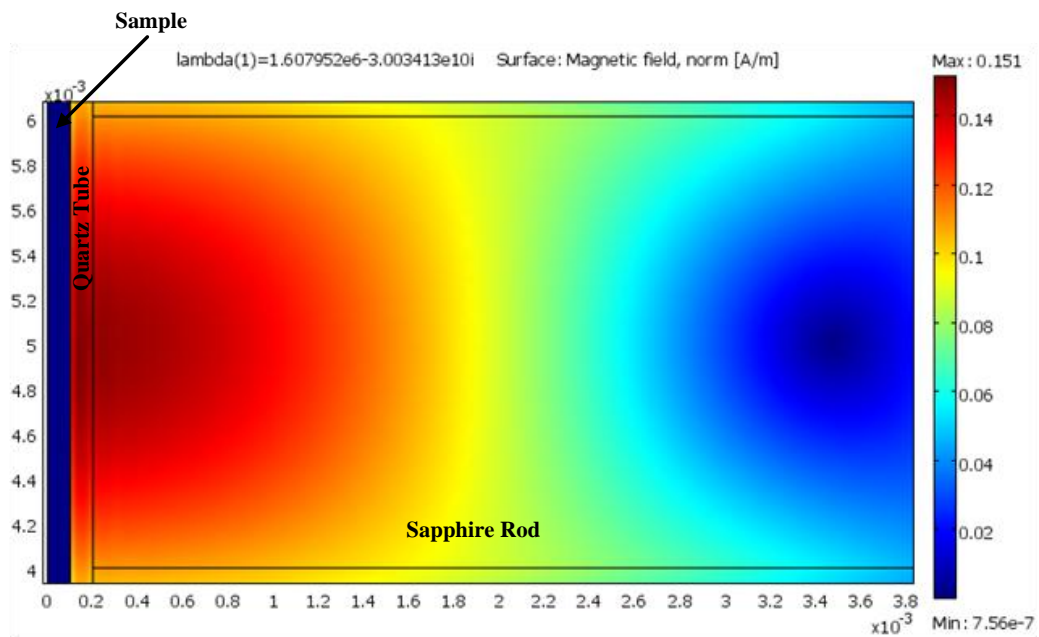
Conductivity [S/m]	Theoretical Calculation [m]	Measured Value [m]
10^6	7.2×10^{-6}	7.3×10^{-6}
10^4	7.3×10^{-5}	7.3×10^{-5}
10^3	2.3×10^{-4}	2.3×10^{-4}

Table A8.1: The skin depth computed from our simulation model is compared to that of the surface resistivity model.

Experimentally, a high field screening from the CNTs sample was observed. In the experiment, it was suggested that the extensive field screening is due to the high conductivity of the CNTs. Here the simulation is started by assuming a conductivity of 10^7 S/m for the sample placed in the sapphire resonator [4]. Using this conductivity, a field screening was observed when the conducting sample was placed in the region of high magnetic field. Fig. A8.5 shows the screening observed in our simulation. As shown in Fig. A8.5a, the entire magnetic fields penetrate into the sample with a conductivity of 10^4 S/m. When the conductivity of the sample is $> 10^6$ S/m, the penetration of the magnetic fields is limited.



(a)



(b)

Figure A8.5: Field screening observed when the conducting sample is placed in the region of high magnetic field. (a) Assumed conductivity of 10^4 S/m, and (b) conductivity of 10^7 S/m.

Also, the conductivity of the sample is varied and the magnetic field strength computed at the surface of the sample. As shown in Fig. A8.6, the field strength at the surface of the sample decreases as its conductivity in the simulation is increased. This observation suggests that the experimental nanotubes sample exhibited screening because it is very conductive.

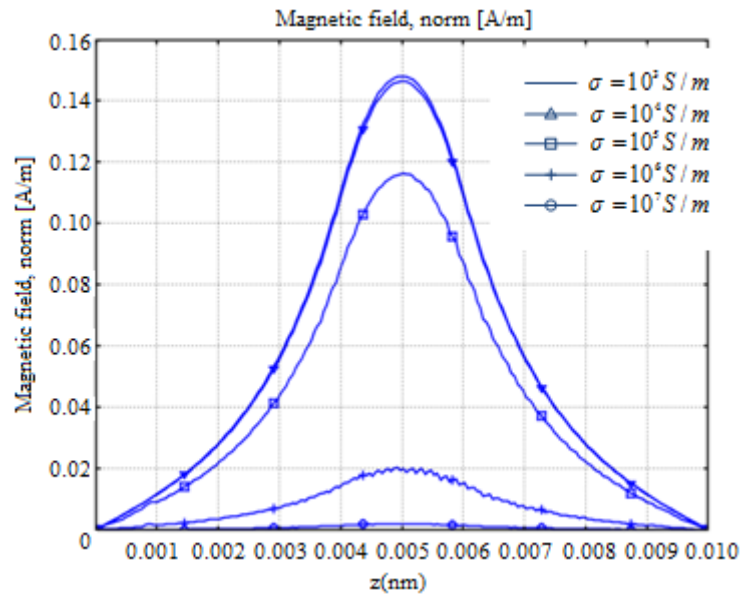


Figure A8.6: The plot of the magnetic field strength against position (z [m]) along the surface of the conducting sample with varying conductivity.

A8.4 References

- [1] D. M. Pozar, *Microwave Engineering, Third Edition*, John Wiley and Sons, N. Y., 2005.
- [2] D. Kajfez and P. Guillon, *Dielectric Resonators, Second Edition*, Noble Publishing Corporation, Atlanta, 1998.
- [3] S. J. Fiedziuszko and P. D. Heidmann, *Dielectric Resonator Used as a Probe for High T_C Superconductor Measurements*, *IEEE MTT-S Digest*, Pages 555-558, 1989.
- [4] J. Baker-Jarvis, M. D. Janezic, and J. H. Lehman, *Dielectric Resonator Method for Measuring the Electrical Conductivity of Carbon Nanotubes from Microwave to Millimeter Frequencies*, *Journal of Nanomaterials*, Volume 2007, Article ID 24242.

Appendix 9

A9. Publication - Modelling Charge Transport in Graphene Nanoribbons and Carbon Nanotubes using a Schrodinger–Poisson Solver

Appendix 10

A10. Publication - Microwave Characterisation of Carbon Nanotube Powders